This is to certify that the

dissertation entitled

Vibrational spectroscopy and structural properties of model compounds of photosynthetic reaction center and cytochrome oxidase

presented by

HONG ZHANG

has been accepted towards fulfillment
of the requirements for

Ph.D. degree in Chemistry

Wendell T. Bottrell
Major professor

Date July 28, 1995

VIBRATIO
MODEL CO
CYTOCHR

VIBRATIONAL SPECTROSCOPY AND STRUCTURAL PROPERTIES OF MODEL COMPOUNDS OF PHOTOSYNTHETIC REACTION CENTER AND CYTOCHROME OXIDASE

By

Hong Zhang

A DISSERTATION

Submitted to

Michigan State University
In partial fulfillment of the requirements
for the degree of

DOCTOR OF PHILOSOPHY

Department of Chemistry

1995

VIBRATION
COMPOUND
CYTOCHRO

The

solar energy

order to ass

separation p

photoinducte

base porphy

resolved, tw

state is dete

500 picosec

observed by

charge sepa

showed tha

state. The

characteristi

octaethylpo

In p

to investiga

series of int

(H)] and fe

performed

ABSTRACT

VIBRATIONAL SPECTROSCOPY AND STRUCTURAL PROPERTIES OF MODEL COMPOUNDS OF THE PHOTOSYNTHETIC REACTION CENTER AND THE CYTOCHROME C OXIDASE

By

Hong Zhang

The photosynthetic reaction center is a protein complex that converts captured solar energy into electrical and chemical energy in the first steps of photosynthesis. In order to assess the effects of structural and electronic properties on its initial charge separation process, different model compounds were synthesized. In this work, the photoinducted charge separated state of a covalently linked magnesium porphyrin and free base porphyrin heterodimer complex (Mg-H_2) is investigated by picosecond time-resolved, two-color, pump-probe resonance Raman spectroscopy. The charge separated state is detected within 30 picoseconds of laser excitation; recombination occurs within 500 picoseconds. The time scales of the charge transfer and recombination processes observed by Raman are consistent with those measured earlier by optical methods. In the charge separated state of the Mg-H_2 diporphyrin complex, vibrational mode correlations showed that the magnesium porphyrin cation half of the dimer is in its $^2A_{1u}$ electronic state. The free base porphyrin anion half of the charge transfer state has vibrational characteristic that are interpreted in terms of data available on the free base octaethylporphyrin anion.

In previous work of this lab, time-resolved vibrational spectroscopy has been used to investigate the reduction of dioxygen by mitochondrial enzyme, cytochrome oxidase. A series of intermediates were detected and assigned to oxy (Fe^{2+}-O_2), peroxy [Fe^{3+}-O^--O^-(H)] and ferryl (Fe^{4+} =O) species. In this work, 1). semi-empirical calculation has been performed on the peroxy species to evaluate the effect of electron transfer on the bond

cleavage

transitior

are com

suggest

oxidase

O-Cu)

Their s

Howe

distrit

a sim

cleavage and bond formation. The Fe^{3+}-O^{-}-O^{-}(H) bonding interaction and excited state transition energies are calculated. Their impacts on electronic structure and conformation are compared to experimental results. 2). the μ-oxo compounds have been widely suggested existing in different enzyme catalytic cycles which included the cytochrome c oxidase. A series of synthesized porphyrin based μ-oxo complexes (i.e., Fe-O-Fe and Fe-O-Cu) have been characterized by resonance Raman and other analytical techniques. Their structural implications on enzyme catalytic cycle are discussed.

A particle in a one-dimensional box is a classic quantum theory problem. However, it has been discussed mostly in the position space and its momentum distributions is misdescribed or incompleted in many textbooks. In this work, we present a simplified and explicit expression of a free particle in momentum space.

I would
financial suppor
Prof Cukier, Pr
people gave me
State, among t
the first laser
synthesized m
communicate
Gardner and
modeling, ar
many device
My s
their patient
was especi
Tang, and
choice of s

ACKNOWLEDGMENTS

I would like to thank Prof. G. T. Babcock for his guidance, especially his financial supports during last two years of this thesis work. I would also like to thank Prof. Cukier, Prof. Chang and Prof. Nocera to serve in my guidance committee. Many people gave me support, encouragement and friendships during my stayed at Michigan State, among them, Mary Tecklenburg and Tony Oertling taught me how to operate the first laser I used, a K^+laser, many years ago; W. Wu, Ying Liang and Nil Bag synthesized many fine model compounds used in this thesis work; Einhard Schmidt communicated spectroscopic data of μ-oxo compounds; Craig Essenmacher, Matt Gardner and Wenjun Shi discussed with me the computer programming and molecular modeling, and the machine shop and electronic shop of Chemistry Department made many devices which were essential to our experiments.

My special thanks go to my wife, Jingyang Lin and my daughter, Lillian for their patient and support during this long period of time. It has not been easy for me, it was especially hard for them. Finally, I would like to thank my mother, Xiuchun Tang, and my father, Min Zhang. Their expectation since I was a little boy made me choice of science as career and, I finally fulfilled my education.

TABLE OF CONTENTS

1.1 Observe
Resona
by Cyto
2.1 Focusin
2.2 Monoch
2.3 Quantu
2.4 Resona
Mg-Mg
2.5 Resona
Compo
Anion F
2.6 Ground
Neutral
2.7 a. Orbit
Comple
b. Net
2.8 a. Orbit
Comple
b. Net
4.1 Charge
angle e
4.2 Ground
4.3 Ground
4.4 Excited
Fe-O1 =
These T
Than th
4.5 Excited
Fe-O1 =
These T
Than the

LIST OF TABLES

4.6 Ground S
Complex
Imidazole

4.7 Ground S
Complex
Termina

4.8 Charge
hydrope
from th
bond le

4.9 Charge
angle e

4.10 Charg
compl
termir
equal

4.11 Char
has b
Fe-C
to 1

4.12 Cha
dio
ecl
Fe-

5.1 Th

LIST OF FIGURES

2.7 Resonance R
diporphyrin
laser line is

2.8 Two color p
spectra of M
(a). Probe b
(b). 30 psec
(c). 500 psec
The pump b
430 nm. So

2.9 Difference s
(a). Spectru
(b). Spectru
Subtraction

2.10 Two color p
of Mg-H_2 d
powers are
spectrum a
taken at 5 m
spectrum ta
for 55 minu

3.1a Top and sid
for the "pac
165.7° and

3.1b The X-ray c
diporphyrin

3.1c Top and sid
for the iron
and the Fe-C

3.1d The strucure
clusters. ...

3.2 The resonan
The excitat
The top spe
1 μm acetic

3.3 The resonar
The excitat
The top spe
with 1 μm a

3.4 The resonar
excitation is
top spectrun
1 μm acetic

3.5 The correla
μ-oxo bridg
angle are fr
vibrational f
here [3.8-3.

3.6 The correlat
μ-oxo bridg
Raman vibr
source as Fi

3.7 The resonar
The excitat
The top spe
with 1 μm a

3.8 The resonar
excitation is
top spectrur
1 μm acetic

4.1 a). the prop
oxidase, b)
for propose
Proc. Natl.

4.2 The peroxy
a). standard

b). hydr
termina
c). hydr

4.3 The cor
oxygen
angle eq

4.4 The 3-D
peroxy

4.5 Compu
Fe-O =

4.6 Compu
Fe-O =

4.7 Compu
Fe-O =

4.8 The co
oxyger
angle

4.9 The 3-
hydrop

4.10 The 3-
hydrop

4.11 The 3
hydro

4.12 The
energ

5.1 Mor
value

The aim of
properties o
oxygen red
chapter we
complex, t
consider th
resonance
The second
of the oxy
review the
feasibility

Chapter One

GENERAL INTRODUCTION

Summary

The aim of this thesis work is to characterize the vibrational, electronic and structural properties of model compounds of the photosynthetic reaction center protein and the oxygen reduction intermediates of cytochrome c oxidase. In the first part of this chapter we briefly review the structure and functions of the biological electron transfer complex, the photosynthetic reaction center, and its model compounds. We also consider the theory and technical background of resonance Raman and time-resolved resonance Raman spectroscopy and their application to biologically relevant systems. The second part of this chapter gives a brief introduction to current progress in studies of the oxygen reduction mechanism by the cytochrome oxidase enzyme. We also review the theoretical background of semi-empirical computational methods and the feasibility of applying these methods to large biological molecules.

1.1 The Photos

The con

is one of the fu

$$H_2O +$$

In this equa

Photosynthet

the absorpti

dioxide [1,

splitting of

reactions.

Photosyste

a product

of photosy

chromoph

Al

photosyst

bacteria

up from

polypep

molecul

Howev

is in fac

acids.

1.1 The Photosynthetic Reaction Center

The conversion of the energy of light into chemical energy and electrical energy is one of the fundamental processes of life. The basic equation is:

$$H_2O + CO_2 \xrightarrow{\text{light}} (CH_2O) + O_2$$

In this equation, (CH_2O) represents carbohydrate, primarily sucrose and starch. Photosynthetic organisms are able to oxidize organic and inorganic compounds upon the absorption of light. They use the extracted electron for the fixation of carbon dioxide [1, 2]. The most important product is oxygen that is produced from the splitting of water. In green plants photosynthesis is mediated by two kinds of light reactions. Photosystem I generates reducing power in the form of NADPH. Photosystem II transfers electrons from water to photosystem I and evolves oxygen as a product. The primary charge separation occurs in the photosynthetic reaction center of photosystem II [3, 4]. This reaction center is a complex consisting of peripheral chromophores and integral membrane proteins.

Although the detailed structure and location of the reaction center in photosystem II is unclear today, the structure of the reaction center from purple bacteria has been resolved by x-ray crystallography [5, 6]. The reaction center is built up from four polypeptides. One of them is a c-type cytochrome. The remaining three polypeptides are called L, M and H because they have light, medium and heavy molecular weights as deduced from their electrophoretic mobility on SDS-PAGE. However, later experiments [7, 8] on amino acid sequences showed that the H subunit is in fact the smallest with 258 amino acids, followed by the L subunit with 273 amino acids. The M subunit is the largest polypeptide with 323 amino acids. The L and M

Figure 1.1 The posthetic groups in the bacterial reaction center.

Bacterial Reaction Center

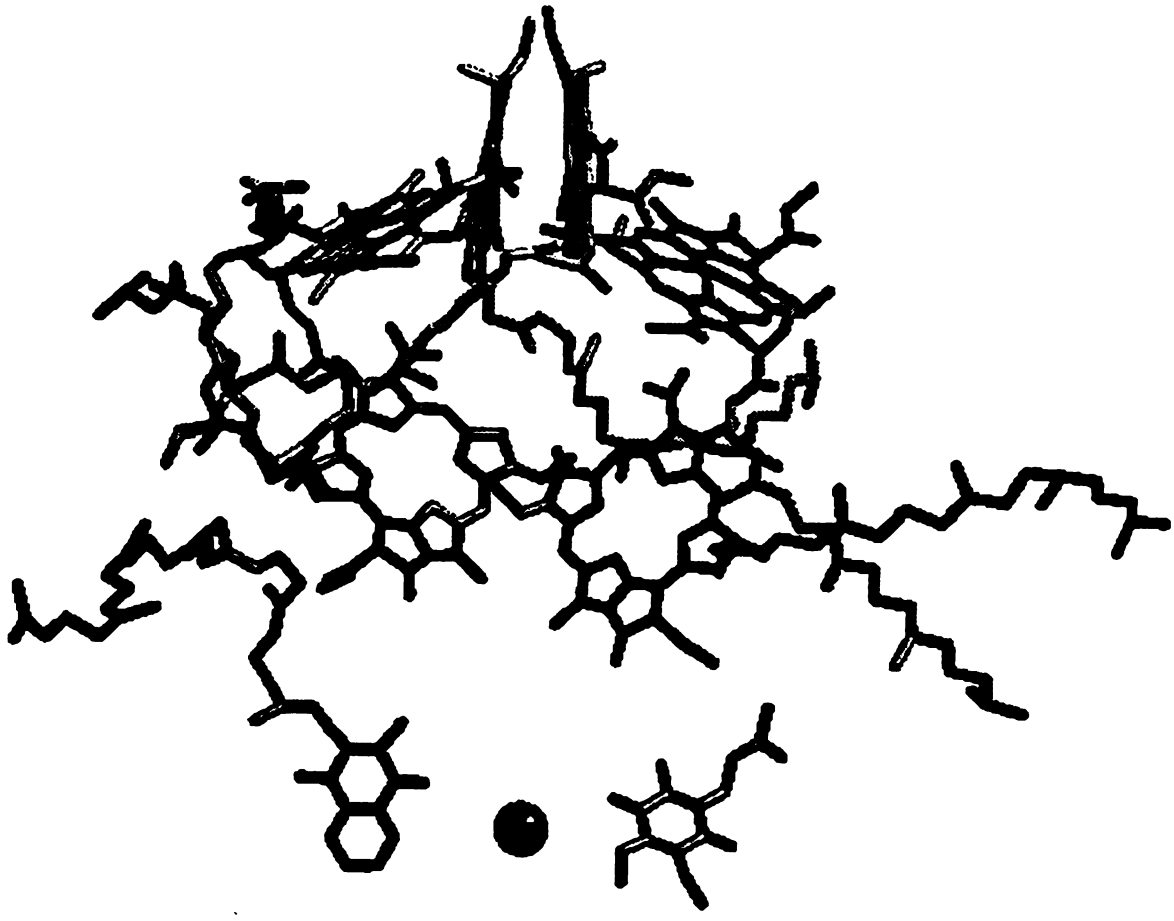

subunits show
evolutionarily
are further rel
the helices of

In add
molecules, tv
photosynthet
in the L and
the hydropho
other side of
"accessory"
contacts witl
$Pheo_M$, on t
two quinone

The
also called
electron tra
However,
special pa
bacterioch
[11]. Exp
pair (Fig.
$Pheo_L$ the
passes thr
process,
special p

subunits show sequence identity of about 25% and are therefore homologous and evolutionarily related proteins. In the crystal, the structurally similar L and M subunits are further related by a pseudo-twofold symmetry axis through the core, and between the helices of a four-helix bundle motif.

In addition to the polypeptide backbone, there are four bacteriochlorophyll molecules, two bacteriopheophytin molecules and two quinone molecules in the photosynthetic reaction center (Fig. 1.1). These prosthetic groups are evenly arranged in the L and M subunits. Two of the bacteriochlorophyll molecules form a dimer in the hydrophobic pocket close to the symmetry axis between L and M subunits. At the other side of the membrane a ferrous non-heme iron is located on this C_2 axis. Two "accessory" bacteriochlorophyll molecules, $Bchl_L$ and $Bchl_M$, make hydrophobic contacts with the dimer on one side and the bacteriopheophytin molecules, $Pheo_L$ and $Pheo_M$, on the other side. Subsequent to the bacteriopheophytins in the structure are two quinone molecules, Q_A and Q_B.

The initial electron separation occurs at the bacteriochlorophyll dimer, which is also called the special pair [4]. In principle, two pathways could be used for the electron transfer process, one is along the L side and another is along the M side. However, only the L side is used in nature [9, 10]. The parallel orientation of the special pair and the close association of the dimer bacteriochlorophyll, accessory bacteriochlorophyll and pheophytin ring systems facilitates the transfer of the electrons [11]. Experiments [10, 12-24] have shown that upon electron separation at the special pair (Fig. 1.2), within 3 picosecond, an electron is transferred to the $Pheo_L$. From the $Pheo_L$ the electron further migrates to Q_A in 200 picoseconds. The electron then passes through the L subunit, to the second quinone, Q_B. This is a comparatively slow process, taking about 100 microseconds. The forward electron transfer rate from special pair to Q_A is more than eight orders of the magnitude faster than that of the

Figure 1.2 Electron transfer sequence and lifetime of intermediates in the bacterial photosynthetic reaction center.

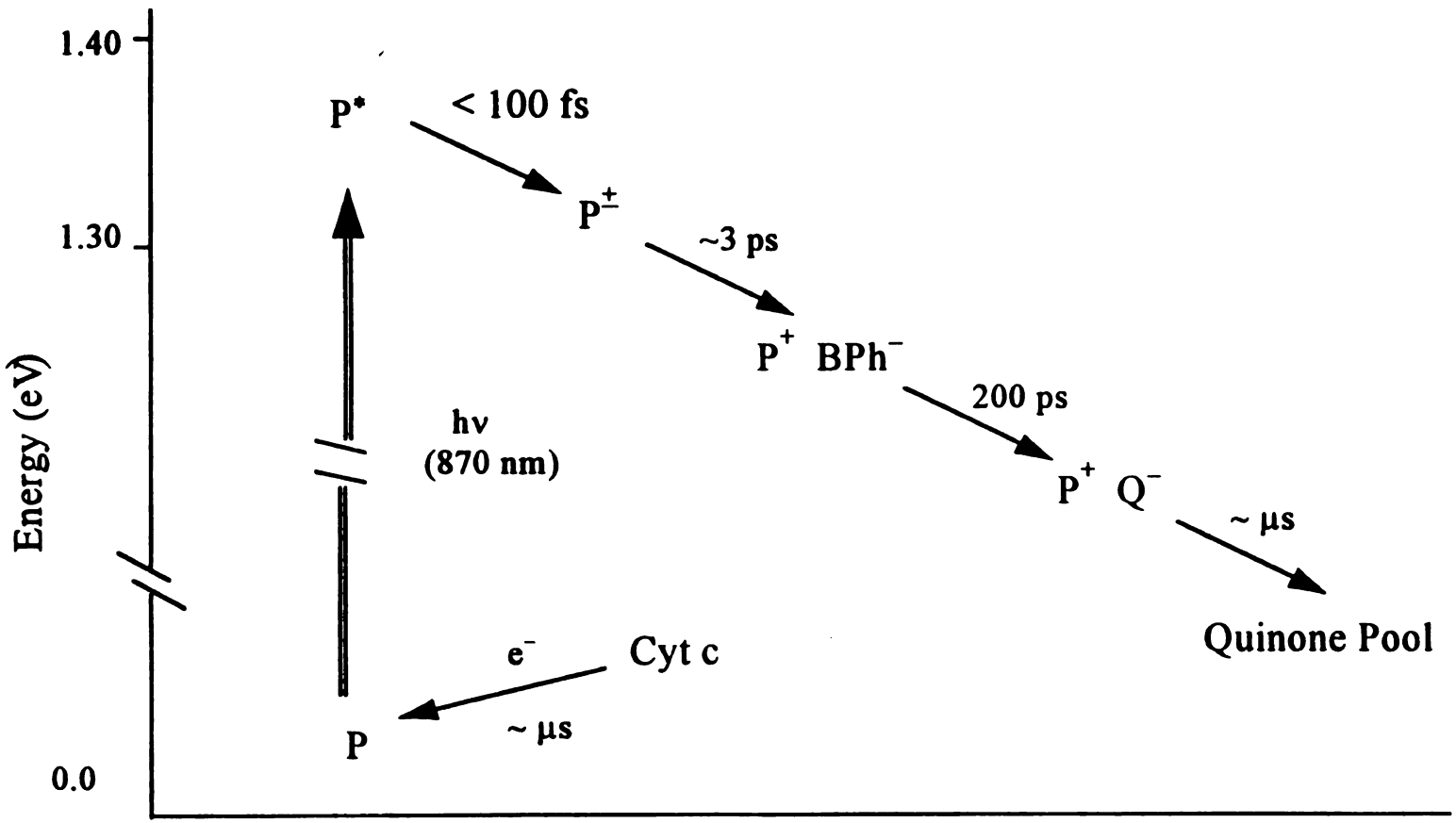
1.40
1.30
0.0
Energy (eV)
P*
< 100 fs
P±
~3 ps
P+ BPh−
200 ps
P+ Q−
~ µs
Quinone Pool
hν
(870 nm)
e−
Cyt c
~ µs
P

back reaction. Th

of the photon ene

This phen

systems of co

chlorophyll-porp

and carptenopo

the photophysi

Many spectros

50], transient a

77] have been

successful ex

electron trans

are the struc

Chang's grou

transient abs

separated ex

following π

state radiat

recombinat

relationshi

transfer rea

study of th

Bo

bacterial

coherent

the kineti

transfer p

back reaction. The large difference allows the reaction center to capture almost 100% of the photon energy it absorbs.

This phenomenon has stimulated efforts to model photosynthesis in artificial systems of covalently and noncovalently linked chlorophyll-chlorophyll [25], chlorophyll-porphyrin [26], porphyrin-porphyrin [27-33] porphyrin-quinone [34-40], and carptenoporphyrin [41,42] complexes. Extensive reviews of the general topics of the photophysics of the photosynthetic model compounds have been given [43]. Many spectroscopic techniques, such as EPR [44-48], X-ray crystallography [28, 49, 50], transient absorption [32, 33, 36, 51-58], emission [59] and, resonance Raman [68-77] have been employed to investigate these model systems. Among the especially successful experiments is the use of transient absorption spectra to monitor the electron transfer process in these model complexes. Of specific interest to this study are the structurally well defined Mg-H_2 diporphyrin complexes synthesized by Dr. Chang's group [27]. In particular, these compounds have been studied by picosecond transient absorption and emission spectroscopy [51-54]. An intramolecular charge separated excited singlet state of the Mg^+-H_2^- is formed within about 6 picosecond following π–π^* excitation. The charge separated state then decayed to the ground state radiationlessly or through the triplet manifolds. The correlation of charge recombination rates with polarizable solvents was also investigated. To understand the relationship of structure and conformation of porphyrin macrocycle to the charge transfer reactions, a resonance Raman and picosecond time-resolved resonance Raman study of the above diporphyrin complexes is presented in Chapter 2 of this thesis.

Both theoretical studies [60-62] and experimental evidence [23, 24] on bacterial photosynthetic reaction centers and mutants [63] have suggested that coherent nuclear motion or coherence in electronic coupling, or both, play a role in the kinetic evolution of the dimer excited state and in the following primary electron transfer process. Vibrational relaxation is a good measure of the transient structure

change and thus,
empirical analysi
cation, anion and
Chapter 2. The
to the charge sep

1.2 Resonance

Raman
destroyed, a s
initial state to
emission tak
events. The
take place
(spontaneo
meaningfu
apparent
band. T
resonant
concentr
polypep
vibratio
useful

articl
for a

change and thus, should give new insight into this process. Consequently, semi-empirical analysis of orbital occupancy and electronically structure of the neutral, cation, anion and the electronic excited neutral diporphyrin complexes is also given in Chapter 2. The implication of these results to the relationship of vibrational structure to the charge separated state is discussed.

1.2 Resonance Raman

Raman scattering is a concerted process during which an incident photon is destroyed, a scattering photon is created, and the system undergoes a transition from an initial state to a final state. This is not a process in which sequential absorption and emission take place because there are is no measurable time delay between the two events. The energy-time uncertainty principle $\Delta t \cdot \Delta E \sim \pi/4h$ thus allows the process to take place even if there is no energy level to match the energy of the incident photon (spontaneous Raman scattering), since the absorption does not populate a physically meaningful intermediate state. However, there are many special features that become apparent when an irradiation frequency is chosen close to a broad optical absorption band. The resonant signals are drastically enhanced in scattering from optically resonant chromophores, and thus good data can be obtained with sample concentrations as low as 10^{-6} M. Scattering from the non-resonant pigments of the polypeptides and other parts of proteins or organic compounds will not complicate the vibrational spectrum. These attributes make resonance Raman a very attractive and useful technique in biological applications.

The basic concepts of resonance Raman have been given by many review articles and textbooks [64-67]. The intensity of a Raman transition from state *m* to *n* for a system of randomly oriented molecules is given by

$$I_{m,n} = I_o$$

Where I_o is the i

$\alpha_{\rho\sigma}$ is the trans

scattered polariza

from second orde

$$(\alpha_{\rho\sigma})_{m,n}$$

$$+ \frac{< m \mid \mu_{\rho}}{(\nu_e -}$$

where μ_ρ and μ

Γ_e is a damping

an intermediate

energies ν_m a

exciting one qu

equation (1.2.2

scattering with

$(\nu_e - \nu_m)$ for so

in the sum bec

observed. Sin

the first term i

most case of re

$$I_{m,n} = I_o \frac{2^7 \pi^5}{3^2} \left(\frac{\nu_s}{c}\right)^4 \sum_{\rho\sigma} |(\alpha_{\rho\sigma})_{m,n}|^2 \qquad (1.2.1)$$

Where I_o is the incident light intensity, ν_s is the frequency of the scattered light, and $\alpha_{\rho\sigma}$ is the transition polarizability tensor, and ρ and σ specify the incident and scattered polarizations, respectively. The elements of the polarizability tensor derived from second order perturbation theory are given by

$$(\alpha_{\rho\sigma})_{m,n} = \frac{1}{h} \sum_e \left[\frac{< m | \mu_\rho | e >< e | \mu_\sigma | n >}{(\nu_e - \nu_m) - \nu_o + i\Gamma_e} + \frac{< m | \mu_\sigma | e >< e | \mu_\rho | n >}{(\nu_e - \nu_n) + \nu_o + i\Gamma_e} \right] \qquad (1.2.2)$$

where μ_ρ and μ_σ are the dipole moment operators, ν_o is the incident laser frequency, Γ_e is a damping factor for the e^{th} intermediate state, and $|e>$ is the wave function for an intermediate state with energy ν_e. The initial state (m) and the final state (n) have energies ν_m and ν_n, respectively. In the simplest case, n is produced from m by exciting one quantum of a particular vibration. When $\nu_o << \nu_e - \nu_m$ both terms in equation (1.2.2) are frequency independent and one observes non-resonant Raman scattering with the scattering intensity proportional to ν_s^4. When ν_o approaches $(\nu_e - \nu_m)$ for some optical transition that has a nonzero transition moment, the e^{th} term in the sum becomes dominant and resonance enhancement of the Raman scattering is observed. Since the energy denominator minimizes under these conditions only for the first term in equation (1.2.2), the (nonresonant) second term can be neglected in most case of resonance Raman scattering.

Figure 1.3 The schematic outline of two color, two pulse picosecond time-resolved resonance Raman experiments. The first laser pulse generates a population of an excited state. After a certain time delay, the second laser pulse probes the excited state at a different wavelength.

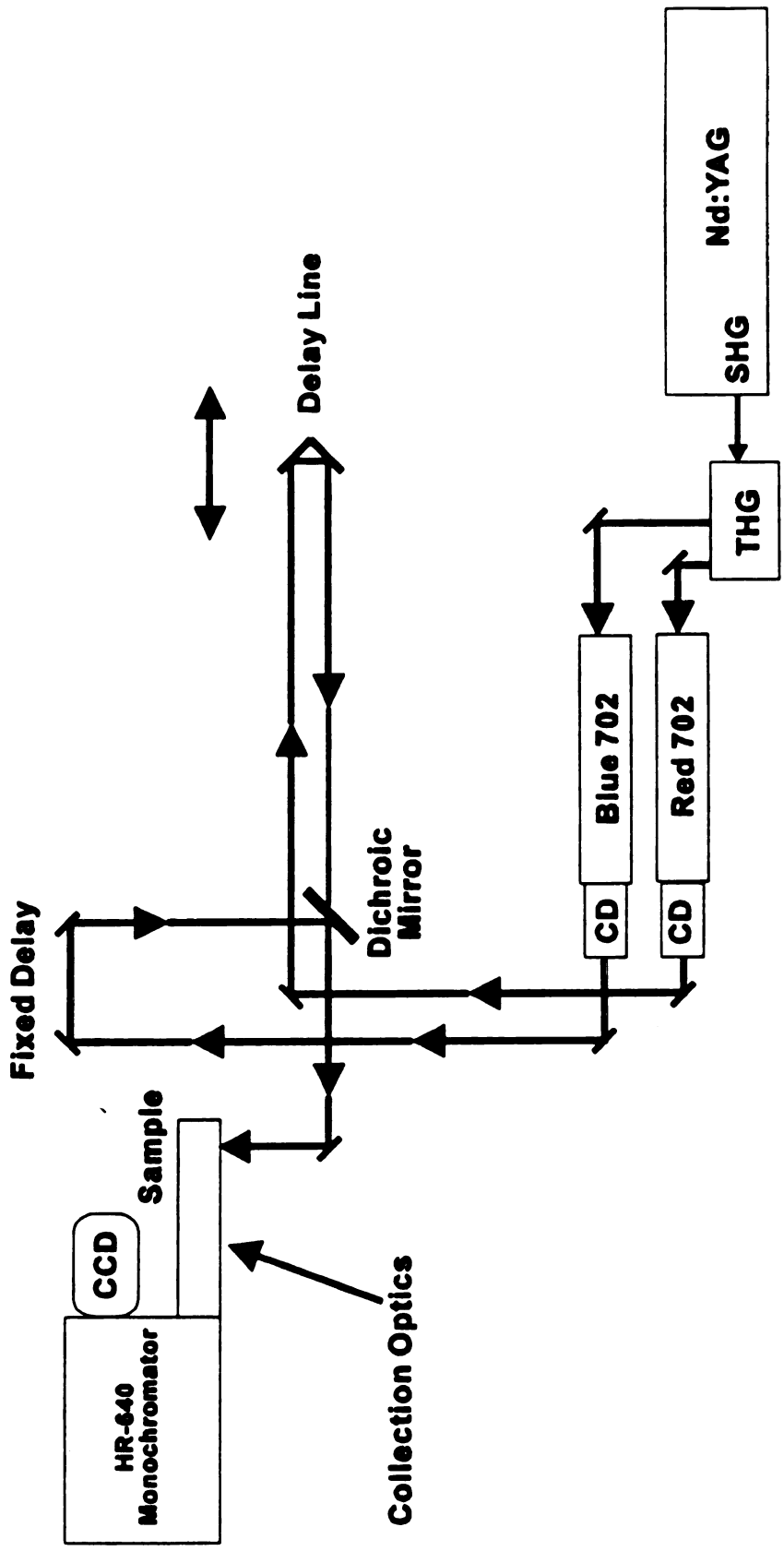
Nd:YAG
SHG
THG
Delay Line
Blue 702
Red 702
CD
CD
Dichroic Mirror
Fixed Delay
Sample
CCD
HR-640 Monochromator
Collection Optics

In addition

Raman spectrosco

[67]. First, reson

Raman signals fr

detecting the spec

broad absorbanc

solutions. Secon

carotenoid, have

effect. Their stro

are easily access

resonance Rama

because the de

multichannel, ch

monitoring inte

nanosecond and

in the next secti

1.3 Time-resolv

Time-res

spectra in a sh

As a scattering

Raman spectru

allowed by the

The one picose

cm^{-1}. Thus

characterizing

properties. Se

In addition to the above resonance effect, there are several other advantages of Raman spectroscopy relative to other vibrational techniques in biological applications [67]. First, resonance Raman spectra can be obtained from aqueous solutions since Raman signals from water are very weak so that they interfere only minimally in detecting the spectral features of the sample. In contrast, water has very strong and broad absorbances that hinder application of infrared spectroscopy to aqueous solutions. Secondly, many prosthetic groups in enzymes, such as heme, chlorin and carotenoid, have conjugated aromatic structures that are ideal for the resonance Raman effect. Their strong absorption in the visible-ultraviolet region (from 350 to 550 nm) are easily accessed by available laser lines. Another important advantage is that resonance Raman can be relatively easily applied to obtain time-resolved spectra because the detection technique of the Raman experiment can accommodate multichannel, charge-coupled device detection. This is a very useful feature in monitoring intermediates and reaction mechanisms. New approaches include nanosecond and picosecond time-resolved Raman techniques. This will be discussed in the next section.

1.3 Time-resolved resonance Raman

Time-resolved resonance Raman spectroscopy refers to the recording of Raman spectra in a short time after a laser pulse initiates a chemical process in the sample. As a scattering phenomenon, the Raman process has very short intrinsic lifetimes. The Raman spectrum of fast events can be recorded with time resolution as short as allowed by the laser excitation line broadening resulting from the uncertainty principle. The one picosecond time-scale can be reached, with a bandwidth of the order of 10 cm^{-1}. Thus the time-resolved resonance Raman has obvious applications for characterizing transient species, photobiological processes, and excited state properties. Several techniques have been implemented to investigate the biological

process. The f
light pulse init
early stage o
experiments t
systems, inclu
major disadva
pump and the
therefore, can

To ov
developed. T
laser flashes
isomerizatior
avoid the pr
probe pulse
probe spectr
basic outlin
experiment
population
certain tim
transient s
in order fo
used to in

Ar
balance c
preferred
detectior
detectio

process. The first is a one pulse pump-probe experiment in that the leading edge of the light pulse initiates the photoprocess and tailing edge of the pulse monitors it. In the early stage of the development of time-resolved Raman spectroscopy, a few experiments that employed this method were applied to several photochemical systems, including the visual pigment rhodopsin [68-70] and hemoglobin [71-74]. The major disadvantage of this approach is that there is no real time delay between the pump and the probe. The various photoprocesses that occurred in the excited state, therefore, can not be easily differentiated.

To overcome this limitation, two-color, pump-probe experiments have been developed. Two pulse, time-resolved resonance Raman with the wavelength of two laser flashes separated by less than 20 nm has been carried out to study photo-isomerization in carotenoid system [75-78]. Although this technique can effectively avoid the problem of one pulse pump-probe experiment by physically delaying the probe pulse relative to the pump pulse, the pump frequency will interfere with the probe spectrum as the monochromator can not, in general, totally separate them. The basic outline for a two color, two pulse time-resolved Raman technique adopted in our experiments is illustrated in Figure 1.3. First, a pump laser pulse generates a population of an excited state or a photoinitiated intermediate state. Then, after a certain time delay, a second laser pulse at a different wavelength is used to probe this transient species. The probe pulse is usually at least 30 nm apart from the pump pulse in order for the monochromator to distinguish them. Recently, this scheme has been used to investigate the photo-isomerization of stilbene derivatives [79, 80].

Another major concern in picosecond time-resolved Raman experiments is the balance of the laser pulse energy and average laser power. Large pulse energies are preferred in order to pump enough molecules to initiate a photoprocess for further detection. On the other hand, average laser power is crucial to the probe pulse for the detection of these photoinitiated intermediates. At present two types of experimental

set-ups are used
pump and detec
rate is in the Ml
of mW range),
advantages of t
repetition rate l
the dye laser pu
Hz and averag
for other exper
ideal method
quantum yield
accumulation
the sample ar
unwanted ever
(ASE) produc
signals difficu
above two typ
constructed ar

In a t
resonance Ra
excitation an
energy of th
equilibrium
prevent them
efficient Ram
provide the
with low-no

set-ups are used. The first is the direct use of the optimized dye laser outputs as the pump and detection sources for the experiments [75-78]. The typical pulse repetition rate is in the MHz range. High sampling rate, high average power (usually in the 10s of mW range), and stability for the detection of Raman scattering are the major advantages of this technique. The second approach uses the high peak power, low repetition rate laser pulses by using Nd:YAG laser or regenerator amplifier to pump the dye laser pulse. The typical pulse repetition rate after the amplification is 10 - 50 Hz and average power is about 10 mW [70-74, 80]. Although this set-up is suitable for other experiments such as transient emission and absorption, it is, however, not an ideal method for the Raman experiments. As Raman is a low-probability, low-quantum yield process and usually needs many sampling cycles, the long-time accumulation with the laser flashes of large peak power may cause photodamage of the sample and other nonlinear Raman processes [80]. In addition to that, other unwanted events, such as the usually large amount of amplified spontaneous emission (ASE) produced during the pulse amplified process, can make detection of the Raman signals difficult [73, 80]. After considering both advantages and disadvantages of above two types of set-up, the low peak power, high repetition rate apparatus has been constructed and used in our picosecond time-resolved experiments.

In a brief summary, the major requirements for the set-up of time-resolved resonance Raman spectroscopy are: a) a wide tunable range of radiation to enable the excitation and probing of the samples at their absorption peaks; b) sufficient peak energy of the laser pulse ($>$ 50 nJ and $<$ 50 μJ) to produce considerable non-equilibrium concentrations of transient species at a Raman detectable level and yet to prevent thermal damage to the samples; c) sufficient average power (~10mW) for efficient Raman signal detection; d) short duration of laser pulse (10^{-9}-10^{-12} sec.) to provide the temporal resolution required; e) high sensitivity of the detecting system with low-noise levels, which requires efficient collection optics for scattering photons,

a good quality m
other stray ligh
detection, such a

1.4 Porphyrin a

Porphyri
systems. These
They are all st
structures.
(bacterial)chlor
been particular
provide excelle
the porphyrin
pigments prov
responsible fo
example, resc
successfully u
hemoglobin an

As prop
Raman scatter
reaction cente
transfer, and c
few picosecon

a good quality monochromator to disperse the Raman signal and reject fluorescence or other stray light background, and a highly sensitive detector for Raman signal detection, such as the recently developed CCD camera.

1.4 Porphyrin and its derivatives

Porphyrin and its derivatives (Fig. 1.4) are common among many biological systems. These prosthetic groups usually play key roles in enzyme cooperativity [81]. They are all strong scattering centers as the result of their conjugated resonance structures. In recent years, resonance Raman studies on porphyrins, (bacterial)chlorins, and hemeproteins enzyme systems and their model complexes have been particularly interesting and productive [67, 81]. The above chromophores provide excellent Raman spectra that are rich in information about the conformation of the porphyrin conjugate macrocycle. Also, resonance Raman scattering from these pigments provides insight that is mechanistically important as they are usually responsible for the photochemistry and catalytical cycles of proteins [67]. For example, resonance Raman and time-resolved resonance Raman have been successfully used to monitor the oxygen binding mechanism [69-71, 74] of hemoglobin and the oxygen reduction process of cytochrome c oxidase [82-88].

As proposed, a long term project in the lab is to use time-resolved resonance Raman scattering to investigate the electron transfer reactions in the photosynthetic reaction center proteins. The time period for the initial charge separation, electron transfer, and charge recombination within the photosynthetic reaction center is from a few picoseconds to microseconds, well in the time range for Raman spectra to be

Figure 1.4 Porphyrin and its derivatives.

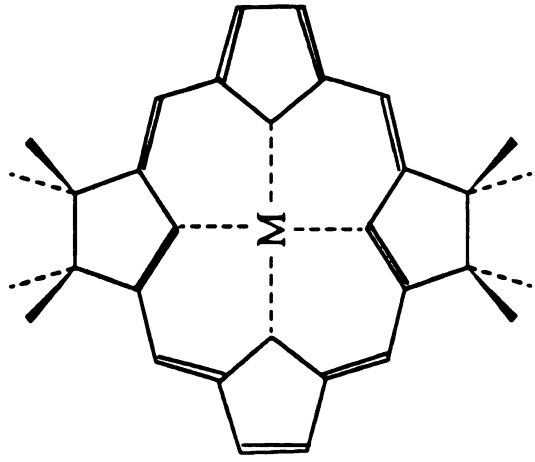

Bacteriochlorin

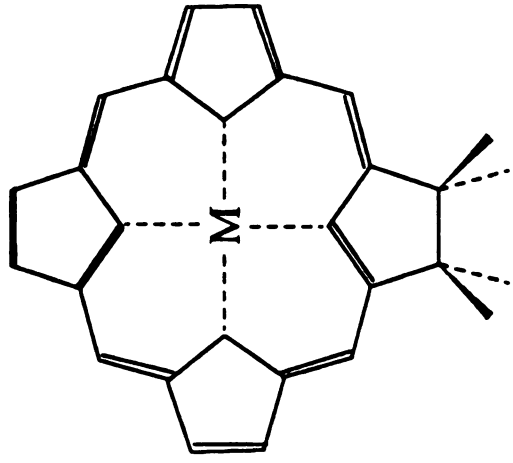

Chlorin

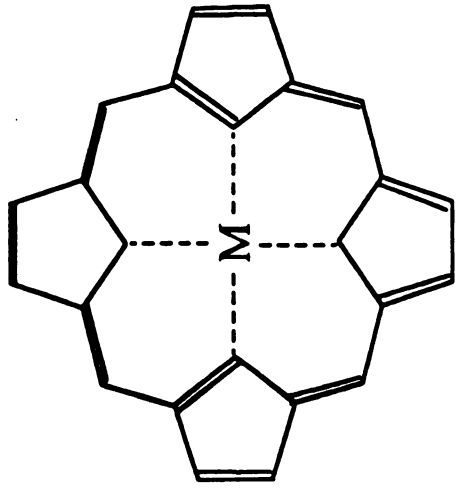

Porphyrin

recorded. An
relatively large
transfer steps,
reaction is, nor
90], it is assur
electron transf
suggested tha
vibrationally r
separation [91
of *Rhodobacte*
about two pi
coherences, w
adiabatic proc
scattering, as
surface, will

1.5 Cytochro

In mo
ATP (Adeno
(Nicotinamid
This process
membrane o
dioxygen oc
reductase, cy
these compl
pumping of

recorded. An intriguing feature of the photosynthetic reaction center complex is the relatively large distance between the pigments involved in the fast initial electron transfer steps, which are about 11 A^0 apart. The initial photosynthetic electron transfer reaction is, nonetheless, highly efficiency. In conventional electron transfer theory [89, 90], it is assumed that vibrational relaxation takes place on a time scale faster than electron transfer and that electron transfer reaction is essentially nonadiabatic. It was suggested that electron transfer from an excited state that is not completely vibrationally relaxed could be the origin of the high quantum yield of the charge separation [91]. Recently, femtosecond stimulated emission spectroscopy of a mutant of *Rhodobacter capsulatus* [23, 24] was able to detect oscillating components lasting about two picoseconds. These oscillations may be attributed to the vibrational coherences, which suggests that the primary charge separation may be a coherent and adiabatic process coupled to low-frequency vibrational modes. Excited state Raman scattering, as a technique for directly probing the anharmonicity of the potential energy surface, will be an ideal tool for the task to resolve this issue.

1.5 Cytochrome c Oxidase

In most aerobic organisms oxidative phosphorylation is the process in which ATP (Adenosine Triphosphate) is formed as electrons are transferred from NADH (Nicotinamide Adenine Dinucleotide) to dioxygen by a series of electron carriers [92]. This process is carried out by respiratory assemblies that are located in the inner membrane of mitochondria. The step-by-step electron transfer from NADH to dioxygen occurs through a chain of three large enzyme complexes, NADH-Q reductase, cytochrome c reductase, and cytochrome oxidase. Electrons flow within these complexes, which pierce the inner mitochondrial membrane, and lead to the pumping of protons across the membrane. Electrons are carried from NADH-Q

Figure 1.5 The cytochrome oxidase: a enzyme in the mitochondrial respiratory chain. It catalyzes the reaction in which O_2 is reduced to H_2O.

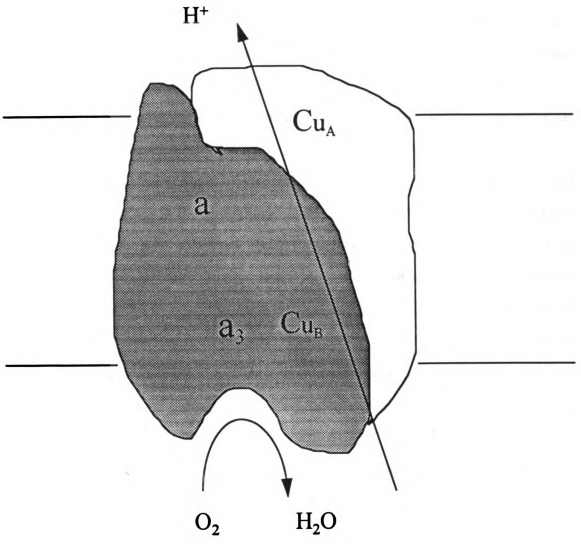
H+
Cu_A
a
a_3
Cu_B
O_2
H_2O

reductase to cyt

form of ubiquin

c reductase to cy

Cytochro

chain, catalyzes

this thermodyn

proton gradien

crystallographic

of high quali

dimensional cr

shape and its p

subunits, of w

genome [96].

a, Cu_A, cytoc

coordinate th

binuclear clu

The remainin

cytochrome c

Mole

electrons pro

Moreover, m

spin restricti

slowly and i

reduction of

organisms.

compound, is

has allowed a

reductase to cytochrome c reductase, the second complex of the chain, by the reduced form of ubiquinone. Cytochrome *c*, a small protein, shuttles electrons from cytochrome c reductase to cytochrome oxidase, the final component in the chain.

Cytochrome oxidase, the last of the mitochondrial enzymes in the respiratory chain, catalyzes the four-electron reduction of molecular oxygen to water and couples this thermodynamically favorable reaction to the formation of an electrochemical proton gradient across the membrane, i.e., proton pumping. The detailed x-ray crystallographic structure of this protein is unknown at present time, owing to the lack of high quality crystalline material. However, electron micrographs of two-dimensional crystalline arrays of cytochrome oxidase have been able to give its overall shape and its position in the membrane [93-95]. This complex contains at least eight subunits, of which three, subunits I, II and III, are encoded by the mitochondrion's own genome [96]. Among the subunits I and II, four metal centers (Fig. 1.5), cytochrome a, Cu_A, cytochrome a_3, and Cu_B, are bonded and mediate the redox chemistry and coordinate the translocation of protons. Cytochrome a_3 and Cu_B combine to form a binuclear cluster that is the site of dioxygen binding and reduction to H_2O [97, 98]. The remaining metal redox active sites function as electron mediators between cytochrome c and the binuclear center.

Molecular oxygen is an ideal terminal electron acceptor. Its high affinity for electrons provides a large thermodynamic driving force for oxidative phosphorylation. Moreover, molecular oxygen is in its triplet ground electronic state, which imposes spin restrictions on its reaction with singlet state reductants. Molecular oxygen reacts slowly and is kinetically stable unless activated by a catalyst. However, the partial reduction of molecular oxygen may generate highly hazardous intermediates in aerobic organisms. In particular, superoxide anion radical O_2^-, a highly destructive compound, is formed by transfer of a single electron to dioxygen. Evolution in Nature has allowed aerobic organisms to treat the reduction of dioxygen into water safely and

efficiently: the basic principle is that the enzyme must not release partially-reduced intermediates. Cytochrome oxidase meets this crucial criterion by binding dioxygen in its a_3-Cu_B center. The donation of two electrons, one from a_3 and another possibly from Cu_B, converts it into a dianion, or the peroxy form O_2^{2-}. Whether protons are involved at this stage is currently unknown. The input of another electron then leads to the formation of a ferryl intermediate in which iron is formally in the +4 oxidation state. Water is formed and released following acceptance of a second electron, and leaves OH^- bound to a_3. Two additional electrons serve to reduce the binuclear center back to its original oxidation state.

The mechanisms of dioxygen reduction by cytochrome oxidase has been extensively studied by a variety of spectroscopic methods [97]. The most commonly used technique is optical spectroscopy. The Gibson-Greenwood flow-flash technique, which is widely adopted in different kinetic studies, is based on this method [99, 100]: the laser flash photodissociates the CO from the fully reduced cytochrome oxidase. Dioxygen introduced in a mixing step before the photodissociation of CO will react with this enzyme and different reaction products can be monitored. One major application of this technique is to establish the kinetic scheme, i.e., reaction rates for possible intermediates. Recent experiments with a double flash techniques have suggested that O_2 first binds to the Cu_B site before it migrates to the a_3 site for further reactions [101]. Several other optical experiments also support this observation [102-104]. FTIR has also been used for this propose. Since this technique is usually sensitive to the high wavenumber vibrational modes, it has been used to monitor the initial CO binding to the Cu_B cluster, and it suggested that dioxygen may follow the same pathway [105-107]. This technique has also been used to study the structures of different ligand adducts in the a_3 - Cu_B binuclear center [108]. As resonance Raman is a vibrational spectroscopy that directly gives binding site information, especially due to its sensitivity in the low frequency region (200 cm^{-1} ~1000 cm^{-1}), it has recently been

applied to study the O_2 reaction mechanism [82-88, 109]. Resonance Raman experiments of different mutants of plant oxidase have been useful in clarification of the a_3 - Cu_B binding site information and possible interaction of this binuclear center with peptide backbones [109]. Time-solved resonance Raman has also been successfully applied to monitor the dioxygen reactions with fully reduced cytochrome oxidase. As showed in Table 1.1, vibrational modes belonging to the Fe^{2+}–O_2, Fe^{3+}=O and Fe^{3+}–OH^- species have been detected and confirmed by oxygen-18 isotope experiments. Based on these experimental results, a reaction scheme for the oxidation of fully reduced cytochrome oxidase by dioxygen has been proposed [97]. However, several major issues in this scheme remained to be answered, among them the structure of a proposed peroxy species, Fe^{3+}–O_2^{2-}, has not yet been confirmed in the transient Raman experiments despite the fact that simulations of concentration-time profiles (Figure 1.6) for these intermediates indicate that this species, if it exists, should build-up to a detectable level [85]. The assignment of this intermediate and its protonated form, Fe^{3+}–O_2^-(H) is also unclear [85, 87, 97]. Since these are transient intermediates, it is impossible to use other static techniques, such as x-ray crystallography to characterize their structural details. The proper model of the reaction mechanism needs both experimental evidence and theoretical support. It would be useful to clarify some of these issues by theoretical computational chemistry methods.

Several *ab-initio* and semiempirical methods have been used to study electronic structure of porphyrin and its derivatives [110], and O_2 binding to metalloporphines [111]. Among those methods, a semiempirical computational package, ZINDO, is our choice for the study of possible cytochrome oxidase

Figure 1.6 Simulations of concentration-time profiles for possible intermediates in the dioxygen reduction by cytochrome oxidase (reprinted from C. Varotsis, Y. Zhang, E. H. Appleman and G. T. Babcock *Proc. Natl. Acad. Sci. USA*, **1993**, *90*, 237).

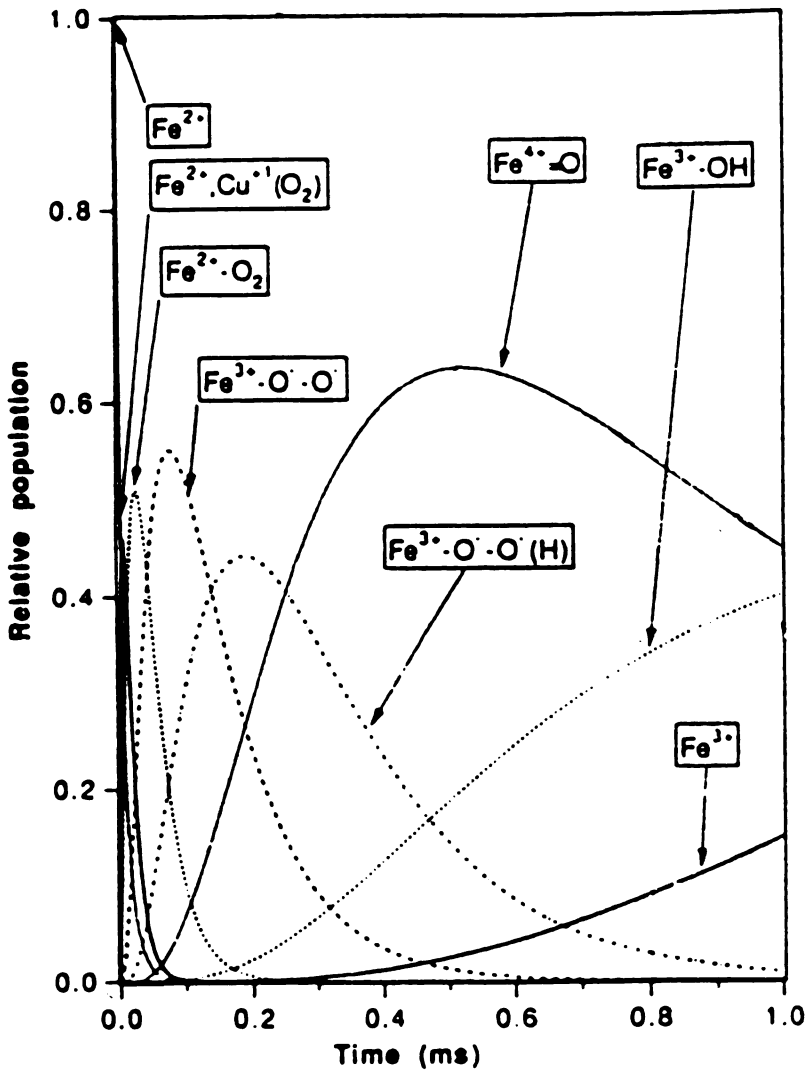
1.0
0.8
0.6
0.4
0.2
0.0
Relative population
0.0
0.2
0.4
0.6
0.8
1.0
Time (ms)
Fe2+
Fe2+.Cu+1(O2)
Fe2+-O2
Fe3+-O-O
Fe4+=O
Fe3+-OH
Fe3+-O-O(H)
Fe3+

Table 1.1
Resonance
Oxidase

Possible in
Babcock[a]
Kitagawa[b]
Rousseau[c]

a from [85

Table 1.1 Observed Frequencies (cm^{-1}) and Assignments from Time-resolved Resonance Raman Experiments of Oxygen Reduction Intermediates by Cytochrome Oxidase.

Possible intermediates	Fe^{2+}-O_2	Fe^{3+}-O^--O^-	Fe^{4+}=O	Fe^{2+}-OH^-
Babcock[a]	572	358	790	458
Kitagawa[b]	571	785	804	450
Rousseau[c]	568		786	450

a. from [85]; b. from [87]; c. from [88].

intermediate

and the cap

discuss som

implication

1.6 Gener

The

H

by using t

and relativ

energies c

summation

Ho

Schrodinge

finite linea

$\psi =$

in which th

principle to m

$E =<$

intermediates because of its ability to treat transition metal ions (heme iron) [112-116] and the capabilities of our computer facilities. In chapter four of this thesis we will discuss some of our computational results on peroxy and hydroperoxy species and their implication to the catalytic cycle of cytochrome oxidase.

1. 6 General Computational Methods

The Hamiltonian for an electron system in a molecular system can be written as

$$\hat{H} = \hat{H}_{core} + \sum_{i<j} r_{ij}^{-1} \tag{1.6.1}$$

by using the Born-Oppenheimer approximation and neglecting spin-orbital, spin-spin, and relativistic effects [117]. $\hat{H}_{core}$ stands for the sum of the kinetic and potential energies of all the electrons excluding those in the valence shell, and the double summation is the total energy of the Coulomb repulsion of all pairs of electrons *i* and *j*.

However, in most cases, it is impossible to solve the eigenvalues for the Schrodinger equation analytically. The usual approximation is to represent Ψ as a finite linear combination of antisymmetrical functions Φ_k of MOs φ_{ki}

$$\psi = \sum_{k}^{\kappa} A_k \Phi_k(\varphi_{k1}, \ldots, \varphi_{kn}) \tag{1.6.2}$$

in which the coefficients A_k are determined by the application of the variation principle to minimize the total energy expression

$$E = <\psi|\hat{H}|\psi><\psi|\psi> \tag{1.6.3}$$

The functi

Φ

of MOs c

describec

B

electrons

F

named th

this appro

averaged

constructi

combinatic

φ_i

In this LCAC

density or pop

the unpaired e

the AO, χ_v . I

configurations

Equation [1.6.2

The functions Φ_k are represented by the determinants

$$\Phi_k = \det|\varphi_{k1}, \ldots, \varphi_{kn}| \tag{1.6.4}$$

of MOs of electrons in different spatial and/or spin configurations. For this reason, the described method is termed configuration interaction (CI).

By introducing an effective one-electron "Fock" operator, $\hat{F}$, valid for all electrons, only a single representative eigenvalue problem

$$\hat{F}\,\varphi_i = \varepsilon_i \varphi_i \tag{1.6.5}$$

named the Hartree-Fock equation, has to be solved to obtain solutions for the MOs. In this approximation, each electron moves independently from the other electrons in an averaged Coulomb field arising from the other electrons and the nuclei. The construction of $\hat{F}$ for molecules is normally performed in the framework of a linear combination of N atomic orbitals (AOs), χ_ν, built to approximate the MOs:

$$\varphi_i = \sum_{\nu}^{N} c_{i\nu}\chi_\nu \tag{1.6.6}$$

In this LCAO-MO formalism, the square of the coefficients $c_{i\nu}$ represents the electron density or population in the AO, χ_ν, in the MO φ_i. In particular, if φ_i is occupied by the unpaired electron of a doublet radical, $|c_{i\nu}|^2$ represents the unpaired spin density in the AO, χ_ν. In a multidetermental CI treatment, the spin densities of all contributing configurations have to be summed up according to the weighting factor A_k of Equation [1.6.2] to give the total spin density.

The Fock operator of Equation [1.6.5] can be represented in the LCAO-MO formalism by a Fock matrix in the AO basis set χ_ν having the elements

$$F_{\mu\nu} = h_{\mu\nu} + \sum_{\lambda\sigma}^{N} p_{\lambda\sigma}[(\mu\nu|\lambda\sigma) - (\mu\lambda|\nu\sigma)/2] \qquad (1.6.7)$$

where

$$h_{\mu\nu} = \int_{core-integral} \chi_\mu(1)\, \hat{H}_{core}\, \chi_\nu\, d\tau_1 \qquad (1.6.8)$$

$$(\mu\nu|\lambda\sigma) = \iint_{two-electron\ Coulomb\ integral} \chi_\mu(1)\, \chi_\nu(1)\, r_{12}^{-1}\, \chi_\lambda\, \chi_\sigma\, d\tau_1\, d\tau_2 \qquad (1.6.9)$$

and electron density matrix

$$P_{\lambda\sigma} = \sum_{i}^{n} c_{i\lambda}^{*} \cdot c_{i\sigma} \qquad (1.6.10)$$

By applying the variation principle to the total Fock energy, we get a set of "Roothaan" equations

$$\sum_{\nu}^{N} (F_{\mu\nu} - \varepsilon_i S_{\mu\nu}) c_{i\nu} = 0 \qquad (1.6.11)$$

for the orbital energies and MO coefficients $c_{i\nu}$. The elements of the matrix $S_{\mu\nu}$ are the AO overlap integrals

$$\int \chi_\mu\, \chi_\nu\, d\tau \qquad (1.6.12)$$

Equation (1.6.11) is an eigenvalue problem that has to be solved iteratively, as $F_{\mu\nu}$ requires the MO coefficients $c_{i\nu}$ of the final solution. This follows from the appearance of the electron density matrix $P_{\mu\nu}$ in the effective electron repulsion field. The normal procedure is to start from some approximate solution for the $c_{i\nu}$ and, by inserting the improved solution into $F_{\mu\nu}$, to carry the iterations to a point that self-consistency is reached, i.e., when the changes in the $c_{\mu\nu}$ decrease beyond a given accuracy limit. These final " self-consistent field (SCF) solutions yield the desired "LCAO-MOs" φ_i and their orbital energies ε_i. A ground state electron configuration φ_1 ,..., φ_{kn} is then produced by consecutively filling these MOs with all electrons according to the Aufbau principle, in order of increasing values of ε_i.

1.7 INDO Method

The INDO semiempirical method is based on the " intermediate neglect of differential overlap" (INDO) approximation developed by Pople and Beveridge [117]. The INDO procedure is basically an extension of the zero-differential overlap (ZDO) approximation, which assumes a vanishing "differential overlap"

$$\chi_\mu \chi_\nu d\tau = 0 \tag{1.7.1}$$

between different AO basis functions in all of the space ($d\tau$ is an infinitesimal volume element). This has the consequence that only two-electron integrals of the form

$$(\mu\mu|\nu\nu) = \gamma_{\mu\nu} \tag{1.7.2}$$

or one pair AOs, have to be retained. This approximation greatly reduces the number of nonvanishing integrals to a stage where SCF calculations, even on large biological molecules, become feasible on computer.

form

The

exch

Thes

betw

as n

diffe

for

"Un

sens

S =

valu

offe

state

(RH

wor

it co

auto

reco

and

deve

By the INDO extension to include all valence orbitals, the full SCF-MO formalism becomes applicable to molecular systems without any symmetry restriction. The term " intermediate neglect" points to the retention of one center-two electron exchange integrals

$$\chi_{\mu\nu} = (\mu\,\nu\,|\,\mu\,\nu) \qquad (1.7.3)$$

These integrals make partial allowance for the different interactions taking place between two electrons with parallel or antiparallel spins. For open-shell systems, such as radical ions, the INDO methods conventionally employ "different orbitals for different spins" method [117]. This approach leads to two coupled Fock equations for α-spin (spin up) and β-spin (spin down). This method is known as the "Unrestricted Hartree-Fock" (UHF) MO treatment.

For large systems with more than 100 electrons, the UHF treatment has the serious disadvantage of admitting an increasing number of higher multiplet states (e.g. S =3/2, 5/2, ...) to the total wavefunction, ending up in unacceptably large expectation values of the total spin-angular momentum operator. A solution to this problem is offered by the "half-electron" method of Dewar et al [118] which produces ground state energies of open-shell systems in the frame-work of a restricted Hartree-Fock (RHF) treatment. It has the additional advantage that only one Fock matrix has to be worked with during the SCF procedure. The well-known failure of this method is that it completely ignores all spin polarization effects which, in a UHF treatment, follow automatically from the UHF approach. The spin polarization effects have to be recovered in a subsequent perturbation treatment. Different computational algorithms and parameterization procedures have been developed [114, 119, 120].

The ZINDO program used in our calculations is an INDO level approximation developed by Zerner and co-workers [112-116] which includes parameterization of

tra

par

the

IN

para

inte

[11

later

oper

trans

IND

from

and

where

γ^{μ}_{μ}

transition-metal complexes. This computational package contains two semi-empirical parameterization procedures: INDO/1 and INDO/s.

INDO/1 method is an INDO method for calculating geometry (so-called theoretical gamma) of the molecules. Its parameterization procedure is similar to other INDO methods but transition metals can be included.

INDO/s method refers to the INDO method with a spectroscopic parameterization (experimental gamma). and includes extensive configuration interaction (CI) for the calculation of excited state energies, i.e., the optical spectra [112-114]. The original program for CI procedures required a close-shell system. The later development of Rumer CI method has overcome this shortcoming, hence the open shell transition metal complexes, such as Cu complexes and the cation or anion transition metal compounds can be calculated [116]. Because of the requirement of INDO/s parameterization, the coulomb integrals are computed in algorithms different from INDO/1

$$\gamma_{\mu\mu}^{AB} = \frac{f_\gamma}{\frac{2 f_\gamma}{\gamma_{\mu\mu}^{A} + \gamma_{\mu\mu}^{B}} + R_{AB}} \tag{1.7.4}$$

and

$$\gamma_{\mu\mu,\nu\nu}^{AB} = \frac{f_\gamma}{\frac{2 f_\gamma}{\gamma_{\mu\mu}^{A} + \gamma_{\nu\nu}^{B}} + R_{AB}} \tag{1.7.5}$$

where f_γ is a constant that is semi-empirically parameterized by ZINDO mehtod and $\gamma_{\mu\mu}^{A}$ and $\gamma_{\nu\nu}^{A}$ are two-electron one center Coulomb integrals.

1.8 r

prob

pres

of th

and

1.8 momentum distribution of a particle in a one-dimensional box

A particle in a one-dimensional box has been a classic quantum theory problem. It, however, has been discussed mostly in position space and, is incorrectly presented in the momentum space in many textbooks. In Chapter five, as a final part of this thesis, we discuss a free particle in momentum space and obtained a simplified and explicit expression for its momentum distribution.

Ref

1.

2.

3.

4.

5.

6.

7.

8.

9.

10.

11.

12.

13.

14.

15.

16.

References

1. R. K. Clayton, *Photosynthesis: Physical Mechanisms and Chemical Patterns*, Cambridge University Press, **1980**.

2. J. K. Hoober, *Chloroplasts*, Plenum. **1984**.

3. A. N. Glazer and A. Melis, *Ann. Rev. Plant Physiol.* **1987**, *38*, 11.

4. W. W. Parson, in *Chlorophylls*, p 1153, H. Scheer *ed.*, CRC Press, **1991**.

5. J. P. Deisenhofer, O. Epp, K. Miki, R. Huber and H. Michel, *J. Mol. Biol.*, **1984**, *180*, 385.

6. J. P. Deisenhofer, O. Epp, K. Miki, R. Huber and H. Michel, *Nature*, **1985**, *318*, 618.

7. H. Michel, *et al* EMBO J. **1985**, *4*, 1667.

8. H. Michel, *et al* EMBO J. **1985**, *5*, 1149.

9. R. K. Clayton, T. Yamamoto, *Photochem. Photobiol.* **1978**, *24*, 67.

10. C. Kirmaier, D. Holten and W. W. Parson, *Biochom Biophys. Acta* **1985**, *810*, 33.

11. S. Franzen, R. F. Goldstein and S. G. Boxer, *J. Phys. Chem.* **1993**, *97*, 3040.

12. C. Kirmaier, D. Holten and W. W. Parson, *Biochom Biophys. Acta* **1983**, *725*, 190.

13. C. Kirmaier, D. Holten, R. Feick, and R. E. Balckenship, *FEBS Lett.* **1983**, *158*, 73.

14. C. Kirmaier and D. Holten, *Photosynth. Res.* **1987**, *13*, 225.

15. C. Kirmaier and D. Holten, *FEBS Lett.* **1988**, *239*, 211.

16. C. Kirmaier and D. Holten, *Proc. Natl. Acad. Sci. USA*, **1990**, *87*, 3552.

17. Woodbury, M. Becker D. Middendorf and W. W. Parson, *Biochemistry*, **1985**, *24*, 7516.

18. W. Zinth, J. Dobler and W. Kaiser, In *Ultrafast Phenomena V*, ed. G. R. Fleming and A. E. Siegman, Springer Ser. Chem. Phys. , Vol. 46, **1986**, 379.

19. W. Holzapfel, U. Finkele, W. Kaiser, D. Oesterhelt, H. Sheer, H. Stilz and W. Zinth, *Proc. Natl. Acad. Sci. USA*, **1990**, *87*, 5168.

20. G. R. Fleming, J.-L. Martin and J. Breton, *Nature*, **1988**, *333*, 190.

21. J. Breton, J.-L. Martin, A. Migus, A. Antonetti and A. Orszag, In *Ultrafast Phenomena V*, ed. G. R. Fleming and A. E. Siegman, Springer Ser. Chem. Phys., Vol. 46, **1986**, 393.

22. J. Breton, J.-L. Martin, J.-C. Lanbry, S. J. Robles and D. C. Youvan, In *Reaction Centers of Photosynthetic Bacteria*, ed. M.-E. Michel-Beyerle Springer, **1990**, 293.

23. M. H. Vos, J.-C. Lanbry, S. J. Robles, D. C. Youvan, J. Breton and J.-L. Martin, *Proc. Natl. Acad. Sci. USA*, **1991**, *88*, 8885.

24. M. H. Vos, F. Rappaport, J.-C. Lanbry, J. Breton and J.-L. Martin, *Nature*, **1993**, *363*, 320.

25. S. G. Boxer and R. R. Bucks, *J. Am Chem. Soc.* **1979**, *101*, 1883.

26. M. R. Wasielewski, D. G. Johnson, M. P. Niemczyk, G. L. Gaines, M. P. O'neil W. A. Svec, *J. Am Chem. Soc.* **1990**, *112*, 6482.

27. C. K. Chang, *J. Hetercycl. Chem.* **1977**, *14*, 1285.

28. J. P. Fillers, K. G. Ravichandran, I. Abdalmuhdi, A. Tulinsky and C. K. Chang, *J. Am. Chem. Soc.* **1986**, *108*, 417.

29. A. Heiler, G. L. McLendon and P. Rogaskyj, *J. AM. Chem. Soc.* **1987**, *109*, 604.

30. A. Osuka and K. Maruyama, *J. Am. Chem. Soc.* **1988**,*110*, 4454.

31. A. Osuka and K. Maruyama, *Chem. Lett.* **1987**, 825.

32. N. Mataga, H. Yao, T. Okada, Y. Kanda and A. Harriman, *Chem. Phys.* **1989**, *131*, 473.

33. A. M. Brun, A. Harriman, V. Heitz and J.-P. Sauvage, *J. Am. Chem. Soc.* **1991**, *113*, 8657.

34. J. A. Cowan, J. K. Sanders, G. S. Beddard, R. J. Harrison, *J. Chem. Soc., Chem. Comm.* **1987**, 55.

35. A. Osuka, S. Morikawa, K. Maruyama, S. Hirayama and T. Minami, *J. Chem. Soc., Chem. Comm.* **1987**, 359.

36. R. J. Harrison, B. Pearce, G. S. Beddard, J. A. Cowan, J. K. Sanders, *Chem. Phys.* **1987**, *116*, 429.

37. J. Dalton and L. R. Milgrom, *J. Chem. Soc., Chem. Comm.* **1979**, 609.

38. J. L. Sessler, M. R. Johnson and T. Y. Lin, *Tetrahedron* **1989** *45*, 4767.

39. J. L. Sessler, M. R. Johnson S. E. Creager, J. C. Fettinger and J. A. Ibers, *J. Am. Chem. Soc.* **1990**, *112*, 9310.

40. A. Osuka, S. Nakajima, K. Maruyama, N. Mataga, and T. Asahi, *Chem. Lett.* **1991**, 1003.

41. A. Osuka, H. Yamada and K. Maruyama, *Chem. Lett.* **1990**, 1905.

42. D. Gust *et al, J. Am. Chem. Soc.* **1993**, *115*, 5684.

43. M. R. Wasielewski, *Chem. Rev.* **1992**, *92*, 435.

44. H. Levanon, A. Regev, T. Galili, M. Hugerat, C. K. Chang and J. Fajer, *J. Phys. Chem.* **1993**, *97*, 13198.

45. K. Hasharoni, H. Levanon, J. tang, M. K. Bowman, J. R. Horris, D. Gost, T. A. Moore, A. L. Moore, *J. Am. Chem. Soc.***1990**, *112*, 55.

46. G. L. Gaines, M. P. O'Neil, W. A. Svec, M. P. Niemczyk M. R. Wasielewski, *J. Am. Chem. Soc.***1991**, *113*, 719.

47. A. Angerhofer, M. R. Wasielewski, G. L. Gaines, M. P. O'Neil, W. A. Svec, M. P. Niemczyk, *Z. Phys. Chem.* **1991**, *172*, 17.

48. F. Lendzian, B. von Maltzan *Chem. Phys. Lett.* **1991,** *180,* 191.

49. W. R. Scheidt, B. Cheng, K. J. Haller, A. Mislankar, A. D. Rae, K. V. Reddy, H. Song, R. D. Orosz, C. A. Reed, F. Cukiernik and J.-C. Marchon, *J. Am. Chem. Soc.* **1993,** *115,* 1181.

50. H. Song, C. A. Reed, and W. R. Scheidt, *J. Am. Chem. Soc* **1989,** *111,* 6867.

51. I. Fujita, J. Fajer, C. K. Chang, C. B. Wang, M. A. Bergkamp and T. L. Netzel, *J. Phys. Chem.* **1982,** *86,* 3754.

52. T. L. Netzel, M. A. Bergkamp and C. K. Chang, *J. Am. Chem. Soc.* **1982,** *104,* 1952.

53. J. M. Zaleski, C. K. Chang, G. E. Leroi, R. I. Cukier and D. G. Nocera, *J. Am. Chem. Soc.* **1992,** *114,* 3564.

54. J. M. Zaleski, C. K. Chang, G. E. Leroi, R. I. Cukier and D. G. Nocera, *Chem. Phys.* **1993,** *176,* 483.

55. O. Bilsel, J. Rodriguez and D. Holten, *J. Phys. Chem.* **1990,** *94,* 3508.

56. J. Rodriguez, C. Kirmaier, M. R. Johnson, R. A. Friesner, D. Holten and J. L. Sessler, *J. Am. Chem. Soc.* **1991,** *113,* 1652.

57. D. G. Johnson, M. P. Niemczyk, D. W. Minsek, G. P. Wiederrecht, W. A. Svec, G. L. Gaines, III and M. R. Wasielewski, *J. Am. Chem. Soc.* **1993,** *115,* 5701.

58. M. R. Wasielewski, G. L. Gaines, III, G. P. Wiederrecht, W. A. Svec and M. P. Niemczyk, *J. Am. Chem. Soc.* **1993,** *115,* 10442.

59. O. Bilsel, J. Rodriguez, D. Holten, G. S. Girolami, S. N. Milam and K. S. Suslick, *J. Am. Chem. Soc.* **1990,** *112,* 4075.

60. R. A. Marcus and R. Almeida, *J. Phys. Chem.* **1990,** *94,* 2973.

61. R. Almeida and R. A. Marcus, *J. Phys. Chem.* **1990,** *94,* 2978.

62. J. Jean, R. A. Friesner, G. R. Fleming, *Ber. Bunsenges. Phys. Chem.* **95,** 253.

63. S. J. Roble, J. Breton, and D. C. Youvan, In *Reaction Centers of Photosynthetic Bacteria,* M.-E. Michel-Beyerle eds. Springer, **1990,** 283.

64. J. Tang and A. C. Albercht, in *Raman Spectroscopy* Vol. II, ed. H. A. Szymanski, Plenum Press, **1970**, p. 33.

65. D. A. Long, *Raman Spectroscopy* McGraw-Hill, 1977.

66. A. T. Tu, *Raman Spectroscopy in Biology: Priciple and Applications* Wiley, **1982.**

67. *Biological Applications of Raman Spectroscop,* ed. T. G. Spiro, Wiley, **1988**.

68. J. Turner, J. D. Strong, T. G. Spiro, M. Nagumo, M. F. Nicol and M. A. El-Sayed, *Proc. Natl. Acad. Sci. USA,* **1981**, *78,* 1313.

69. E. M. M. van den Berg, D.-J. Jang, H. Bitting and M. A. El-Sayed, *Biophys. J.* **1990**, *58,* 135.

70. M. A. El-Sayed, *Acc. Chem. Res.* **1992**, *25,* 279.

71. E. W. Findson, J. M. Friedman, M. R. Ondrias and S. R. Simon, *Science* **1985**, *229,* 661.

72. R. G. Alden, L. D. Sparks, M. R. Ondrias, B. A. Crawford and J. A. Shelnutt, *J. Phys. Chem.*, **1990**, *94,* 1440.

73. R. G. Alden, M. R. Ondrias, S. Courtney, E. W. Findson and J. M. Friedman, *J. Phys. Chem.*, **1990**, *94,* 85.

74. R. G. Alden, M. D. Chavez, M. R. Ondrias, S. Courtney and J. M. Friedman, *J. Am. Chem. Soc.* **1990**, *112,* 3241.

75. G. H. Atkinson, T. L. Brack, D. Blanchard and G. Rumbles, *Chem. Phys.* **1989**, *131,* 1.

76. T. L. Brack, J. K. Delaney, G. H. Atkinson, A. Albeck, M. Sheves and M. Ottolenghi, *Biophys. J.* **1993**, *65,* 964.

77. J. K. Delaney, T. L. Brack, G. H. Atkinson, and M. Ottolenghi, N. Friedman and M. Sheves, *J. Phys. Chem.* **1993**, *97,* 12416.

78. W. L. Weaver, L. A. Huston, K. Iwata and T. L. Gustafson, *J. Phys. Chem.*, **1992**, *96,* 8956.

79. R. M. Bulter, M. A. Lynn and T. L. Gustafson, *J. Phys. Chem.*, **1993**, *97*, 2609.

80. C. K. Johnson, G. A. Dalickas, S. A. Payne and R. M. Hochstrasser, *Pure & Appl. Chem.* **1985**, *57*, 195.

81. *Porphyrins: Excited State Dynamics*, M. Gouterman, P. M. Rentzepis, K. M. Smith and D. A. Goff ed., Am. Chem. Soc., Washington D. C., 1986.

82. C. Varotsis and G. T. Babcock, *Biochem.* **1990**, *29*, 7357.

83. C. Varotsis, W. H. Woodruff and G. T. Babcock, *J. Am. Chem. Soc.* **1989**, *111*, 6439.

84. C. Varotsis, W. H. Woodruff and G. T. Babcock, *J. Am. Chem. Soc.* **1990**, *112*, 1297.

85. C. Varotsis, Y. Zhang, E. H. Appleman and G. T. Babcock, *Proc. Natl. Acad. Sci. USA*, **1993**, *90*, 237.

86. T. Ogura, S. Takahashi, S. Hirota, K. Shinzawa-Itoh, S. Yoshikawa, and T. Kitagawa, *J. Am. Chem. Soc* **1990**, *112*, 5630.

87. T. Ogura, S. Takahashi, S. Hirota, K. Shinzawa-Itoh, S. Yoshikawa, E. H. Appleman and T. Kitagawa, *J. Am. Chem. Soc* **1993**, *115*, 8527.

88. S. Han, Y.-C. Ching and D. L. Rousseau, *Nature* **1990**, *348*, 89.

89. R. A. Marcus and N. Sutin, *Biochim. Biophys. Acta*, **1985**, *811*, 265.

90. M. Bixon and J. Jortner, *J. Chem. Phys.*, **1986**, *90*, 3795.

91. M. Bixon and J. Jortner, *Faraday Discuss. Chem. Soc.*, **1982**, *74*, 17.

92. F. M. Harold, *The Vital Force, A Study of Bioenergetics* **1986**, W. H. Freeman.

93. S. D. Fuller, R. A. Capaldi and R. Henderson, *J. Mol. Biol.* **1979**, *134*, 305.

94. R. A. Capaldi F. Malatesta and V. M. Darley-Usmar, *Biochim. Biophys. Acta.* **1983**, *726*, 135.

95. J. M. Valpuesta, R. Henderson and T. G. Frey, *J. Mol. Biol.* **1990**, *214*, 237.

96. M. Wikstrom, M. Saraste and T. Penttila, in *The Enzymes of Biological Membranes* Vol. 4 ed. A. N. Martonosi, **1985**, p. 111.

97. G. T. Babcock and M. Wikstrom, *Nature* **1992**, *356*, 301.

98. S. I. Chan and P. M. Li, *Biochem.* **1990**, *29*, 1.

99. Q. Gibson and C. Greenwood, *Biochem. J.* **1963**, *86*, 541.

100. C. Greenwood and Q. Gibson, *J. Biol. Chem.* **1967**, *242*, 1781.

101. R. S. Blackmore, C. Greenwood and Q. Gibson, *J. Biol. Chem.* **1991**, *266*, 19245.

102. M. I. Verhovsky, J. E. Morgan and M. Wikstrom, *Biochem.* **1994**, *33*, 3079.

103. M. Oliveberg and B. G. Malmstrom, *Biochem.* **1992**, *31*, 3560.

104. B. C. Hill, *J. Biol. Chem.* **1991**, *266*, 2219.

105. O. Einarsdottir *et al*, *Biochem.* **1993**, *32*, 12013.

106. O. Einarsdottir, P. M. Killough, J. A. Fee and W. H. Woodruff, *J. Biol. Chem.* **1989**, *264*, 2405.

107. P. O. Stoutland, R. B. Dyer and W. H. Woodruff, *Science* **1992**, *257*, 1913.

108. W. Li and G. Palmer, *Biochem.* **1993**, *32*, 1833.

109. J. P. Hosler et al, *J. Bioener. Biomem.* **1993**, *25*, 121.

110. L. K. Hanson, in *Chlorophylls* p. 993, ed. H. Scheer, CRC Press, **1991**.

111. I. Bytheway and M. B. Hall, *Chem. Rev.* **1994**, *94*, 639.

112. J. E. Ridley and M. C. Zerner, *Theoret. Chim. Acta*, **1973**, *32*, 111.

113. A. D. Bacon and M.C. Zerner, *Theoret. Chim. Acta*, **1979**, *53*, 21.

114. M. C. Zerner, G. Loew and R. F. Kirchner, *J. Am. Chem. Soc.* **1980**, *102*, 589.

115. J. D. Head, M. C. Zerner and B. Weiner, *Chem. Phys. Lett.* **1986**, *131*, 359.

116. M
3
117. J.
M
118. M
1
119. G
120. M

116. M. C. Zerner, J. Mckelvey and W. D. Edwards, *Theoret. Chim. Acta,* **1987,** *72,* 347.

117. J. A. Pople and D. L. Beveridge, *Approximate Molecular Orbital Theory,* McGraw-Hill, New York , **1970.**

118. M. J. S. dewar, J. A. Hashmall and C. G. Venier, *J. Am. Chem. Soc* **1968,** *90,* 1953.

119. G. M. Zhidomirov and N. D. Chuvylkin, *Chem. Phys. Lett.* **1972,** *14,* 52.

120. M. Plato, W. Lubitz F. Lendzian and K. Mobius, *Isr. J. Chem.* **1988,** *28,* 109.

PIC
AND SEN
OF MG-FI

The photo
and free b
time-resol
separated
within 50
observed
Fujita *et a*
comparing
monomer
H_2 diporp
porphyrin
porphyrin
interpreted
INDO/1 a
the model

* Part of
Schmidt

CHAPTER TWO

PICOSECOND TIME-RESOLVED RESONANCE RAMAN SPECTROSCOPY AND SEMI-EMPIRICAL CALCULATIONS OF THE CHARGE SEPARATED STATE OF MG-FREE BASE DIPORPHYRINS*

Summary

The photoinducted charge separated state of a covalently linked magnesium porphyrin and free base porphyrin heterodimer complex (Mg-H_2) was investigated by picosecond time-resolved, two-color, pump-probe resonance Raman spectroscopy. The charge separated state is detected within 30 psec of laser excitation; recombination occurs within 500 psec. The time scales of the charge transfer and recombination processes observed by Raman are consistent with those measured earlier by optical methods (I. Fujita *et al*, J. Phys. Chem. 86 (1982) 3754). The vibrational data were analyzed by comparing with resonance Raman spectra of ground state diporphyrin complexes and monomer porphyrin cation and anion radicals. In the charge separated state of the Mg-H_2 diporphyrin complex, vibrational mode correlation showed that the magnesium porphyrin cation half of the dimer is in its $^2A_{1u}$ electronic state. The free base porphyrin anion half of the charge transfer state has vibrational characteristics that are interpreted in terms of data available on the free base octaethylporphyrin anion. INDO/1 and INDO/s calculations on such diporphyrin model compounds also support the model of vibrational-electronic coupling we employed here.

---

* Part of results published on *Phys. Chem. Lett.* **1995**, *234*, 133 (Co-authors with E. Schmidt, W. Wu, C. K. Chang and G.T. Babcock.

2.1 Introd

The
solar ener
The initia
the transie
anion [1]
therefore,
process.
such as s
recombin
studied b
[14] and

In
macrocyc
categorie
macrocyc
occurs be
which ca
relationsl
photoind
processes
photoind
steps tha
recombin
systems t

2.1 Introduction

The photosynthetic reaction center is a protein complex that converts captured solar energy into electrical and chemical energy in the first steps of photosynthesis. The initial charge separation in the bacterial photosynthetic reaction center results in the transient formation of a bacteriochlorophyll dimer cation and a bacteriopheophytin anion [1]. The structure and electronic properties of this cation-anion radical pair are, therefore, likely to be key to understanding the mechanism of the charge separation process. In order to gain insight into factors that control the charge separation process, such as structural conformation, energy transfer, bond distance, solvation and charge recombination, different diporphyrin model compounds have been developed [2] and studied by transient absorption spectroscopy [3-12], emission spectroscopy [13], EPR [14] and X-ray crystallography [15-17].

In general, research work on photoinduced electron transfer involving macrocyclic complex of porphyrin and chlorophylls can be divided into three categories. First, a number of experiments investigate electron transfer between macrocycles [3-4, 9-13]. Since the primary electron separation in photosynthesis occurs between chlorophylls, it is important to understand these macrocycle structures which can localize and stabilize the charges. Second, much work has been done on relationships of distance, free energy, solvent effect, structural dependence of both photoinduced charge separation reactions and subsequent charge recombination processes [5, 6]. Third, since, in photosynthetic charge separations, an initial photoinduced charge separation is followed by a sequence of dark electron transfer steps that proceed at rates sufficiently fast to compete with the series of back-electron recombination processes, several studies have focused on developing supramolecular systems that mimic the stepwise nature of this process. Such work includes porphyrin-

porphyri

porphyri

Se

properti

fluoresc

generall

techniqu

On the c

resolved

incident

process.

porphyri

monome

heterodi

ground

reduced

not yet

spectros

The resu

porphyri

monitor

extended

In

pump-pr

covalent

(Mg-H_2)

photoexc

porphyrin-quinone complexes [18-22], porphyrin-carotenoids complexes [23], porphyrin-polyene-quinone complexes [24].

Several spectroscopic methods can produce information on internal vibrational properties of macromolecules. They include neutron scattering, resonance fluorescence, optical absorption, IR and Raman. However, as these methods produce generally broad electronic linewidths when applied to macromolecules, most of these techniques give much less information in the condensed phase than in the gas state. On the other hand, resonance Raman produces sharp line spectra that contained well-resolved vibrational information as phase relationships are retained between the incident monochromatic laser light and the scattered photons in Raman scattering process. With its unique advantage of being able to detect structural changes in the porphyrin macrocycle, resonance Raman spectroscopy has been used to examine monomeric cation [25-29] and anion porphyrin radicals [30-33], chlorophyll-porphyrin heterodimer [34] and sandwich type diporphyrins [35 and references therein]. The ground state orbital assignments and vibrational properties of these oxidized and reduced porphyrin systems are reasonably well understood. Although its potential has not yet been fully exploited in excited state studies, time resolved resonance Raman spectroscopy has been used to monitor the excited porphyrin triplet state [32, 36-40]. The results indicated that dynamic Jahn-Teller distortion plays an important role in the porphyrin triplet excited state and showed that Raman scattering was a useful tool to monitor excited state dynamics. The excited state Raman approach has recently been extended to the picosecond time scale and metalloporphyrin excited singlet states [41].

In the work here, we report the use of picosecond time-resolved, two color pump-probe resonance Raman to detect directly the charge separated state of the covalently linked magnesium porphyrin and free base porphyrin heterodimer complex ($Mg\text{-}H_2$), a classic model compound which acquires charge transfer character upon photoexcitation [3-6], shown in Figure 1. Our experimental results indicate that, in the

Figure 2.1. Mg-H_2 diporphyrin complex.

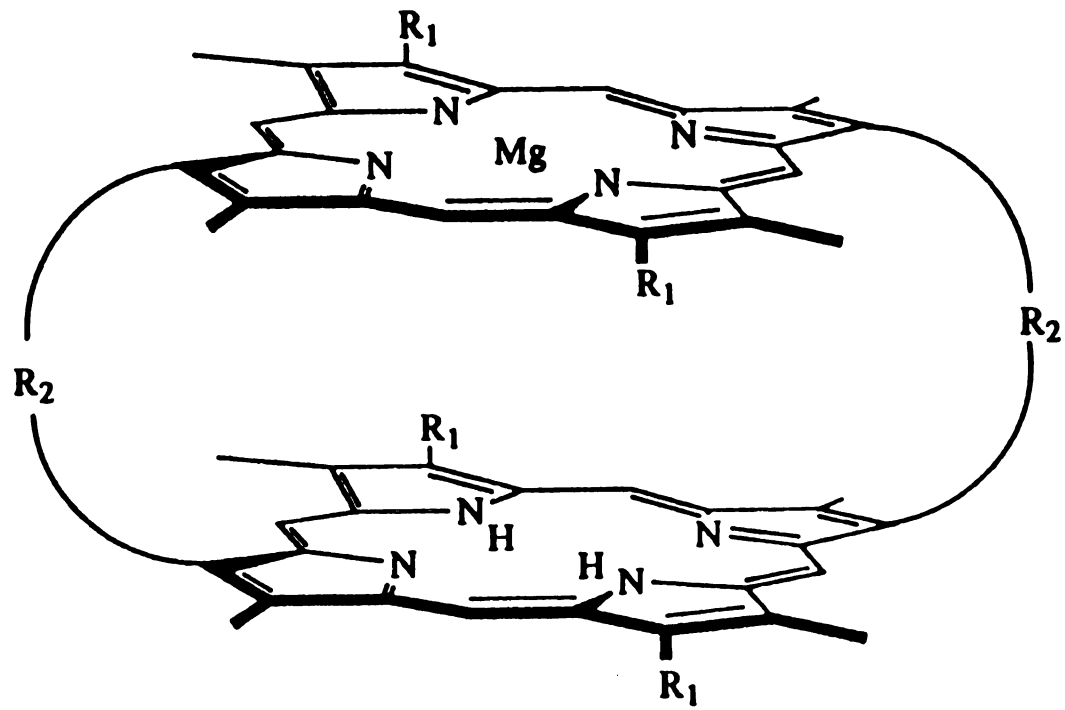

R_1 = n-octyl, R_2 = $-CH_2-\underset{\underset{O}{\|}}{C}-N(n\text{-butyl})-CH_2-CH_2-$

high f

interpr

anion

and m

separat

resolve

2.2 Ge

M

were ki

the pro

methyle

we re

spectro

413.1 n

Laser p

Spex 1

Spectru

2.3 Inst

Th

experim

instrume

modified

time-resc

MHz, 70

to pump

high frequency region, the Raman bands of the charge separated state can be interpreted within the context of the Raman shifts of monomer porphyrin cation and anion radicals. These results are explained within Gouterman's model for porphyrin and metalloporphyrin orbital occupancy [42]. Our work shows that the charge separated state of an optically excited porphyrin complex can be assessed by time-resolved resonance Raman spectroscopy.

2.2 General Experimental Section

Mg-H_2 diporphyrin compounds and most of other metal and free base porphyrins were kindly provided by Dr. Chang's lab. They were synthesized and purified by using the procedures described by Chang and co-workers [43]. Spectroscopic grade methylene chloride (J. T. Baker) was used as the solvent in the spectroscopic studies we report. Absorption spectra were recorded on a Perkin-Elmer λ-5 spectrophotometer. The cw resonance Raman spectra were obtained by using the 413.1 nm laser line of a Coherent K^+ laser or the 441.6 nm line of a He-Cd laser. Laser power was about 15 mW at the sample. Raman scattering was dispersed into a Spex 1877 triplemate monochromator and recorded by a CCD detector (Spex Spectrum One).

2.3 Instrumentation of time-resolved resonance Raman set-up

The picosecond Raman set-up has been crucial to the success of those experiments we designed and much effort of this thesis work has been on the instrumentation. During a period of about five years, the instruments have been modified several times and have improved significantly. In an early version of our time-resolved Raman set-up, a Coherent 76s Antare laser produced a pulse train of 32 MHz, 70 picoseconds at 532 nm. This seeding picosecond laser with 1.2 W was used to pump a Coherent 702 dye laser. The output pulse from the dye laser at

Figure 2.2 **The picosecond time-resolved resonance Raman set-up.**

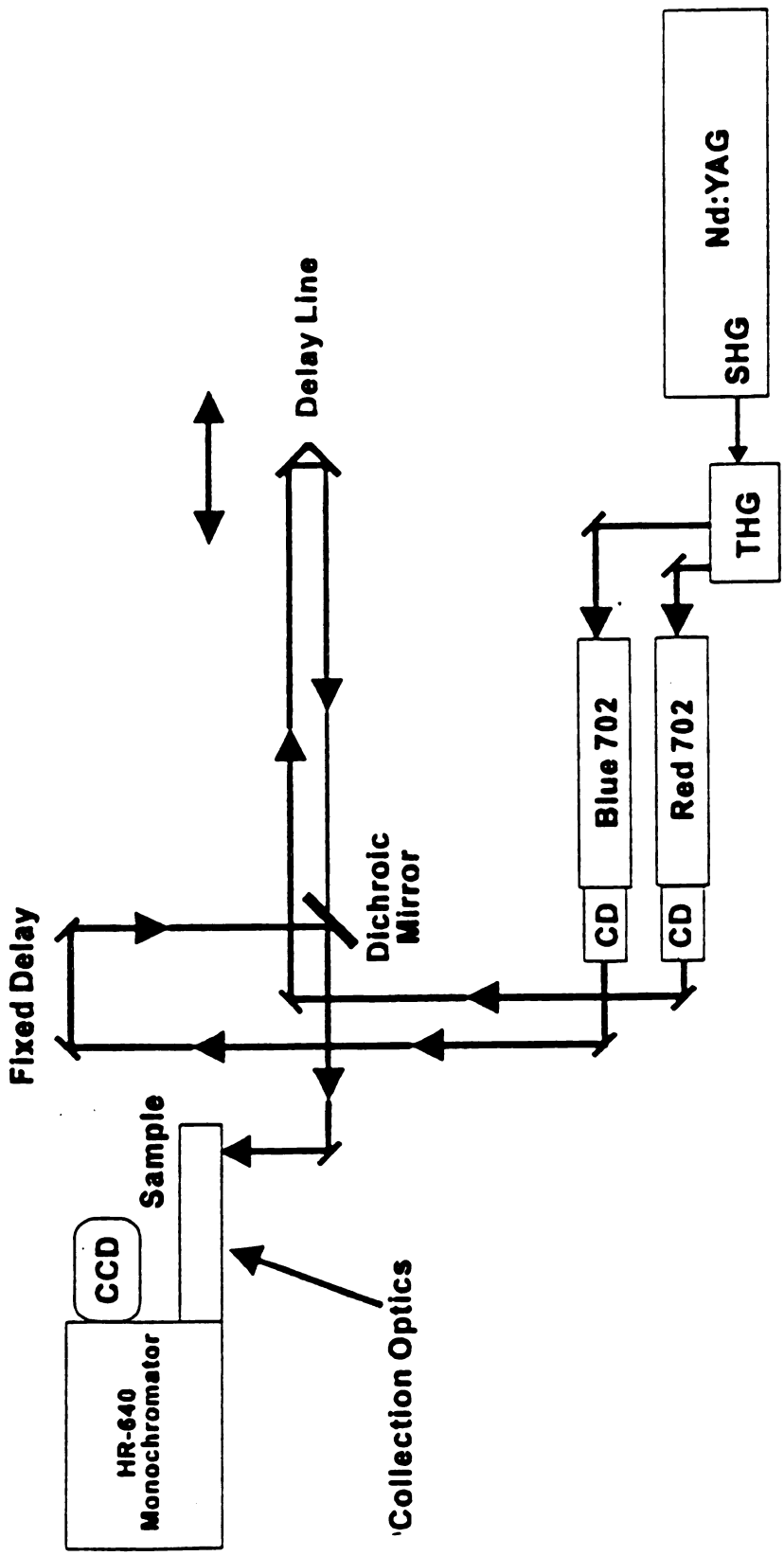
Nd:YAG
SHG
THG
Delay Line
Blue 702
Red 702
CD
CD
Dichroic Mirror
Fixed Delay
Sample
CCD
HR-640 Monochromator
Collection Optics

580 nm wit
excimer las
and 680 nr
resonance
repetition
large amo
of peak p
green reg

The
given in
with secc
mW), an
a cavity
used Stil
operated
MHz re
laser an
auto co
High g
minimiz
correspo
charge
in the S
chosen t
blue dye
yellow
were con

580 nm with about 50 mW was then amplified by a dye amplifier pumped by an excimer laser. After the Raman shift cell, two wavelengths, 580 nm (fundamental) and 680 nm (first Stokes shift) were available with enough power for time-resolved resonance Raman experiments. The long duration pulse (17 ~ 22 ns) and low repetition rates (10 to 50 Hz) of the excimer laser led to inefficient dye pumping, to a large amount of amplified spontaneous emission (ASE), and to non-linear fluctuation of peak power. The anti-Stokes laser line at 500 nm which covered the important green region, did not have sufficient power and stability for Raman scattering.

The picosecond Raman set-up we used in the experiments described here is given in Figure 2.2. It consisted of the Coherent mode-locked Antares Nd:YAG laser with second and third harmonic generators. The output beams at 355 nm (about 800 mW), and at 532 nm (2.2 W), were used to pump two dye lasers, each equipped with a cavity damper (Coherent models 702 and models 7200, respectively). One dye laser used Stilbene 420 with a tunable range of 425 nm to 460 nm, while the other dye laser operated with Rhodamine 6G and had a tunable range of 575 nm to 620 nm. At a 1 MHz repetition rate, the typical output energy/pulse was 110 nJ for the yellow dye laser and 35 nJ for the blue dye laser. Both pulses had a FWHM = 4 - 5 psec in their auto correlation traces without any further assumption of pulse shape correction. High grade (λ=1/10) refractive optics were used in the beam pathway in order to minimize pulse broadening. The pump beam was tuned to 580 nm, which corresponds to one of the Q band peaks of Mg-H_2 (see Fig. 2.7 below). For the charge separated state, there is a broad absorption band in the charge separated state in the Soret region from about 400 nm to 460 nm [6, 12]. The probe beam was chosen to be 430 nm because this wavelength is close to the maximum output of our blue dye laser. The 430 nm blue beam traversed a fixed distance and the 580 nm yellow beam was directed through a variable optical delay line. The two beams were combined at a dichroic mirror. The collimated beams were then focused onto the

sample by

were meas

section for

yield proc

conditions

order to a

a backsca

light was

of the res

spectrogr

Model LN

using the

trace amo

sample u

and after

during th

also perfo

The

the exper

monochro

(a) Focusi

In or

power of o

spot size

photoexcite

detection. T

sample by a doublet lens (Newport, model PAC058). The sizes of the focused spots were measured as 30 μm for 580 nm and 28 μm at 430 nm (please see the following section for details). Resonance Raman scattering is a low-probability, low-quantum yield process, and therefore requires high irradiance at the sample. Resonance conditions involve high electronic absorption and hence heating of the sample. In order to avoid the heating problems, samples were spun in a cylindrical quartz cell and a backscattering geometry with an angle of ~135^{o} was used. The Raman scattered light was passed through a narrow beam filter centered at ~ 440 nm in order to get rid of the residual scattered yellow pumping beam, before it was collected with a single spectrograph (ISA, THR 640) and detected by a CCD detector (Princeton Instruments Model LN1152/UV with EEV 1154x298 chip). Samples were degassed three times by using the freeze-pump-thaw method on a vacuum line. This procedure is important as trace amount of oxygen dissolved in the solution may cause the photooxidation of the sample under repetitive laser pulses [44]. Absorption spectra were checked before and after each Raman measurement and indicated that sample damage did not occur during the Raman measurements. Further control resonance Raman experiments were also performed to insure the sample integrity.

There are several major factors in the instrument that are key to the success of the experiment. They are focusing spot size, optical aberration, and optimization of monochromator and detector. We discuss them separately as following.

(a) Focusing spot size

In order to take the advantage of the high laser pulse repetition rate, low peak power of our experimental set-up, a tight focusing at the sample is desired. A smaller spot size will lead to a larger amount of molecules being pumped into the photoexcited state for further photophysical process and, therefore, for Raman detection. The theoretical focus spot size is given by

Figure 2.3 a). average power dependence of pulse repetition rates at 580 nm and;
b). peak power dependence of pulse repetition rate at 580 nm.

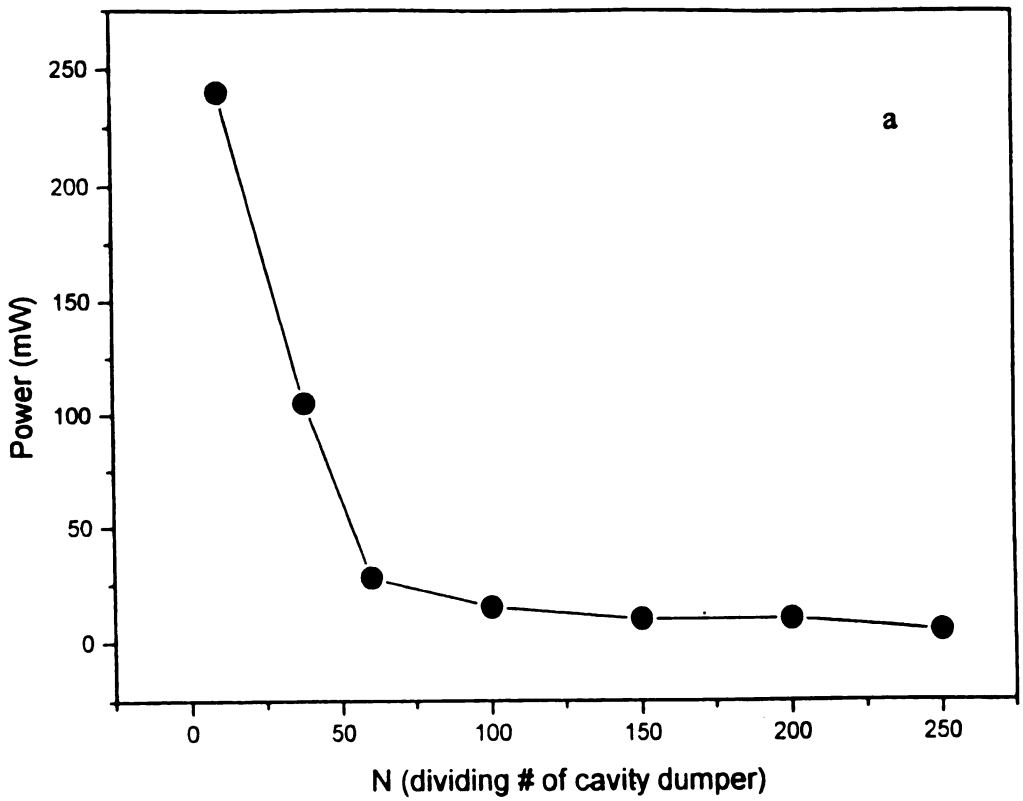
a
Power (mW)
250
200
150
100
50
0
0
50
100
150
200
250
N (dividing # of cavity dumper)

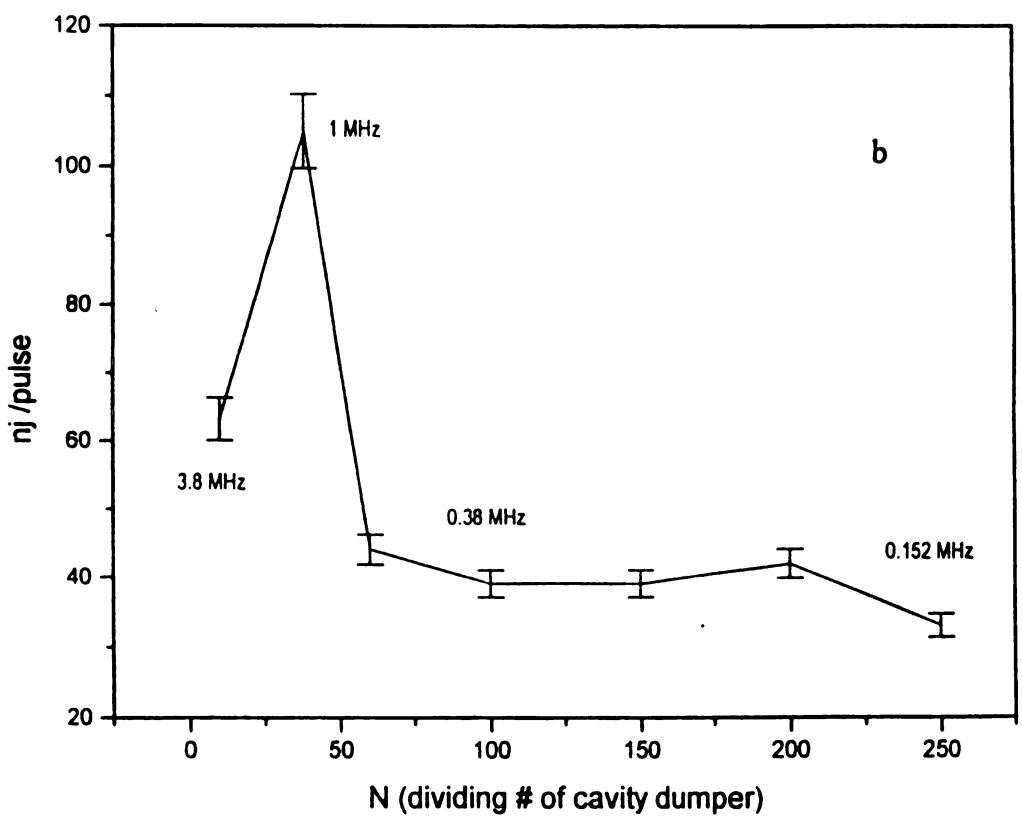
b
nj /pulse
120
100
80
60
40
20
1 MHz
3.8 MHz
0.38 MHz
0.152 MHz
0
50
100
150
200
250
N (dividing # of cavity dumper)

Figure 2.4 Measurements of the spot size at focus point for a 6' doublet at a).580 nm; b). 430 nm.

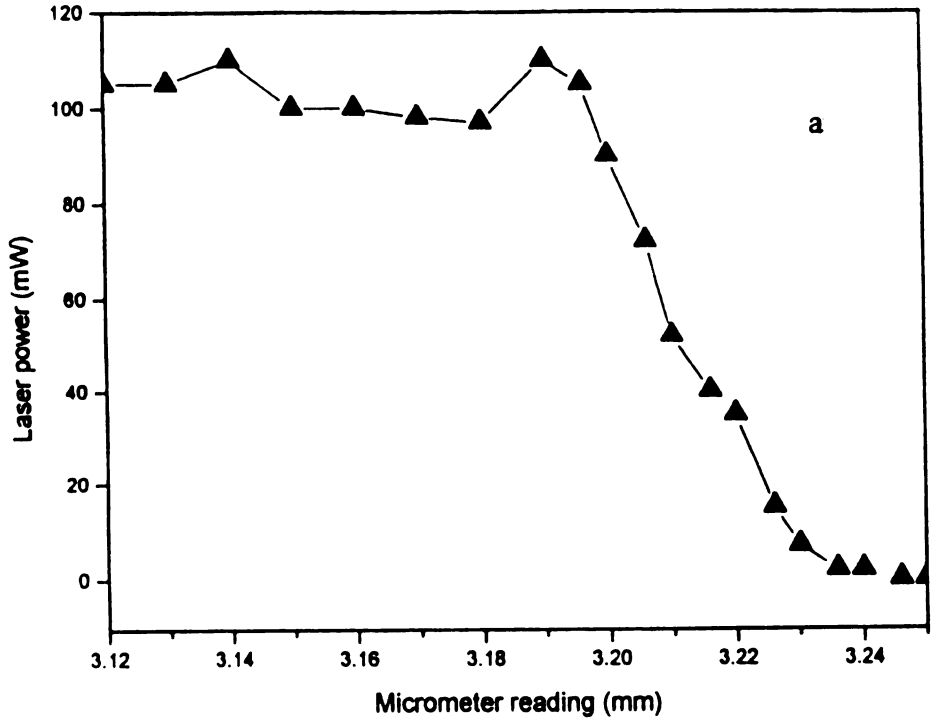
120
100
80
60
40
20
0
Laser power (mW)
a
3.12
3.14
3.16
3.18
3.20
3.22
3.24
Micrometer reading (mm)

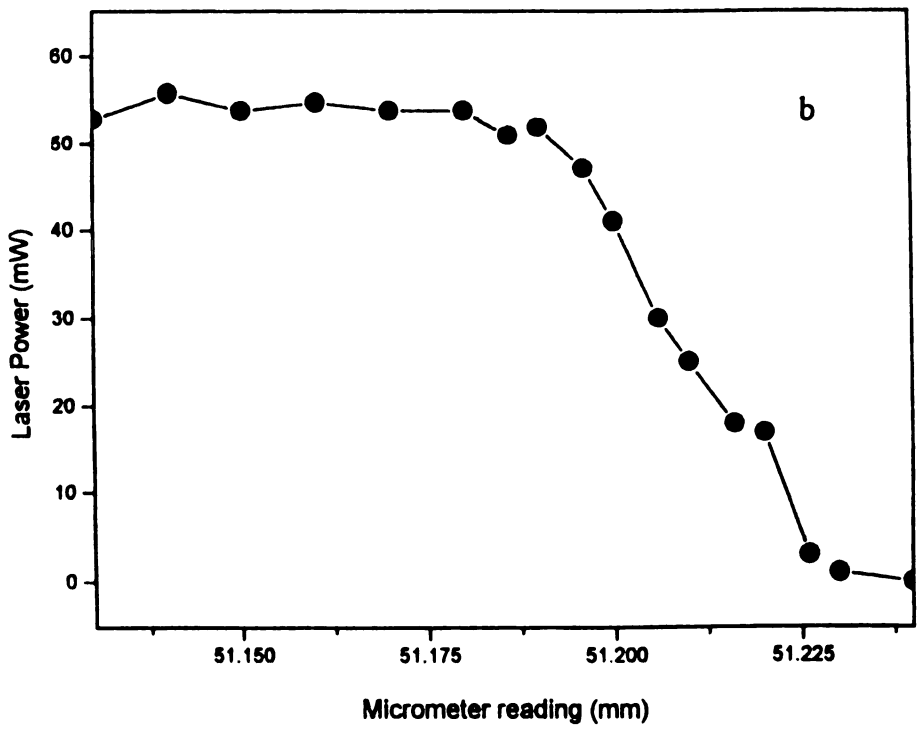
60
50
40
30
20
10
0
Laser Power (mW)
b
51.150
51.175
51.200
51.225
Micrometer reading (mm)

Figure 2.5 The collection optics for resonance Raman experiments.

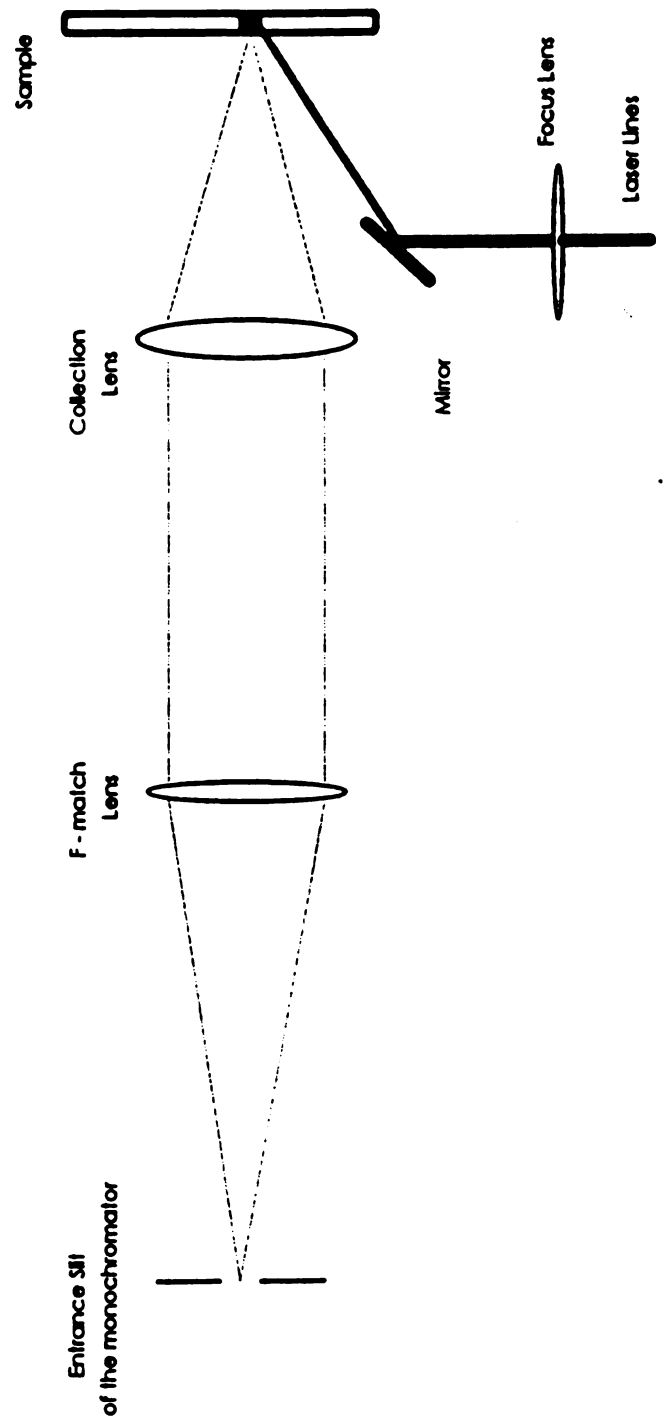
Sample
Focus Lens
Laser Lines
Collection Lens
Mirror
F - match Lens
Entrance Slit of the monochromator

$S =$

wher

diam

lengt

lense

aberr

wave

suitat

from

mode

both

focus

whicl

result

acros

the c

of the

focus

(b) T

operat

with v

called

spectru

$$S = 2.44\ \lambda * (f / D) \qquad (2.1)$$

where λ is the wavelength used, f is the focal length of the lens and, D is the diameter of the focusing lens. According to this equation, a lens with short focus length and large diameter will give a small focused spot. Although specially designed lenses, such as best-form lenses which are designed to minimize the spherical aberration over a narrow range of wavelengths, will give the perfect images at specific wavelength regions for the propagation of a single incoming Gaussian beam, it is not suitable for our task as our experiments have to cover a wide range of wavelengths, from about 600 nm to 400 nm. The lens we chose was a six inch doublet (Newport, model PAC058) that has taken consideration of the chromatic aberration, as we used both blue and yellow laser lines simultaneously in our experiments. The sizes of the focused spots were measured by both pinholes and a standard night-forge experiment, which correlated the optical power and focusing spot size. Figure 2.3 and 2.4 gave the results of the night-forge experiments. In brief, a sharp edge razor was moved slowly across the focus point as the transmitted laser power was recorded. The diameter of the central spot, the so-called the Airy disc, is defined as containing 86.5% ($1 - 1/e^2$) of the total optical energy. The experimental results and theoretical calculation of the focusing spot size were given in Table 1.

(b) The chromatic aberration

When a lens or a optical system uses many wavelengths at the same time or operates a continuum of wavelengths, as the refractive index of optical material varies with wavelength, the focal properties of a simple lens will vary as well. This is so-called chromatic aberration. Glasses exhibit normal dispersion in the visible spectrum, so the refractive index is higher for blue light than for red light. The ability

of the lens to bend rays is thus stronger in the blue, and the focal length of a convex glass lens is shorter for blue light than for red light. In order to avoid this type of optical aberration, one must use achromatic doublet lenses. A typical doublet consists of two lenses of different optical glasses placed in close contact. The two lenses have a common radius of curvature so that they fit intimately over their entire surface. An index-matched cement is used to eliminate the individual reflections from the two interior surfaces. By a proper choice of glasses, the doublet can have the same focal lengths for the designed wavelengths. In light of above consideration, a six inch diffraction limited achromatic doublet (Newport PAC058) was used in our two color, time-resolved experiments.

(c) Optimization of the monochromator and detector system

The rigorous characterization of the dispersion of a monochromator is given by its F number. How the F number of a monochromator is calculated is a complicated procedure. However the F number can be interpreted approximately as the ratio of the axial distance from entrance slit to the holographic grating and the diameter of the grating. In order to avoid underfilling or overfilling of the monochromator grating, the collection optics were designed so that they matched the F number of the monochromator (Figure 2.5). The monochromator and detector were aligned with the standard procedure suggested in the ISA instrumental manual. First, with the mirror masks, a He-Ne laser line at 632.8 nm was aligned through the collection optics and the centers of the mirrors and grating of the monochromator. Further optimization was then done by using the image mode of the CCD detector, i.e., at a small aperture of the entrance slit, a sharp mercury line was imaged at the CCD detector; by adjusting the detector position a sharp, even image was centered. This image was moved horizontally on the CCD chip when the monochromator grating was moved. However the above image was always at the vertical center of the CCD chip for a good

alignment,. Finally, different mercury lines were tested for correct wavelength and maximum intensity. The monochromator resolution was optimized by using CCl_4 triplet solvent lines. These three lines were distinguishable at a 10 μm entrance width. In practical time-resolved experiments, a 5 mm height and a 120 μm width of the entrance slit was used, which results in a spatial resolution of 4~5 cm^{-1}.

Throughput optimization is one of the most challenging topics in spectrometer performance. After careful alignment and optimization of the J-Y R640 single monochromator and collection optics, we setup for the picosecond time-resolved Raman experiments by carrying out an estimate of throughput factors for both the R650 and a standard OMAIII triplemonochromator routinely used in the laser lab. This ratio was then compared with the experimental data in order to characterize the efficiency of the J-Y R640 monochromator. The monochromator throughput factor is the product of the source area viewed, the solid angle collected by the monochromator, the transmission factor of the monochromator optics, and the slit function. The final equation for throughput factor is given by [46]

$$\Phi_o = B_\lambda W^2 H \Omega T_{op} R_d \qquad (2.2)$$

where B_λ is the source spectral reliance. At the same laser power level, it is close to the same for both the R640 single monochromator and the OMAIII. W is the entrance slit width and H is the entrance slit height of the monochromator, respectively. The Ω is the solid angle of the monochromator, which is defined as

$$\Omega = \frac{\pi / 4}{(F / n)^2} \qquad (2.3)$$

f/n is the f number of the monochromator. For R640 single monochromator and OMAIII, f/n is 5.7 and 10, respectively. T_{op} is a factor that accounts for the effect of

absor

and g

disper

R_d

f is th

monoc

Table

OMA

$$\frac{\Phi}{\Phi_0}$$

Howev

single

OMAI

ratio o

Photon

absorption, refection and scattering loss of the optical components. For each mirror and grating, the optical intensity will decrease by about 4%. R_d is the reciprocal linear dispersion of the monochromator, which is given by

$$R_d = \frac{\lambda \cos\beta}{f(\sin\alpha + \sin\beta)} \tag{2.4}$$

f is the f number of the focusing lens, α and β are entrance and dispersion angle of the monochromator, respectively. The numerical values for the above factors are listed in Table 2.1. The throughput ratio for the J-Y R-640 single monochromator and the OMA III is

$$\frac{\Phi_o(R640)}{\Phi_o(OMAIII)} = 1.755 \tag{2.5}$$

However, in order to compare with the signals detected by the CCD detector from the single monochromator and the intensified photodiode array detector (IPDA) from the OMAIII triple monochromator, we must convert the above throughput ratio into the ratio of detector counts.

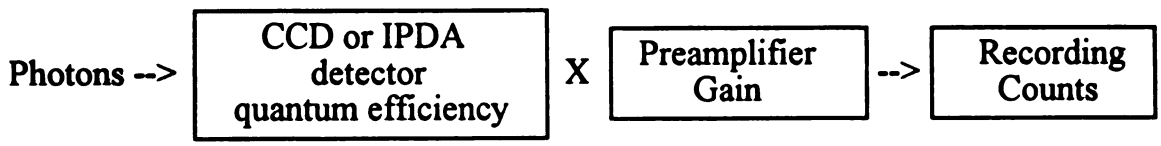

Table 2.1. Focusing Spot Size of the Six Inch Doublet Lens

Wavelength λ	D = 1 inch	D_{eff} = 0.35 inch	Exp.
580 nm	8.54 μm	24. 4 μm	30 μm
430 nm	6.23 μm	17.8 μm	28 μm

Table 2.2. Monochromator Paramaters Used for Throughput Factor Calculation

	B_λ	W	H	Ω	T_{op}	R_d
J-Y R-650	~ 1	100 μm	10 μm	0.8847	0.96^3	0.6 nm/mm
OMAIII	~ 1	100 μm	10 μm	0.6648	0.96^{10}	1.4 nm/mm

Table 2.3. Quantum Efficiency and Preamplifier Gain

at 440 nm	CCD (Princeton Blue coated 1152E)	IPDA
Quantum Efficiency	20 %	10 %
Preamplifier Gain	5 e^-/counts	1 e^-/counts
Photon/Count Convertion	25 photons/count	10 photons/count

At 440 nm, the quantum efficiency and preamplifier gain for both CCD and IPDA are listed in Table 2.2. Considering both throughput factors and detector efficiency, the ratio of the theoretical counts is estimated as

$$\frac{Counts(R650)}{Counts(OMAIII)} = \frac{\Phi_o(R650)*(CCD^{photon/count})}{\Phi_o(OMAIII)*(IPDA^{photon/count})} = 0.702 \qquad (2.6)$$

Considering three more slits in the filter stages in OMAIII, if 5% loss occurs on each slit, the above throughput ratio becomes

$$\frac{Counts(R650)}{Counts(OMAIII)} = 0.702/(0.95)^3 = 0.82 \qquad (2.7)$$

Under normal daily experimental conditions, J-Y monochromator with the LN1152/UV CCD can easily produce about 6000 counts/sec. while OMAIII with an IPDA detector generates about 4000 counts. This result (Table 2.3) demonstrates that the J-Y R-650 monochromator we setup works efficiently.

2.4 Results

The UV-visible absorption spectra of magnesium octaethylporphyrin (MgOEP), covalently linked magnesium-magnesium diporphyrin (Mg-Mg), and Mg-H_2 are shown in Figure 2.6. The Soret maxima for the two dimers are blue shifted relative to that of the monomer porphyrin. These spectral shifts are characteristic of porphyrin ring-ring interaction in the excited states and are attributed to exciton coupling in the diporphyrin complex [47-50]. This effect, which depends on the relative orientation of the monomer transition dipoles in the dimer, is such that the transition to the higher energy excited state is allowed and the transition to the lower

Figure 2.6 Absorption spectra of MgOEP, Mg-Mg and Mg-H_2 diporphyrins.

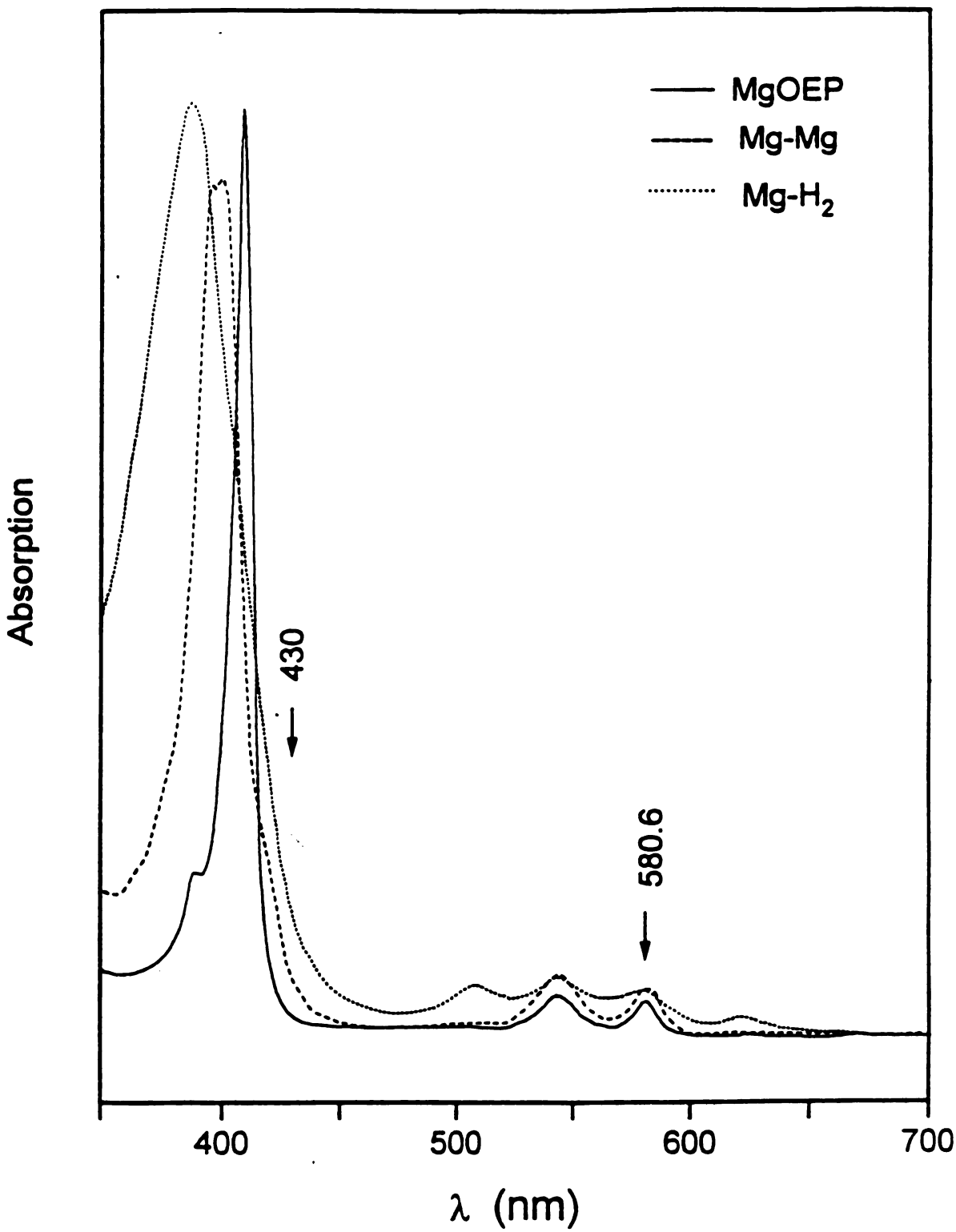
MgOEP
Mg-Mg
Mg-H2
Absorption
430
580.6
400
500
600
700
λ (nm)

Figure 2.7 Resonance Raman spectra of H_2OEP, MgOEP, Mg-Mg diporphyrin and Mg-H_2 diporphyrin complex. Excitation laser line is at 413.1 nm.

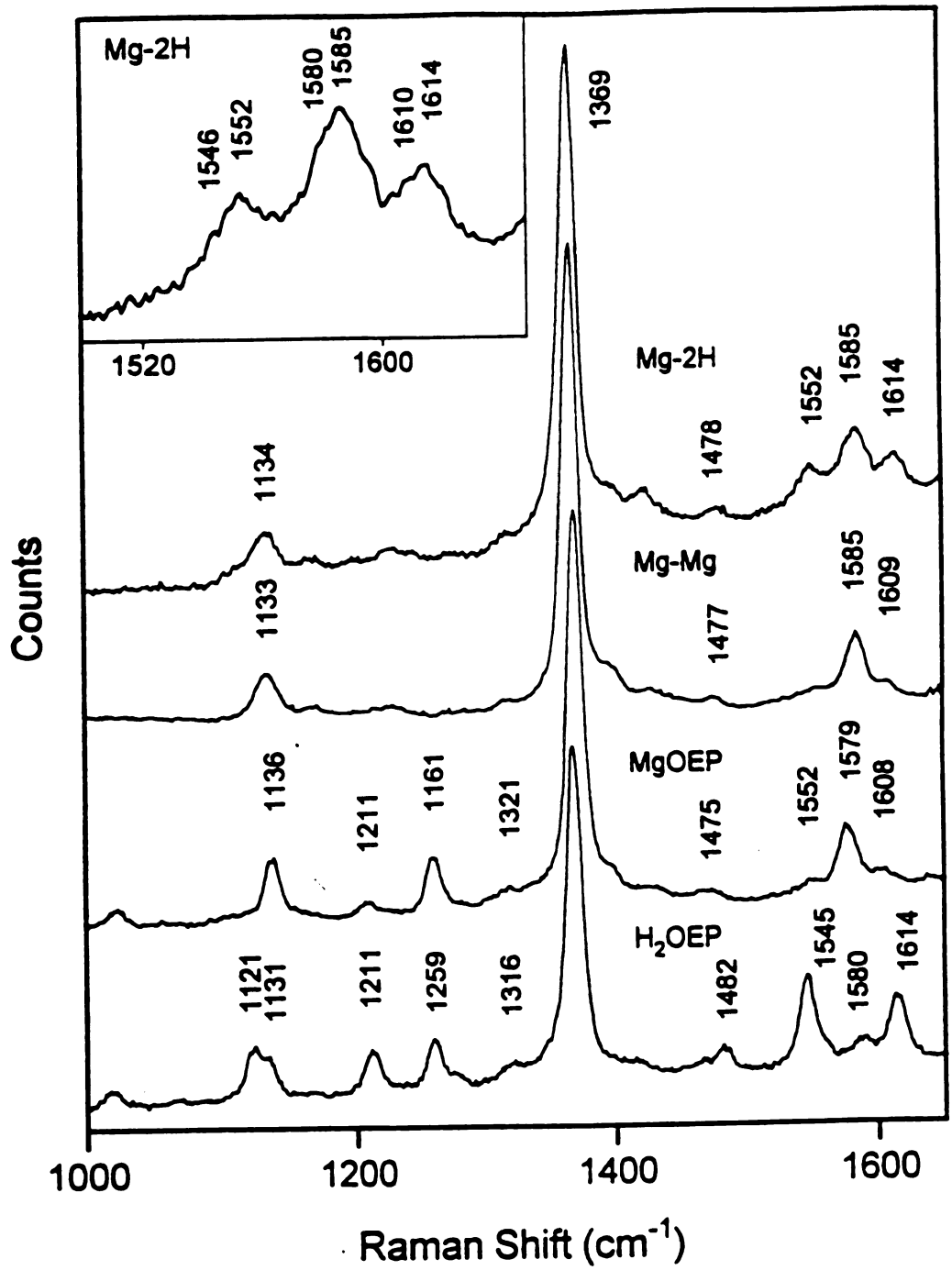
Mg-2H
1546
1552
1580
1585
1610
1614
1520
1600
1369
Mg-2H
1134
1478
1552
1585
1614
Mg-Mg
1133
1477
1585
1609
MgOEP
1136
1211
1161
1321
1475
1552
1579
1608
H2OEP
1121
1131
1211
1259
1316
1482
1545
1580
1614
Counts
1000
1200
1400
1600
Raman Shift (cm-1)

Figure 2.8 Two color pump-probe, time-resolved resonance Raman spectra of $Mg\text{-}H_2$ diporphyrin complex. (a). Probe beam only; (b). 30 psec delay; (c). 500 psec delay. The pump beam is at 580 nm. The probe beam is at 430 nm. Solvent peaks are marked with an asterisk (*).

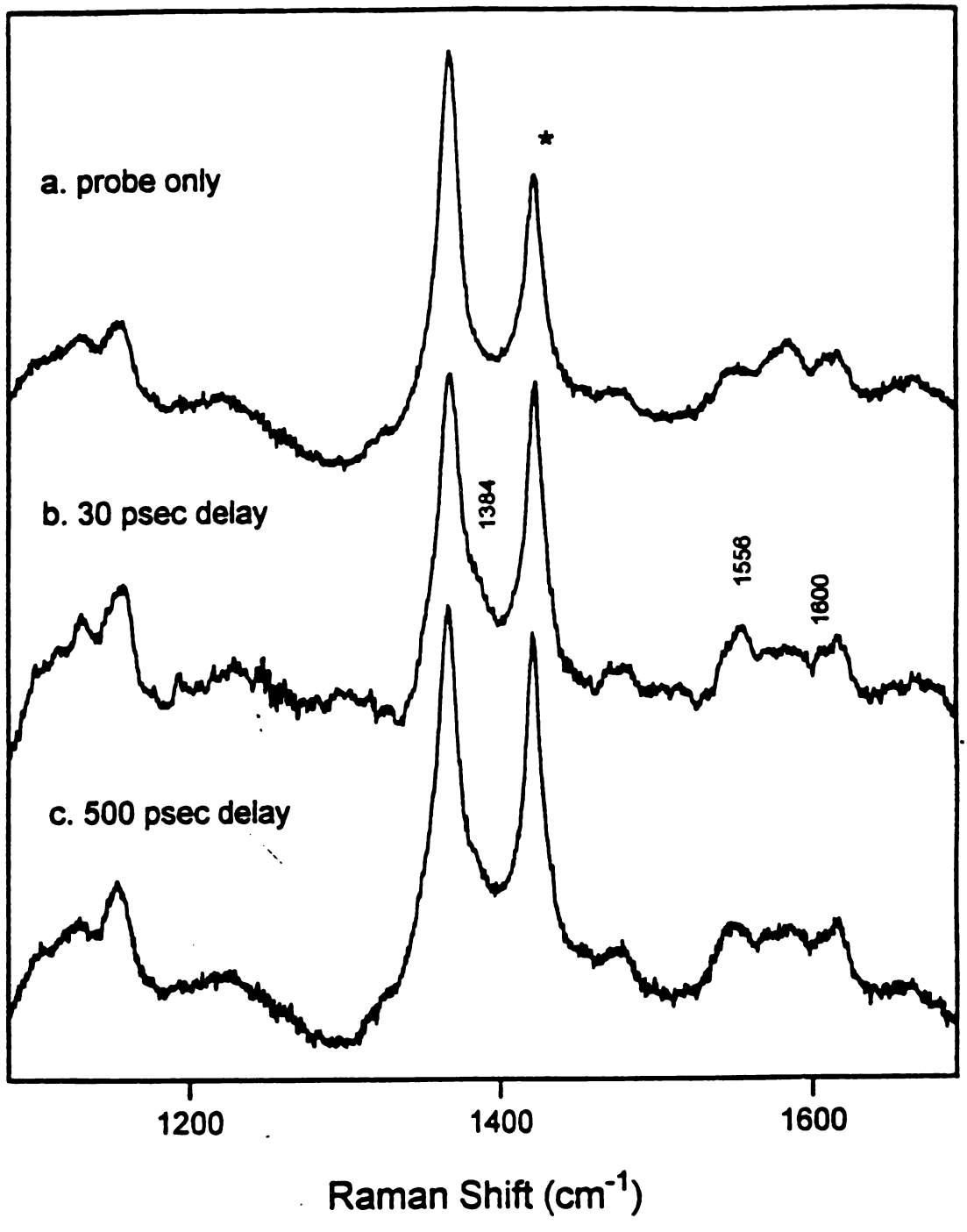
a. probe only
*
b. 30 psec delay
1384
1556
1600
c. 500 psec delay
1200
1400
1600
Raman Shift (cm-1)

Figure 2.9 Difference spectra of Mg-H_2 diporphyrin complex. (a). Spectrum (b) minus spectrum (a) of Fig. 2.8; (b). Spectrum (c) minus spectrum (a) of Fig. 2.8. Subtraction method is described in the text.

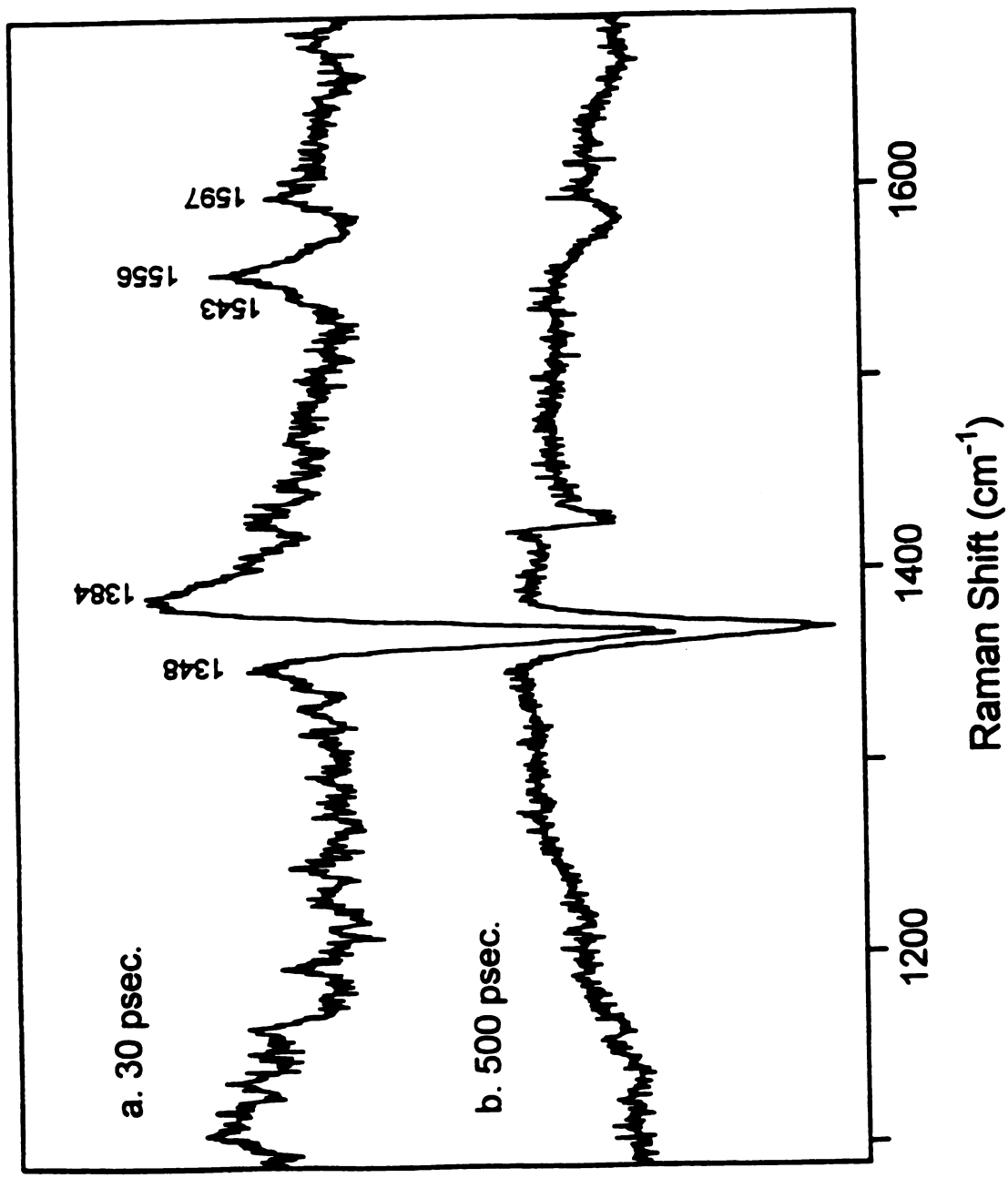
a. 30 psec.
b. 500 psec.
1348
1384
1543
1556
1597
1200
1400
1600
Raman Shift (cm-1)

Figure 2.10 Two color pump-probe, time-resolved resonance Raman spectra of Mg-H_2 diporphyrin complex taken at 2.0 ns delay, laser powers are 120 mW at 580 nm and 45 mW at 430 nm. spectrum a. the probe only spectrum; from b. to g. were taken at 5 minute accumulation for each spectrum; h. is the spectrum taken after sample has been under aser irradiance for 55 mininutes.

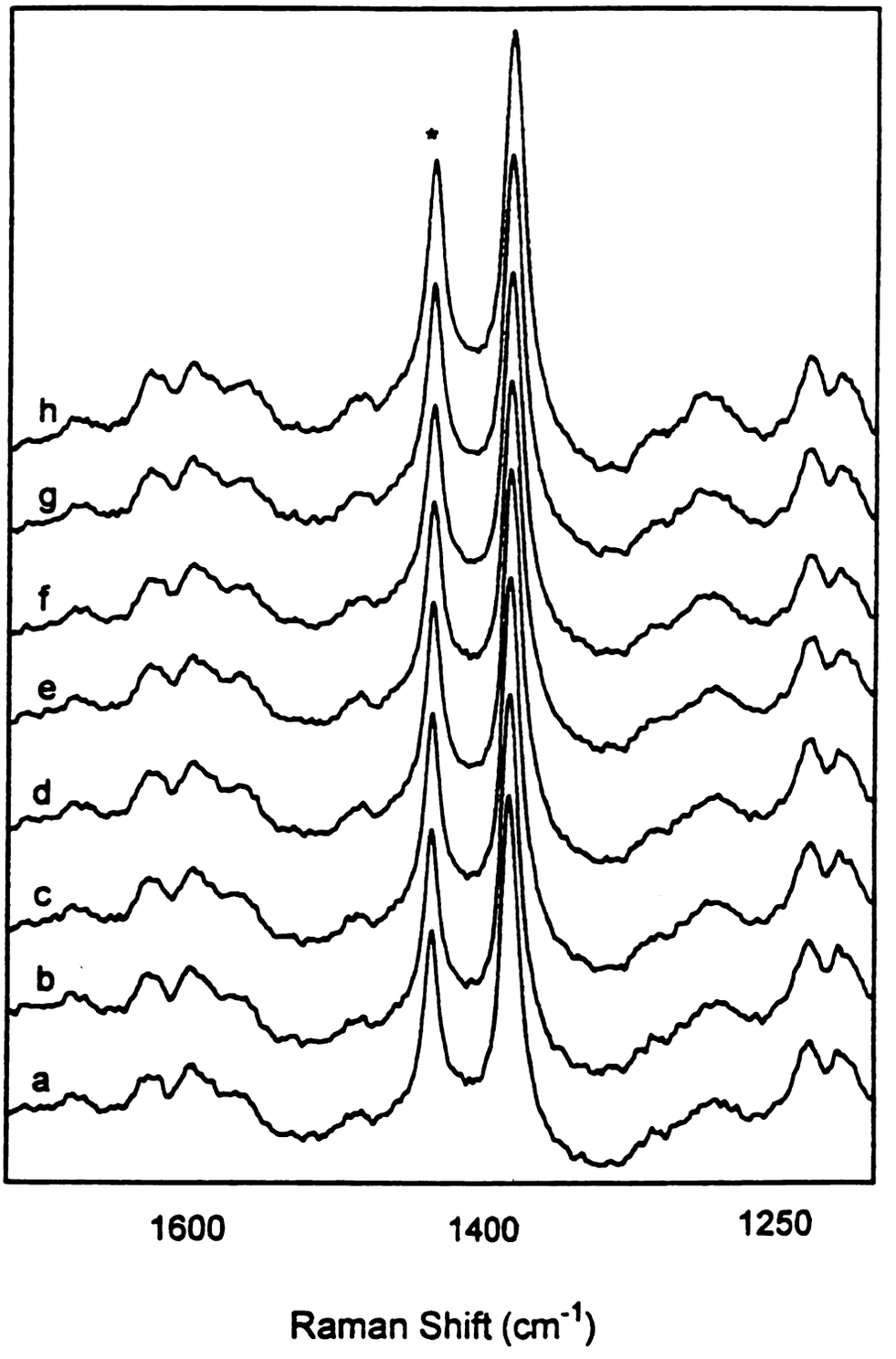
h
g
f
e
d
c
b
a
1600
1400
1250
Raman Shift (cm-1)

Table 2.4. Resonance Raman Frequencies (cm^{-1}) of Mg, Free Base Porphyrins, Mg-Mg Diporphyrin and Mg-H_2 Diporphyrin

	MgOEP	MgEtioP[a]	H_2OEP[b]	Mg-Mg	Mg-H_2[c]
υ_{10}	1608	____	1614	1609	1614 (H_2P)[d] 1610 (MgP)
υ_2	1579	1584	1580	1585	1585 (MgP) 1580 (H_2P)
υ_{11}	1552	1552	1545	____	1552 (MgP) 1546 (H_2P)
υ_3	1475	1477	1482	1477	1478
υ_{29}	1397	1397	____	____	____
υ_4	1371	1369	1369	1369	1369
CH2 wag	1321	1312	1316	____	____
CH2 twist	1261	1257	1259	____	____
υ_{13}	1211	1214	1211	____	1226
υ_5	1136	1135	1131	1133	1135

[a] Also from ref. [53]; [b] Also from ref. [33]; [c] This work; [d] H_2P and MgP are free base porphyrin half and Mg porphyrin half of the Mg-H_2 diporphyrin complex, respectively.

Table 2.5. Resonance Raman Frequencies (cm^{-1}) for Mg^{+}-$2H^{-}$ Diporphyrin Compounds and Their Corresponding Parent Cation and Anion Radicals

	ZnOEP	$ZnOEP^{+}$ [a]	MgOEP	$MgOEP^{+}$ [b]	H_2OEP	H_2OEP^{-} [c]	Mg-H_2	Mg^{+}-H_2^{-}
υ_{10}	1618	1617	1608	1610			1614	------
					1614	1604	1610	------
υ_2	1581	1600	1579	1598			1585	1597
					1580	1573	1580	1556
υ_{11}	1559	1587	1552	1587			1552	1597
					1544	1542	1546	1543
υ_{20}								
						1376		1384
υ_4	1376	1342	1371	------			1369	1348
					1369	1367		1368

[a] From ref. [17]; [b] From ref. [19]; [c] From ref. [25].

energy excited state is forbidden in the cofacial type diporphyrins. For the Mg-H_2 heterodimer, a Q band peak centered at 581 nm allows us to take advantage of the maximum output of our picosecond yellow dye laser, which peaks around this wavelength.

Figure 2.7 shows ground state resonance Raman spectra of MgOEP, free base octaethylporphyrin (H_2OEP), Mg-Mg and Mg-H_2 with 413.1 nm excitation. From the vibrational frequencies and the depolarization ratios observed, we are able to assign vibrational modes of Mg-H_2 diporphyrin compounds (Table 2.4). The Soret excited resonance Raman spectrum of H_2OEP closely resembles those of the metalloporphyrins, despite the fact that H_2OEP has D_{2h} symmetry rather than the D_{4h} symmetry of the metalloporphyrins [33, 38, 51]. As the core sizes of Mg porphyrin and free base porphyrin are very similar, it is not surprising that MgOEP and H_2OEP have similar Raman band assignments . The vibrational modes of OEP monomers correlate well with those of the Mg-H_2 heterodimer, indicating that the two porphyrin macrocycles of the dimer have minimal interaction in the ground state. Similar behavior has been observed in other neutral dimeric metalloporphyrins [34]. One notable difference between the Raman spectra of the dimers and those of the monomers, however, is that the peak intensity of CH_2 twisting motions of the monomer species, which occur in the 1260 cm^{-1} region [33, 52, 53], decrease in the diporphyrin Raman spectra. Apparently, those torsional motions are constrained by the covalent linkages that attach the porphyrin rings of the dimer [Fig. 2.1] so that resonance Raman active conformations are minimized.

The positive detection of the charge separated state relies on directly monitoring the charge separated species. Most of the picosecond transient absorption measurements were carried out at wavelengths of 600 nm to 700 nm where are the region of characteristic charge separated state absorption. Previous studies have indicated that spectral characterization of porphyrin excited states is difficult at

wavelengths from 400 nm to 500 nm region due to overlapping absorption bands of the singlet, triplet and radical species. However, it is possible to identify these species in the ultraviolet region according to their life time [12].

The generation and decay of the charge separated state of Mg-H_2 have been previously studied by optical methods [3-6]. In brief, within 6 psec of photoexcitation one electron transfer from the Mg porphyrin (MgP) to the free base porphyrin (H_2P) occurs with high quantum yield [3]. The major fraction of the dimers in this charge separated state lives ~ 200 psec before charge recombination occurs; a small fraction of those species in the charge separated state (< 4% quantum yield) decays via a long-lived state with a life time of ~ 5 ns [3, 4]. The low quantum yield of fluorescence quenching of these compounds in CH_2Cl_2 solvent, in which the charge-transfer state and the lowest singlet state is about 150 to 200 meV apart, implies that charge transfer is the dominant deactivation pathway. This provides us with an ideal temporal situation within which to probe the charge transfer state without interference from other excited states (porphyrin singlet and triplet states) species, which have life times in the nsec to msec time scale in Mg and free base porphyrins [54]. The psec time-resolved resonance Raman spectra of Mg-H_2 obtained with 580 nm pump and 430 nm probe with pump subtracted are shown in Figure 2.8. New features appear near 1384 cm^{-1}, 1556 cm^{-1} and 1600 cm^{-1} with the 30 psec delay and are assigned to the Mg^+-H_2^- charge transfer state. At 500 psec, those features decay as charge recombination occurs. This latter observation confirms that the charge separated state is detected at early times. In order to assess these spectral changes in detail, the difference spectra are obtained and are shown in Figure 2.9. The spectrum in the probe only experiment is subtracted from those obtained with both pump and probe by using the 1423 cm^{-1} solvent peak as reference. At 30 psec time delay, peaks occur at 1348 cm^{-1}, 1384 cm^{-1}, 1543 cm^{-1}, 1556 cm^{-1} and 1597 cm^{-1} in the difference spectrum. The inverse peak at 1370 cm^{-1} is due to both lost ground state population and increasing stray light

background in the two beam experiment. At 500 psec time delay, although some lost population remains, the positive-going Raman peaks that were apparent at shorter time delays have diminished significantly. This result is consistent with the charge recombination rate obtained in the transient absorption experiments [3, 4]. The inverse peaks at 1370 cm^{-1} and in the 1580 cm^{-1} region in the 500 psec spectrum indicate that a fraction of molecules has not returned to the ground state at this time; moreover, the absence of positive-going features in the 500 psec spectrum suggests that the longer-lived metastable states (possibly the 5 nsec state detected by Netzel (see above)) do not have significant resonance Raman cross sections at λ_{ex} = 430 nm. We can eliminate irreversible photodamage as a source of the 500 psec lost ground state population as control optical experiments before and after the Raman measurements yielded identical optical spectra. Further supporting evidence comes from the resonance Raman spectra taken at 2.0 ns delay. These experiments were designed with long time accumulations at much extensive laser irradiance in order to test the possible photodamage of the sample. All of these spectra [Fig. 2.10] lack the charge separated state peaks and basically give the same features as the ground state spectrum.

Transient optical absorption spectra have shown that there is a broad feature in the charge separated state that extends from 610 nm to 700 nm. As monomers, the MgP^+ cation and the H_2P^- anion maximize at ~665 nm and ~635 nm, respectively [3-6]. The absorption band of the charge transfer state of the heterodimer thus shows a reasonable correspondence with the composite difference spectrum calculated from the oxidation of MgOEP and reduction of H_2OEP [3]. The optical results suggest that, in the heterodimer charge separated state, MgP^+ and H_2P^- retain monomer characteristics. Accordingly, the assignment (Table 2.5) of the vibrational modes of the Mg-porphyrin (MgP) cation of the Mg^+-H_2^- diporphyrin is made by analyzing patterns that have been established previously for the vibrational modes of MOEP cations (CuOEP, ZnOEP, MgOEP) [25-29]. The assignment of the 1597 cm^{-1} band

to the υ_{11} and υ_2 modes is made because, in the high frequency region, modes involving primarily C_bC_b stretching (υ_{11} and υ_2) increase in frequency as the result of removing one electron from the porphyrin a_{1u} orbital. In general, this assignment is close to what is predicted by metalloporphyrin $^2A_{1u}$ cation core size correlation [17,18]. Similar results have been reported for the singly-oxidized, sandwich-type, diporphyrin cation complex [35]. In $^2A_{1u}$ metalloporphyrin cation radicals, modes involving primarily C_aC_m stretching character decrease in frequency. However, the υ_{10} mode, which has C_aC_m character, is usually weak in the neutral species and in our experiments the υ_{10} mode in the MgP^+ cation of the heterodimer can not be identified. The υ_4 mode, the oxidation state marker in heme proteins, is the most strongly enhanced mode observed for neutral ground state metalloporphyrins when Soret excitation is used. This mode shifts down and loses intensity in the resonance Raman spectra of the $^2A_{1u}$ type π cation radical and is assigned to 1348 cm^{-1} in the MgP^+ cation.

The assignments of the vibrational modes of the free base anion (H_2P^-) in Mg^+-H_2^- are made by analogy to those of the OEP anions [33]. In the monomer, both υ_2 and υ_{11} modes down shift upon oxidation (Table 2.5). Accordingly, modes in the heterodimer charge transfer state that occur at 1556 cm^{-1} and 1543 cm^{-1} are assigned to those two vibrations, respectively. This relatively large shift pattern is consistent with earlier results for monomeric H_2OEP^- anions [33], which have been interpreted to indicate that excess electron density in the anion radical is localized at the porphyrin peripheral atoms rather than at those at the center. The υ_4 mode of the monomeric H_2OEP^- anion shifts only two wavenumbers relative to its parent neutral H_2OEP species. If this is the case for the Mg^+-H_2^-, the υ_4 mode of the H_2P^- anion overlaps the strong ground state υ_4 band and its exact frequency will be obscured by the large negative ground state contribution in the 1370 cm^{-1} region.

We now turn to the assignment of the Raman band at 1384 cm^{-1} in the charge separated state. In the D_{4h} symmetry of closed shell neutral porphyrins, a_{1g}, b_{1g} and b_{2g} vibrations are Jahn-Teller active, whereas modes of the a_{2g} symmetry are not. However, in the lower symmetry case, a_{2g} modes can be Jahn-Teller active as a result of removing an electron from the a_{1u} or a_{2u} orbitals to form the metalloporphyrin cation [42]. The 1384 cm^{-1} peak is, however, unlikely to arise from the MgP^+ cation of Mg^+-H_2^- as there are no strong resonance Raman active vibrations of the metalloporphyrin cation in this region. On the other hand, this vibration can be assigned to the υ_{20} mode of the H_2P^- because there is a significant enhancement of a depolarized mode in this region in the resonance Raman spectrum of the H_2OEP^- anion [33]. The Jahn-Teller effect is expected to be small in the free base porphyrin anions, as it is already in D_{2h} symmetry. A rationale for strong B-state resonance enhancement of non-totally symmetric modes has been provided in the earlier work on the H_2OEP anion [33]. The υ_{20} vibration belongs to the b_{1g} mode of the free base porphyrin. In D_{2h} symmetry, Herzberg-Teller coupling, which mixes nondegenerate porphyrin excited states, occurs through the b_{1g} modes. Thus the υ_{20} vibration can gain intensity via Herzberg-Teller coupling between anion low-lying excited states.

The data and analysis presented here allow us for the first time to get a preliminary picture of the vibrational properties of the charge separated state of the diporphyrin complex. We have observed the ground state and the charge separated state of the Mg-H_2 diporphyrin complex by using resonance Raman and time-resolved resonance Raman spectroscopy. The interpretation of the time-resolved spectra described in this paper is based on a comparison with the known spectra of metalloporphyrins, free base porphyrin, and their cation and anion derivatives and indicate that we can decompose the charge transfer state spectrum into contributions from the anion and cation halves of the diporphyrin complex.

2.5 Discussion

In the previous section we discussed the use of two color picosecond Raman pump and probe techniques to dynamically measure the relative population of electron density on Mg-H_2 diporphyrin complex. The similarity of the vibrational patterns between the diporphyrin complex and the porphyrin cation and anion radicals leads us to think that the principal force in altering the force constants in the Mg^+-H_2^- charge separated state is the electron density distribution between two porphyrin rings, and that the possible orbital occupancies in Mg^+-H_2^- are similar to these of Mg porphyrin cation and free base porphyrin anion. It would be interested to explore this idea further by investigating in detail the orbital distributions and electronic states of porphyrin cation, anion and diporphyrin excited states.

Gouterman treated the vibronic coupling and optical spectra of porphyrin π macrocycle by using a cyclic polyene model of linear combinations of one electron promotions between the two accidentally degenerate highest occupied orbitals, a_{1u} and a_{2u}, and two lowest unoccupied orbitals, e_g under D_{4h} symmetry [42]. The Q bands in the visible region can be constructed from a subtractive combination of two promotions, and the Soret bands originate from an additive combination of two promotions. This interpretation is known as the four-orbital model. Since Gouterman's work, the general features of the a_{1u}, a_{2u}, and e_g orbitals, as well as the general predictions of the four-orbital model, have been reproduced by many different MO calculations on a variety of porphyrin derivatives.

The semi-empirical INDO/s computational methods employed here have been described previously [55-57] and have been applied in studies of the electronic spectra of several heme porphyrin and chlorin systems [58]. Several modifications have been done, however, to the original computational package in order to apply it to large molecular systems such as the diporphyrin complexes discussed here. A more detailed description of modification of the subroutines to increase the maximum number of

atoms allowed and to modify the CI matrix in this package, along with an input example, are available upon request. Briefly, the molecular coordinates for diporphyrin complex were adapted from X-ray crystallographic data [17]. SCF calculations were performed to obtain the ground state MO descriptions. Subsequently, electronic wave function for 15 ground states orbitals (orbital # 100 to 114) and 15 lowest excited states orbitals (orbital # 115 to 130) of the complex were calculated by performing the singlet excited CI procedure [56, 57]. A total of the lowest 35 excited singlet sates were calculated.

2.5.1 Ground State

The ground states of neutral diporphyrin complexes at different ring-ring distances, were calculated by SCF method. The frontier orbitals (HOMO and LUMO) are given in the Figure 11 and their orbital coefficients are listed in Table 2.6. Similar to their monomer porphyrin counterparts, the highest four HOMOs have a_{1u} properties (H_2P is treated in D_{4h} symmetry) characterized by large unpaired spin densities at α carbons adjacent to the nitrogen atoms or a_{2u} properties with large spin densities at *meso*-carbons and on the nitrogen atoms. The lowest four LUMOs are of e_g symmetry with π electron densities at β and *meso* positions. The calculations show that for ring-ring distance less than 3.5 Å, i.e., in Van der Waals contact, there are strong orbital mixing between the two porphyrin rings. The coefficients of the orbitals are evenly distributed among two rings. This could be the case of exciton states as the result of strong ring-ring interaction. At ring-ring distances from 3.5 Å to 4.5 Å, there is a transition period, orbital mixing decreases as the ring-ring distance increases. The HOMOs have more mixing between MgP and H_2P than the LUMOs. For ring-ring distances larger than 4.5 Å, however, the two porphyrins basically retain their monomer properties. The orbital coefficients are very similar to those of the monomer porphyrins. More than 95% of orbital density is localized in MgP or H_2P rings. The

Table 2.6. Ground State Orbital Coefficients of HOMO and LUMO of the Neutral Diporphyrin Complexes

Orbital #/symmetry	C_α		C_β		C_{meso}		N	
	MgP	H_2P	MgP	H_2P	MgP	H_2P	MgP	H_2P
$111/a_{2u}$	0.06	0.050	0.100	0.094	0.265	0.262	0.148	0.180
$112/a_{1u}$	0.20	0.234	0.110	0.126	0.005	0.004	0.004	0.004
$113/a_{1u}$	0.05	0.05	0.09	0.079	0.270	0.255	0.155	0.174
$114/a_{1u}$	0.235	0.198	0.125	0.103	0.005	.030	0.005	0.003
$115/e_g$	0.109	0.191	0.100	0.143	0.155	0.170	0.078	0.088
$116/e_g$	0.123	0.125	0.110	0.120	0.160	0.225	0.07	0.100
$117/e_g$	0.169	0.138	0.139	0.118	0.210	0.155	0.09	0.650
$118/e_g$	0.155	0.106	0.130	0.091	0.200	0.185	0.09	0.073

Table 2.7a. Orbital Coefficients of HOMO of the Cation Diporphyrin Complexes

Orbital #/symmetry	C_α		C_β		C_{meso}		N	
	MgP	H_2P	MgP	H_2P	MgP	H_2P	MgP	H_2P
111/a_{1u}	0.242		0.114		0.098		0.130	
112/a_{2u}		0.182		0.156		0.225		0.239
113/a_{2u}		0.277		0.123		0.114		0.165
114/a_{1u}	0.119		0.116		0.318		0.235	

Table 2.7b. Net Charge Densities of the Cation Diporphyrin Complexes

Ring-Ring Distance (A^o)	3.3	3.5	3.8	4.0	4.5
MgP:					
Mg + H	1.970	1.973	1.930	1.829	1.834
C_α	1.310	1.315	1.188	1.093	1.085
C_β	-0.488	-0.484	-0.498	-0.504	-0.503
C_{meso}	-0.282	-0.275	-0.201	-0.101	-0.100
N	-1.625	-1.603	-1.456	-1.326	-1.318
Total	0.885	0.926	0.963	0.991	-0.998
H_2P:	1.580	1.570	1.620	1.722	1.720
H					
C_α	0.940	0.939	0.940	0.948	0.936
C_β	-0.698	-0.704	-0.705	-0.705	-0.714
C_{meso}	-0.282	-0.289	-0.336	-0.320	-0.312
N	-1.465	-1.473	-1.485	-1.638	-1.628
Total	0.075	0.043	0.034	0.007	0.002

Table 2.8a. Orbital Coefficients of HOMO of the Anion Diporphyrin Complexes

Orbital #/symmetry	C_α		C_β		C_{meso}		N	
	MgP	H_2P	MgP	H_2P	MgP	H_2P	MgP	H_2P
115/e_g		0.231		0.189		0.190		0.102
116/e_g	0.203		0.191		0.235		0.143	
117/e_g	0.195		0.179		0.260		0.180	
118/e_g		0.141		0.157		0.280		0.240

Table 2.8b. Net Charge Densities of the Anion Diporphyrin Complexes

Ring-Ring Distance (A^o)	3.3	3.5	3.8	4.0	4.5
MgP:					
Mg + H	1.405	1.424	1.498	1.552	1.574
C_α	1.00	1.012	1.006	1.009	1.003
C_β	-0.666	-0.653	-0.688	-0.750	-0.743
C_{meso}	-0.340	-0.321	-0.312	-0.303	-0.302
N	-1.535	-1.529	-1.533	-1.532	-1.539
Total	-0.136	-0.067	-0.029	-0.024	-0.007
H_2P:					
H	1.222	1.217	1.210	1.197	1.197
C_α	0.776	0.759	0.765	0.746	0.778
C_β	-0.965	-0.980	-0.976	-0.952	-0.936
C_{meso}	-0.382	-0.395	-0.405	-0.413	-0.443
N	-1.476	-1.489	-1.532	-1.552	-1.588
Total	-0.825	-0.888	-0.938	-0.974	-0.992

order of HOMOs in increasing energy is $a_{2u}(H_2P) < a_{1u}(H_2P) < a_{2u}(MgP) < a_{1u}(MgP)$ with a small gap between them (< 0.01 a.u.). However, at larger ring-ring distance, the $a_{2u}(MgP)$ orbital drops bellow H_2P's a_{1u} and a_{1u} orbitals. The lower D_{2h} symmetry of the H_2P, which causes the splitting of the near degenerate a_{1u} and a_{2u} orbitals, and the exciton interaction at short porphyrin ring-ring distance may account for the above change in orbital orders. On the other hand, the change in ring-ring distance has little effect on LUMOs. The order of LUMOs in increasing energy is 2 $e_g(H_2P) < 2\ e_g(MgP)$.

2.5.2 The Cation and Anion Radicals

Mg porphine cation radical has been studied experimentally with EPR and ENDOR [14, 59] and theoretically with the ZINDO semi-empirical method [57]. Our results on this monomer radical were very similar to those reported, i.e., an $^2A_{1u}$ configuration. The orbital distribution and electron occupancy of the diporphyrin cation and anion radical were calculated by UHF procedures. The results from ROHF methods were similar to those from UHF. The geometries of the diporphyrins used in calculations were the same as those for their parent diporphyrin compound, but an electron was added or subtracted from the complex. The results are given in Table 2.7 and Table 2.8. It is expected that at large ring-ring distance (> 4.0) the electronic structure of diporphyrin radicals is similar to their parental monomer porphyrin radicals and the charge is localized. However, it is clear that, even if at very close ring-ring distance, 3.5 Å, the cation radical has an $^2A_{1u}$ configuration with more than 93% orbital coefficients concentrated on the MgP side. The electron density analysis also indicates that 0.93 (at 3.5 Å) and 0.99 (at 4.0 Å) of the charge is localized at MgP macrocycle. ENDOR studies of the special pair in bacterial reaction centers showed that the oxidized dimers behave like supermolecules, however, the unpaired spin density is unevenly distributed over both rings [60]. Considering that the

electrochemical potential difference between and MgP and H_2P is much larger than that of the two BChl molecules in the special pair, it is not surprising that charge is localized at the electrostatically favorable MgP ring. The calculations of the orbital distribution and the electron occupancy also indicates that the diporphyrin anion radical has an ^2E_g configuration with 90% of orbital coefficients is on H_2P ring. The electron density analysis shows that 0.89 of the unpaired electron is localized at the H_2P macrocycle at a ring-ring distance equal to 3.5 Å.

In contrast to these radicals, at the Van der Waals distance, their parent neutral diporphyrin complexes show strong ring-ring orbital mixing. Nevertheless, cation and anion diporphyrin radicals are in a stable configuration which is similar to the monomer porphyrin cation or anion. No mixing occurs in these diporphyrin cation and anion radicals. This is a very interesting result as it implies that: 1) at least for the ground state, the diporphyrin cation and anion radicals have retained their monomer porphyrin properties; 2) without significantly alter the porphyrin macrocycle structure, diporphyrin complex can have strong exciton coupling before the charge transfer occurs. The same diporphyrin structure can also localize cation or anion radical at one of porphyrin rings that is electrochemical favorable for stabilizing the charge after the initial charge separation. The implications of these results will be discussed in next section.

2.5.3 The CI Results

The CI wavefunctions from the combination of exciting an electron from fifteen highest occupied orbitals into sixteen lowest unoccupied orbitals were obtained by using ZINDO/s. The low-lying excited states up to the Soret bands, their transition energies and oscillator strengths at ring-ring distance equal to 3.5 Å, 4.0 Å and 4.5 Å are listed in Table 2.9, 2.10 and 2.11. For ring-ring distances larger than 4.5 Å, the excited states can be characterized simply as either monomeric $\pi \rightarrow \pi^*$ states or as

linear combinations of the monomeric states. The first group of excited states with MgP to H_2P charge transfer characters are calculated around the 18000 to 20000 cm^{-1} region, higher than the Q bands of porphyrin macrocycles which is consistent with previous *ab-inito* calculation results on similar model compounds [61]. For ring-ring distances less than 3.5 Å, severe mixing of intermacrocyclic wavefunctions occurs. All the transitions are dimeric in character and no clear charge transfer bands can be detected. Furthermore, at such distances, the geometries of the two porphyrins are probably strongly distorted [15]. The most interesting region is the ring-ring distance between these two extremes, from 3.5 Å to 4.5 Å. Calculation results indicate this is a mixing region such that the localized, monomer-like $\pi \rightarrow \pi^*$ excited states, the delocalized dimeric exciton states and the charge transfer states are observed. Two low-lying excited states whose major components are MgP to H_2P charge transfer are detected below the diporphyrin Q bands. These results are consistent with the experimental picosecond transient absorption data on the same diporphyrin complexes, which show that two electron transfer bands lay below the porphyrin Q bands [3-6]. The four locally excited $\pi \rightarrow \pi^*$ states, which are essentially identical to the two lowest $\pi \rightarrow \pi^*$ transitions of monomer porphyrin, are assigned to the Q bands for this diporphyrin complexes. Some high-lying states and Soret bands are also assigned according to their transition symmetry and oscillator strengths. More interestingly, a group of mixing excited $\pi \rightarrow \pi^*$ states, i.e. simultaneous MgP to H_2P transition and H_2P to MgP transition which is similar to exciton coupling, are detected between Q bands and Soret bands. Those bands disappear at ring-ring distances large than 4.5 Å. The fact that the calculation results from this intermediate region are mostly consistent with the experimental data implies that exciton states may play an active role in the electron transfer process of those diporphyrins. From the diporphyrin cation and anion results in the previous section, we find that without significantly altering the porphyrin macrocycle structure, the same diporphyrin structure can have strong exciton coupling

Table 2.9. Electronic Transitions and Assignments of the Diporphyrin Complexes at 3.5A^{0} Ring-Ring Distance

Transition Energy (cm^{-1})	Transition Assigments (Major components)	Oscillator Strength
12105	CT (Mg -> H_2P)	0.0004
12256	CT (Mg -> H_2P)	0.0001
15440	Q (MgP: π–π^*)	0.0346
16259	Q (MgP: π–π^*); Q (H_2P: π–π^*)	0.0895
18162	Q (H_2P: π–π^*)	0.0144
18340	CT (MgP-> H_2P); Q (MgP: π–π^*)	0.0013
20041	CT (H_2P-> MgP); Q (H_2P: π–π^*)	0.0006
20422	Q: (H_2P: π–π^*)	0.0034
23429	π–π^*(MgP)	0.0334
24159	CT (H_2P-> MgP); π–π^*(MgP)	0.0494
24579	π–π^* (H_2P-> MgP + Mg -> H_2P)	0.0277
24795	π–π^* (H_2P-> MgP + Mg -> H_2P)	0.0046
26079	π–π^* (H_2P-> MgP + Mg -> H_2P)	0.0008
27121	π–π^* (H_2P-> MgP + Mg -> H_2P)	0.0010
27605	π–π^*; CT (MgP-> H_2P)	0.2540
29653	CT (H_2P-> MgP); π–π^*(MgP)	0.0121
29745	π–π^*	0.0174
29931	π–π^* (MgP)	0.0820
31011	π–π^*	0.0004
31805	π–π^*	0.1442

Table 2.9. Continue

32362	π–π^*	0.5555
32525	Soret π–π^*	1.2502

Table 2.10. Electronic Transitions and Assignments of the Diporphyrin Complexes at 4.0 A^{o} Ring-Ring Distance

Transition Energy (cm^{-1})	Transition Assigments (Major components)	Oscillator Strength
14288	CT (MgP -> H_2P); Q (MgP: π–π^*)	0.0054
15471	CT (MgP -> H_2P)	0.0028
16046	Q (π–π^*); CT (MgP -> H_2P)	0.0362
16604	Q (H_2P: π–π^*)	0.1032
19726	Q (H_2P: π–π^*)	0.0002
20961	CT (MgP -> H_2P);: π–π^* (MgP)	0.0060
21496	CT (H_2P-> MgP)	0.0001
21660	CT (H_2P -> Mg); π–π^* (H_2P)	0.0007
23772	π–π^* (H_2P)	0.0125
24208	π–π^* (H_2P)	0.0007
24654	CT (H_2P -> Mg)	0.0053
25370	π–π^* (H_2P-> MgP + Mg -> H_2P)	0.0286
26386	π–π^* (H_2P-> MgP + Mg -> H_2P)	0.0858
27384	π–π^* (H_2P-> MgP + Mg -> H_2P)	0.0029
28184	π–π^*	0.0013
28993	π–π^*	0.0387
29713	Soret π–π^*	0.7078
30195	π–π^*	0.1195
32542	Soret π–π^*	3.3810
33108	π–π^*	0.6688

Table 2.11. Electronic Transitions and Assignments of the Diporphyrin Complexes at 4.5A° Ring-Ring Distance

Transition Energy (cm^{-1})	Transition Assigments (Major components)	Oscillator Strength
14350	Q (H_2P: π–π^*)	0.0094
15932	Q (MgP: π–π^*)	0.0162
16220	Q (MgP: π–π^*)	0.0371
16590	Q (H_2P: π–π^*)	0.0944
20664	CT (Mg -> H_2P)	0.0000
20961	CT (MgP-> H_2P); π–π^*(MgP)	0.0009
22195	CT (H_2P-> MgP)	0.0000
22513	CT (H_2P -> Mg); π–π^*(H_2P)	0.0001
25043	π–π^*(H_2P)	0.0469
25606	π–π^* (H_2P); CT (H_2P-> MgP)	0.0002
25727	π–π^* (H_2P-> MgP + Mg -> H_2P)	0.0003
26070	π–π^* (H_2P-> MgP + Mg -> H_2P)	0.0612
26354	π–π^* (H_2P-> MgP + Mg -> H_2P)	0.0168
27177	π–π^* (MgP); CT (MgP-> H_2P)	0.0004
28271	π–π^*	0.0026
29337	π–π^*	0.2760
29674	Soret π–π^*	0.7231
30057	π–π^*	0.1686
32133	Soret π–π^*	4.1876
33230	π–π^*	0.1821

before the charge transfer occurs and delocalize the cation or anion radical at one of the porphyrin rings. Therefore, exciton states may couple into the forward electron separation. Furthermore, the experimental results reveal that Mg-H_2 diporphyrins with long length, flexible side-chain linkages seen to prefer a closer conformation than its side chain length [3-4] and Mg-H_2 diporphyrins given a short ring-ring distance will tend to separated from each other by taking a "slipped" structure [17]. The consistency of our calculation results with the experiments suggest that this is an important intermediate region key to the electron transfer reactions that occur in these diporphyrin complexes. Electron transfer reactions are less efficient as the results of less interaction at large ring-ring distance (>4.5 A^o) or orbital contamination at short ring-ring distance (< 3.5 A^o).

These structures in the intermediate ring-ring distance region may also have another important function in the CT reactions, by minimizing the reorganization energy. It has been established both in experiments and in theories that porphyrin excited S_1 state is somewhat closer to the ground state in conformation than is the excited T_1 state, which experiences various distortions that arise from Jahn-Teller effects [42]. During the course of inter-system crossing from excited S_1 to the T_1 states, the change of the porphyrin conformation must go through a period that is favorable to the occur of the electron transfer reaction. Those structures may be more similar to the S_1 state structures or to the triplet state structures. Time-resolved Raman spectroscopy is the best method to detect the above structure changes. According to the Fermi Golden Rule of electron transfer reaction, the reaction rate is a products of an electronic matrix element squared, $|V|^2$, and a vibrational term which involves a thermally weighted sum of Franck-Condon factors, FC: $k_{et}=(4\pi^2/h)|V|^2 \cdot FC$. The matrix element V contains the dependence of the rate on the orientation of the electron donor and acceptor and their separation distance. The Franck-Condon factors contain the dependence on the density of states and total nuclear reorganization energy. For

electron transfer reactions in liquid medium, the Franck-Condon factors include contributions from both solvent motion, which are sufficiently low in frequency that they can be treated classically at most temperatures, and internal vibrations of the electron donor and acceptor, which usually must be handled quantum mechanically [62-64]. Therefore, in order to account properly for the quantum mechanical nature of the high frequency molecular vibrations, the frequencies and reorganization energies of these individual internal modes must be known [65]. Since such information is not usually available, the rate of electron transfer reaction are usually described by using models that employ a single "average" quantized vibrational mode with a frequency considered appropriate for the systems of interest [66-68]. Often a value close to 1500 cm^{-1} is chosen for this averaged frequency, as this is close to the frequencies of skeletal stretching vibrations of aromatic systems. Clearly the assumption of a single high frequency mode is at best a rough approximation. However, from our experimental data in the high frequency region, the modes which are most active, i.e. with large Raman intensity or shifts in the electron-transfer process, are those modes which relate to the porphyrin skeletal motions in the 1300 cm^{-1} to 1500 cm^{-1} range, such as ν_2 and ν_{20} of the anion and ν_2 and ν_{11} of the cation.

Under the sum of state expression of resonance Raman effect, the Raman tensor is the sum of a Franck-Condon term and a Herzeberg-Teller term.

$$\alpha_{m,n} = \frac{1}{h}|M(R_o)|^2 \sum \frac{< m|e >< e|n >}{\varpi_{me} - \varpi_L - i\Gamma_e} + \frac{1}{h}|M(R_o)|*|M!(R_o)|\sum \frac{< m|R|e >< e|n > + < m|e >< e|R|n >}{\varpi_{me} - \varpi_L - i\Gamma_e} + \ldots \tag{2.8}$$

In the Franck-Condon situation, excited state potential has a quite different shape and internuclear position from the ground state. In terms of the electron transfer, this will

require a large reorganization energy. This is not consist with the experimental data on this diporphyrin complexes since the charge separation is efficient. In order to achieve the maximum electron transfer efficiency, the reorganization energy should be small. Our calculation results indicate that the porphyrin dimer may serve this propose well under certain structures. Its structures are favorable for exciton coupling, which allows the charge delocalizes between the two porphyrin rings, which may serve as a precursor to the subsequent electron transfer reaction. After the electron transfer reaction the same structure with minimal alteration can also stabilize the changes in the charge separated state. In these systems, the excited state potential surface is nearly the same as that of the ground state, thus the vibrational wavefunctions are orthogonal. The Franck-Condon term in the Raman tensor expression only gives Rayleigh scattering. Under this circumstance the matrix element of $\langle e|R|n\rangle$ does not require total symmetric. The Hezeberg-Teller term dominates the Raman scattering. This is a possible cause of activation of the nonsymmetric modes in the charge separated state, such as ν_{20} mode, although it is an open question as to whether they come from a conformation during the charge transfer process or they are belong the metastable structure of final electron-separated states. In other words, the conformation of those nonsymmetric modes may have two functions, first to activate the electron-transfer process; second to stabilize the charge-separated species.

This initial interpretation has interesting implications for the molecular dynamics that accompany charge transfer. Several factors may be envisioned that could produce substantial structure changes in the charge separated state. In the diporphyrin case, the two porphyrin rings are nearly in van der Waals contact [17]. Although this type of porphyrin ring-ring interaction has only small effects on the ground state vibrations [Fig. 3 and Table 1], its effect may be enhanced in the excited state and in the charge transfer state. For example, geometry changes have been observed for porphyrin dimers upon formation of the corresponding singly oxidized cation radicals [15, 16].

For the dimers we studied here, if the charge separated state involves an electron transfer from the a_{1u} orbital of the Mg porphyrin to the e_g orbital of the free base porphyrin, as our data indicate, then rotation in the x-y plane of the cationic ring relative to the anionic ring by ~ 45^o will produce maximum in-phase overlap of the orbitals. Although the covalent links will restrict this process, some rotation might be expected and this would produce shifts in π electron density and ring distortion, which would, in turn, cause vibrational mode shifts. Resonance Raman spectroscopy [35] on lanthanide porphyrin sandwich complexes and their cation radicals also shows that there are vibrational manifestations of porphyrin-porphyrin π–π interaction [see also 7, 13]. Moreover, resonance Raman spectroscopy of the ground state special pair of bacterial reaction center [70-73] has detected several low-frequency peaks that are proposed to arise from modes that are unique to the dimer by using several excitation wavelengths in the 800 - 910 nm range. Thus, nonsymmetric modes may also gain intensity from this kind of ring-ring interaction. However, from the analysis of our transient Raman data, we conclude that the effect of ring-ring interactions on the charge transfer state of the diporphyrin complexes of Fig 1, are minor in the high frequency region ($\Delta > 1200$ cm^{-1}), in comparison with the effects of oxidation and reduction of the two porphyrin rings. The changes in force constant in the charge separated state are basically dominated by the formation of cation/anion porphyrin radicals. Other factors are not large enough to change appreciably the overall character of the high frequency normal modes.

Our results indicate that, in the charge separated state of the Mg-H_2 diporphyrin complex, the MgP^+ cation half of the dimer is in its $^2A_{1u}$ electronic state. The H_2P^- anion half in the charge transfer state has vibrational characteristics that are typical of the free base octaethylporphyrin anion. Further resonance Raman studies on porphyrin excited states at short times are ongoing in our lab, and will give us a more detailed

model of the vibrational dynamics that occur upon photoexcitation and charge transfer transitions in porphyrin-based systems.

2.6 Acknowledgment

We thank Dr. T. Carter for technical help on the psec laser instrumentation. Support is acknowledged from grant GM 25480 (to G.T.B.) of the U.S. National Institute of Health.

References

1. W. W. Parson, in Chlorophylls, p 1153, H. Scheer eds., *CRC Press*, **1991**.

2. M. R. Wasielewski, *Chem. Rev.* **1992,** *92*, 435.

3. I. Fujita, J. Fajer, C. K. Chang, C. B. Wang, M. A. Bergkamp and T. L. Netzel, *J. Phys. Chem.* **1982,** *86*, 3754.

4. T. L. Netzel, M. A. Bergkamp and C. K. Chang, *J. Am. Chem. Soc.* **1982,***104*, 1952.

5. J. M. Zaleski, C. K. Chang, G. E. Leroi, R. I. Cukier and D. G. Nocera, *J. Am. Chem. Soc.* **1992,***114*, 3564.

6. J. M. Zaleski, C. K. Chang, G. E. Leroi, R. I. Cukier and D. G. Nocera, *Chem. Phys.* **1993,** *176*, 483.

7. O. Bilsel, J. Rodriguez and D. Holten, *J. Phys. Chem.* **1990,** *94*, 3508.

8. J. Rodriguez, C. Kirmaier, M. R. Johnson, R. A. Friesner, D. Holten and J. L. Sessler, *J. Am. Chem. Soc.* **1991,** *113*, 1652.

9. D. G. Johnson, M. P. Niemczyk, D. W. Minsek, G. P. Wiederrecht, W. A. Svec, G. L. Gaines, III and M. R. Wasielewski, *J. Am. Chem. Soc.* **1993,** *115*, 5701.

10. M. R. Wasielewski, G. L. Gaines, III, G. P. Wiederrecht, W. A. Svec and M. P. Niemczyk, *J. Am. Chem. Soc.* **1993,** *115*, 10442.

11. N. Mataga, H. Yao, T. Okada, Y. Kanda and A. Harriman, *Chem. Phys.* **1989,** *131*, 473.

12. A. M. Brun, A. Harriman, V. Heitz and J.-P. Sauvage, *J. Am. Chem. Soc.* **1991,** *113*, 8657.

13. O. Bilsel, J. Rodriguez, D. Holten, G. S. Girolami, S. N. Milam and K. S. Suslick, *J. Am. Chem. Soc.* **1990,** *112*, 4075.

14. H. Levanon, A. Regev, T. Galili, M. Hugerat, C. K. Chang and J. Fajer, *J. Phys. Chem.* **1993,** *97*, 13198.

15. W. R. Scheidt, B. Cheng, K. J. Haller, A. Mislankar, A. D. Rae, K. V. Reddy, H. Song, R. D. Orosz, C. A. Reed, F. Cukiernik and J.-C. Marchon, *J. Am. Chem. Soc.* **1993,** *115,* 1181.

16. H. Song, C. A. Reed, and W. R. Scheidt, *J. Am. Chem. Soc.* **1989,** *111,* 6867.

17. J. P. Fillers, K. G. Ravichandran, I. Abdalmuhdi, A. Tulinsky and C. K. Chang, *J. Am. Chem. Soc.* **1986,** *108,* 417.

18. J. Dalton, L. R. Milgrom, *J. Chem. Soc. Commun.* **1979,** 609.

19. J. L. Sessler, M. R. Johnson and T. Y. Lin, *Tetrahedron* **1989** *45,* 4767.

20. J. L. Sessler, M. R. Johnson S. E. Creager, J. C. Fettinger and J. A. Ibers, *J. Am. Chem. Soc.* **1990,** *112,* 9310.

21. A. Osuka, S. Morikawa, K. Maruyama, S. Hirayama and T. Minami, *J. Chem. Soc., Chem. Comm.* **1987,** 359.

22. Osuka, S. Nakajima, K. Maruyama, N. Mataga, and T. Asahi, *Chem. Lett.* **1991,** 1003.

23. A. Osuka, H. Yamada and K. Maruyama, *Chem. Lett.* **1990,** 1905A.

24. D. Gust *et al, J. Am. Chem. Soc.* **1993,** *115,* 5684.

25. W. A. Oertling, A. Salehi, Y. C. Chung, G. E. Leroi, C. K. Chang and G. T. Babcock, *J. Phys. Chem.* **1987,** *91,* 5887.

26. W. A. Oertling, A. Salehi, C. K. Chang and G. T. Babcock, *J. Phys. Chem.* **1989,** *93,* 1311.

27. W. A. Oertling, *Ph.D. Thesis,* **1987,** Michigan State University.

28. R. S. Czernuszewicz, K. A. Macor, X.-Y. Li, J. R. Kincaid and T. G. Spiro, *J. Am. Chem. Soc.* **1989,** *111,* 3860.

29. K. Prendergast and T. G. Spiro, *J. Phys. Chem.* **1991,** *95,* 9728.

30. J. Teraoka, S. Hashimoto, H. Sugimoto, M. Mori and T. Kitagawa, *J. Am. Chem. Soc.* **1987,** *109,* 180.

31. G. P. Gurinovich, I. F. Gurinovich, N. V. Ivashin, G. N. Sinyakov, A. M. Shulga, S. N. Terekhov, I. V. Filatov and K. Dzilinski, *J. Mol. Struct.* **1988,** *172,* 317.

32. R. A. Reed, R. Purrello, K. Prendergast and T. G. Spiro, *J. Phys. Chem.* **1991,** *95,* 9720.

33. J.-H. Perng and D. F. Bocian, *J. Phys. Chem.* **1992,** *96,* 4804.

34. D. Gosztola and M. R. Wasielewski, *J. Phys. Chem.* **1993,** *97,* 9599.

35. J.-H. Perng, J. K. Duchowski and D. F. Bocian, *J. Phys. Chem.* **1991,** *95* 1319.

36. V. A. Walters, J. C. de Paula, G. T. Babcock and G. E. Leroi, *J. Am. Chem. Soc.* **1989,** *111,* 8300.

37. R. Kumble, S. Hu, G. R. Loppnov, S. E. Vitols and T. G. Spiro, *J. Phys. Chem.* **1991,** *95,* 9720.

38. S. Sato, M. Asano-Someda and T. Kitagawa, *Chem. Phys. Let.* **1992,** *189,* 443.

39. S. E. J. Bell, A. H. R. Al-Obaidi, M. Hegarty, R. E. Hester and J. J. McGarvey, *J. Phys. Chem.* **1993,** *97,* 11599.

40. S. H. Courtney, T. M. Jediu, J. M. Friedman, R. G. Alden and M. R. Ondrias, *Chem. Phys. Lett.* **1989,** *164,* 39.

41. D. Kreszowski, G. Deinum and G. T. Babcock, *J. Am. Chem. Soc., submitted.*

42. M. Gouterman, *In The Porphyrins, Vol. 3, p 1, D. Dolphin eds,* Acad. Press, **1978.**

43. C. B. Wang and C. K. Chang, Synthesis **1979,** 548.

44. A. T. Tu, *Raman Spectroscopy in Biology: Priciple and Applications* Wiley, **1982.**

45. P. Das, *Laser and Optical Engineering, Springer-Verlag,* **1991.**

46. I. Crouch and D. James, *Spectrochemical Analysis, Englewood Cliffs,* **1988.**

47. M. Gouterman, D. Holten and E. Lieberman, *Chem. Phys.* **1977,** *25,* 139.

48. A. Osuka and K. Maruyama, *J. Am. Chem. Soc.* **1988,** *110,* 4454.

49. C. A. Hunter, J. K. M. Sanders and A. J. Stone, *Chem. Phys.* **1988,** *133,* 395.

50. S. Eriksson, B. Kallebring, S. Larsson, J. Martensson and O. Wennerstrom, *Chem. Phys.* **1990,** *146,* 165.

51. X. Li and M. Z. Zgierski, *J. Phys. Chem.* **1991,** *95,* 4268.

52. T. Kitagawa, M. Abe and H. Ogoshi, *J. Phys. Chem.* **1978,** *69,* 4516.

53. P. Thoai, J. P. Leicknam, M. Momenteau and B. Loock, *Spectro. Lett.* **1979,** *12,* 333.

54. J. Rodriguez, C. Kirmaier and D. Holten, *J. Am. Chem. Soc.* **1989,** *111,* 6500.

55. J. D. Head, M. C. Zerner and B. Weiner, *Chem. Phys. Lett.* **1986,** *131,* 359.

56. M. C. Zerner, J. Mckelvey and W. D. Edwards, *Theoret. Chim. Acta,* **1987,** *72,* 347.

57. W. E. Edwards and M. C. Zerner, *Can. J. Chem.* **1985,** *63,* 1763.

58. L. K. Hanson, in *Chlorophylls* p. 993, ed. H. Scheer, *CRC Press,* **1991.**

59. P. O. Sandusky, A. Salehi, C. K. Chang and G. T. Babcock, *J. Am. Chem. Soc.* **1989,** *111,* 6437.

60. N. Lubitz, F. Lendzian, M. Plato, K. Mobius and E. Trankle, in *Antannas and Reaction Centers of Photosynthetic Bacteria,* M. E. Michel-Beyerle ed., *Springer-Verlag,* **1985,** 164.

61. J. D. Perke and G. M. Maggiora, *J. Chem. Phys.* **1986,** *84,* 1640.

62. E. Buhks, M. Bixon, J. Jortner and G. Navon, *J. Phys. Chem.* **1981,** *85,* 3759.

63. P. Siders and R. A. Marcus, *J. Am. Chem. Soc.* **1981,** *103,* 741.

64. P. Siders and R. A. Marcus, *J. Am. Chem. Soc.* **1981,** *103,* 748.

65. I. Webman, N. R. Kestner *J. Chem. Phys.* **1982,** *77,* 2387.

66. J. Miller, J. V. Beitz and R. K. Huddleston, *J. Am. Chem. Soc.* **1984,** *106,* 5057.

67. N. Liang, J. Miller and G. L. Closs, *J. Am. Chem. Soc.* **1990,** *112,* 5353.

68. S. Franzen, R. F. Goldstein and S. G. Boxer, *J. Phys. Chem.* **1990,** *94,* 5135.

69. R. J. Donohoe, R.B. Dyer, B. I. Swanson, C. A. Violette, H. A. Frank and D. Bocian, *J. Am. Chem. Soc.* **1990,** *112*, 6716.

70. V. Palaniappan, M. A. Aldema, H. A. Frank and D. F. Bocian, *Biochemisrty* **1992,** *31,*11058.

71. A. P. Shreve, N. J. Cherepy, S. Franzen, S. G. Boxer and R. A. Mathies, *Proc. Natl. Acad. Sci, USA* **1991,** *88*, 11207.

72. T. A. Mattioli, A. Hoffmann, B. Robert, B. Schrader and M. Lutz, *Biochemistry* **1991,** *30*, 4648.

CHAPTER THREE

THE VIBRATIONAL CHARACTERIZATION OF THE SYNTHESIZED μ-OXO BRIDGED DIPORPHYRIN COMPLEXES AND IRON PORPHYRIN/COPPER CLUSTERS

Summary

Resonance Raman spectroscopy has been used to characterize μ-oxo vibrations in synthetic iron diporphyrin, diporphycene, iron porphyrin/Cu and iron porphyrin/Fe complexes. The μ-oxo symmetric vibrations were detected at 406 cm^{-1} and 452 cm^{-1} for the iron diporphyrin and diporphycene, respectively. The aymmetric vibrations were observed at 818 cm^{-1} and 824 cm^{-1} for iron porphyrin/Cu cluster and iron porphyrin/iron clusetr. Further evidence supporting these bridge vibrations comes from mode shifts in the protonated samples. The linear correlation of μ-oxo bridge vibrations and the M-O-M angle suggests that the M-O-M angle is a good indication of the bridge strength in these compounds.

3.1 Introduction

The μ-oxo dimer is a structure that has been proposed to exist in the active-site of several metalloenzymes. It has thus been the subject of much spectroscopic study [1-7]. Resonance Raman and IR spectroscopies have proven to be important methods for vibrational structural determinations. These techniques are particularly suitable for the characterization of bridge vibrations and have been used to probe the μ-oxo type bridged structure in the reaction mechanisms of several important enzymes and model systems, such as the possible detoxification pathway of the malaria pigment [8, 9], the respiratory hemerythrin of many invertebrates [10, 11], and the reduction of dioxygen into water in the catalytic cycle of cytochrome c oxidase [12, 13]. These techniques were also applied to the potentially physiologically important μ-oxo diporphyrins [14-16]. Recently, several porphyrin-based Fe-O-Fe and Cu-O-Fe complexes have been synthesized with [17] and without [5-7] the supporting covalent linkages between the di-metal centers. They have also been characterized by X-ray crystallography. These molecules, aimed to model the structure of the copper-heme a_3 complexes of the cytochrome c oxidase enzyme, are of importance to characterize with Raman spectroscopy in order to make contact with the *in vivo* studies underway in several labs [18-24]. The comparison of the vibrational modes of the model compounds with the *in vivo* system may clarify several important issues of the reaction mechanism in the enzyme system. These include mode assignments of the intermediates, the local environments and coordination numbers of the Cu_B site, and the reaction mechanism and kinetic scheme. Of particular interest to this work, we report resonance Raman studies of a series of Fe-O-Fe diporphyrin compounds and Fe-O-Cu complexes [17]. These compounds have been characterized by X-ray crystallography recently, and have shown well-defined distances between the two metal centers, as they are constrained by an aromatic linkage, in addition to the μ-oxo bridge (Figure 3.1a, b and c).

3.2 Methods

The synthesis of diiron and iron-copper complexes and the incorporation of the μ-oxo bridge were performed by Chang and co-workers and will be published elsewhere [17]. methylene chloride (for spectrophotometry, J. T. Baker) was distilled from $CaCl_2$ and used as the solvent in the spectroscopic studies. Absorption spectra were recorded on a Perkin-Elmer λ-5 spectrophotometer. The cw resonance Raman spectra were obtained by using the 413.1 nm laser line of a Coherent K^+ laser. Laser power was about 15 mW at the sample. The backscattering geometry was used in Raman measurements. Raman scattering was dispersed into a Spex 1877 triplemate monochromator and recorded by a CCD detector (Spex Spectrum One).

3.3 Results and Discussion

Compound I, shown in Figure 3.1a, is a μ-oxo iron porphyrin dimers whose structure has been determined by X-ray crystallography [17]. Two M-O-M vibrational stretching motions have been detected in several μ-oxo compounds [10,11, 13-16]. The symmetric stretching mode appears at about 350 ~ 550 cm^{-1} and an asymmetric stretching mode is at 700 ~ 900 cm^{-1}. Figure 3.2 shows the Raman spectra of this diporphyrin compound. Only the symmetric mode is predicted to be Raman active due to the exclusion rule of total symmetric groups [18]. However, since the aromatic side chain and the two closely packed porphyrins destroy the perfect linear Fe-O-Fe symmetry, the asymmetric mode may also be Raman active. Recently, X-ray crystallographic experiments on μ-oxo iron diporphyrin compounds have indicated this oxo bridge can be protonated and will, furthermore, break into hydroxide species [4, 19]. The 406 cm^{-1} and 822 cm^{-1} peaks in the μ-oxo species in Figure 3.1a can be tentatively assigned to the symmetric and asymmetric μ-oxo vibrations, respectively, as the 406 cm^{-1} mode down-shifted to the 387 cm^{-1} and the 822 cm^{-1} mode decreased

greatly in intensity when 1 μm of acetic acid was added. Positive identification of the origin of these modes will require with ^{18}O labeled samples. However, the fact that these modes are missing in spectra of the monomeric porphyrin starting material lends support to our assignment.

Figure 3.3 and Figure 3.4 give the resonance Raman spectra of another iron diporphyrin (DPX) and an iron diporphycene μ-oxo complexes [Figure 3.1b and 3.1 c]. pH sensitive modes have been found at 387 cm^{-1} for the DPX and 452 cm^{-1} for diporpycene and are assigned as the Fe-O-Fe symmetric stretching vibration.

Further evidence supporting the assignments in Figures 3.2 to 3.4 is that the frequency of the μ-oxo symmetric vibrations can be correlated empirically to the Fe-O-Fe angle, determined by X-ray crystallographic data [9]. A plot of the Fe-O-Fe angles vs. the symmetric and asymmetric μ-oxo stretching vibrations is given in Figures 3.5 and 3.6, respectively. In order to overlap with the sp hybrid orbitals of the oxygen, the ideal angle for Fe-O-Fe is 180^0. Actually, this is the case for most iron porphyrin μ-oxo dimers [20-24]. However, if the two porphyrin rings are constrained by other covalent linkages [25] or the μ-oxo bridge is protonated [19], this angle will become substantially smaller. In the iron diporphyrin compound studied here, the Fe-O-Fe angle is 164.7^0 and the distance between the two iron centers is $3.51A^0$. The two porphyrin rings are overlapped nearly perfectly (Figure 1a) and D_{4h} symmetry, without considering side chain linkage, is retained in the dimer. This conformation differs from the "slipped" equilibrium position of similar diporphyrin complexes [26]. These considerations suggest that there is a strong interaction in the diporphyrin system. Surprisingly, however, the 406 cm^{-1} μ-oxo vibration fits well in the angle-vibration

Figure 3.1a Top and side views of the X-ray ctrystallographic strucure for the "pacman" iron diporphyrin. The Fe-O-Fe angle is 165.7^{o} and the Fe-O bond length is 1.759 A^{o}.

Figure 3.1b The X-ray ctrystallographic strucure for the DPX iron diporphyrin.

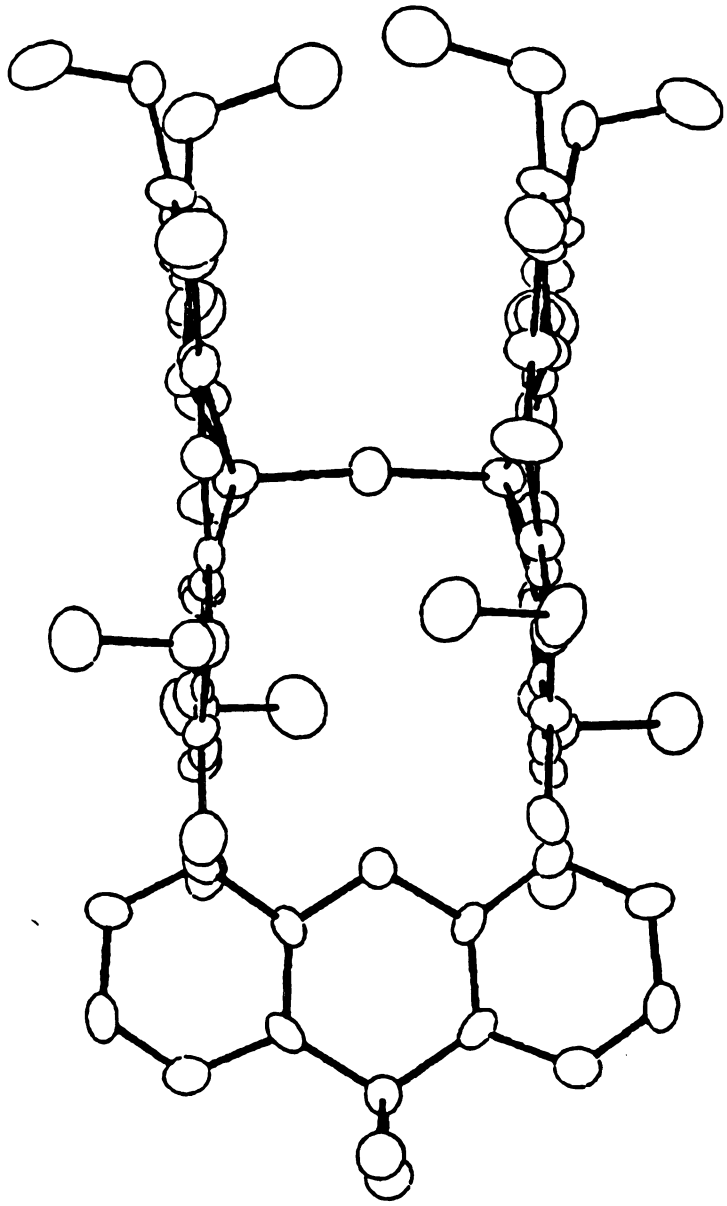

Figure 3.1c Top and side views of the X-ray ctrystallographic strucure for the iron diporphycene. The Fe-O-Fe angle is 145^{o} and the Fe-O bond length is 1.77 A^{o}.

Figure 3.1d The strucure for the iron porphryin-copper/iron ligands clusters.

Figure 3.2 The resonance Raman spectra of iron diporphyrin ("Pacman"). The excitation is 413.1 nm and the power is 15 mW. The top spectrum is taken from the same sample but with 1 μm acetic acid was added.

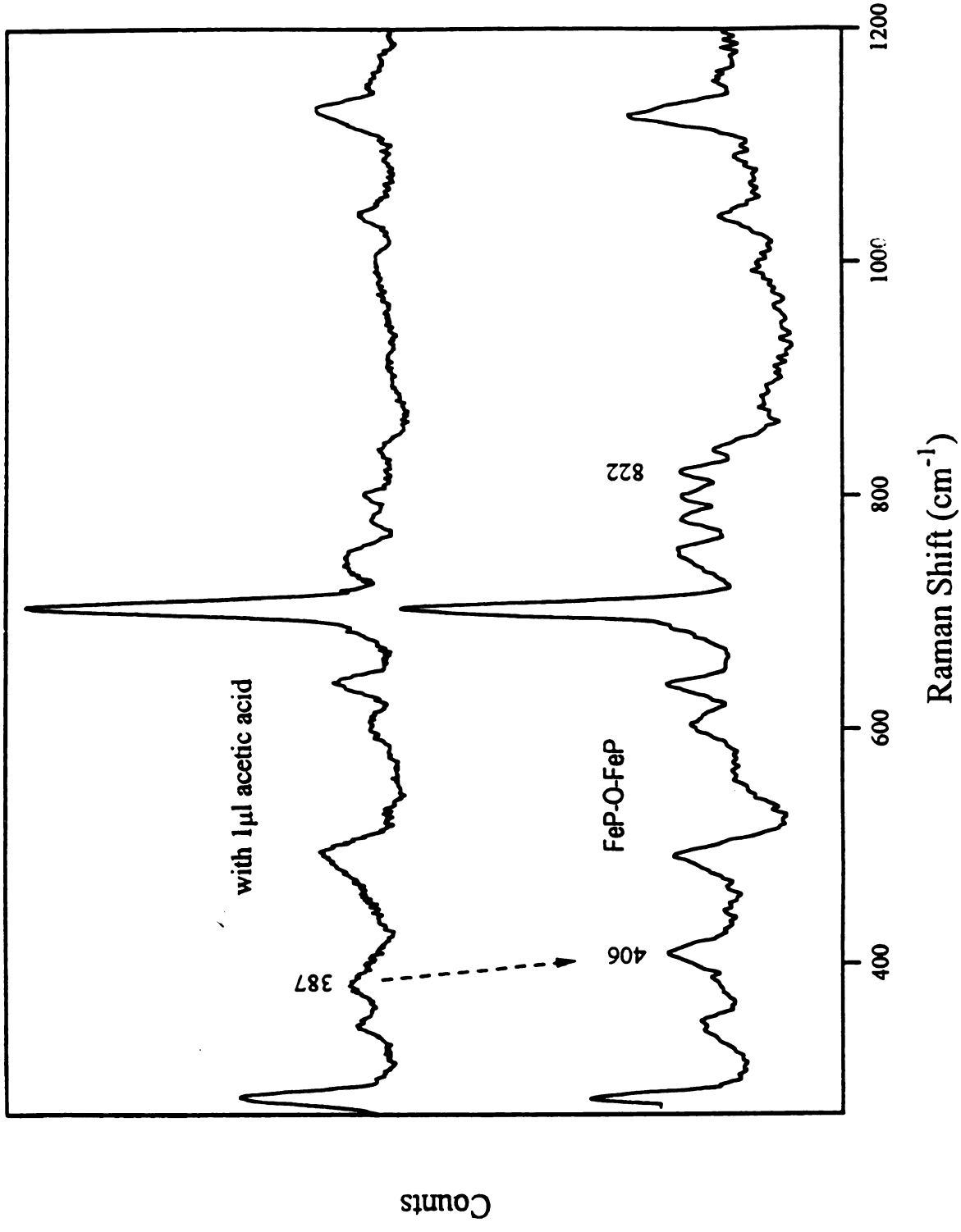
with 1µl acetic acid
387
406
FeP-O-FeP
822
400
600
800
1000
1200
Raman Shift (cm-1)
Counts

Figure 3.3 The resonance Raman spectra of iron diporphyrin (DPX). The excitation is 413.1 nm and the power is 15 mW. The top spectrum is taken from the same sample but with 1 μm acetic acid was added.

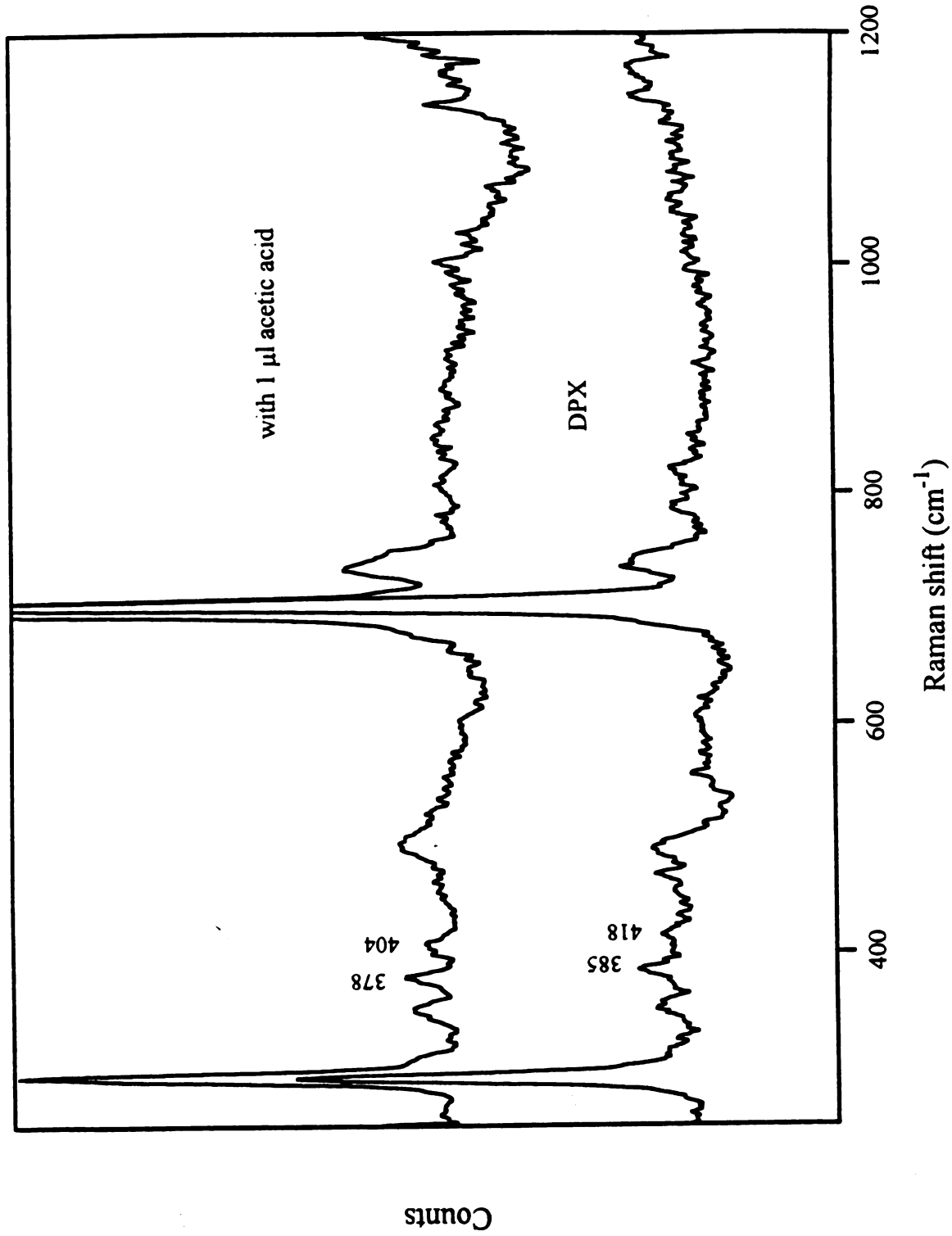
with 1 µl acetic acid
DPX
378
404
385
418
400
600
800
1000
1200
Raman shift (cm-1)
Counts

Figure 3.4 The resonance Raman spectra of iron diporphycene. The excitation is 413.1 nm and the power is 15 mW. The top spectrum is taken from the same sample but with 1 μm acetic acid was added.

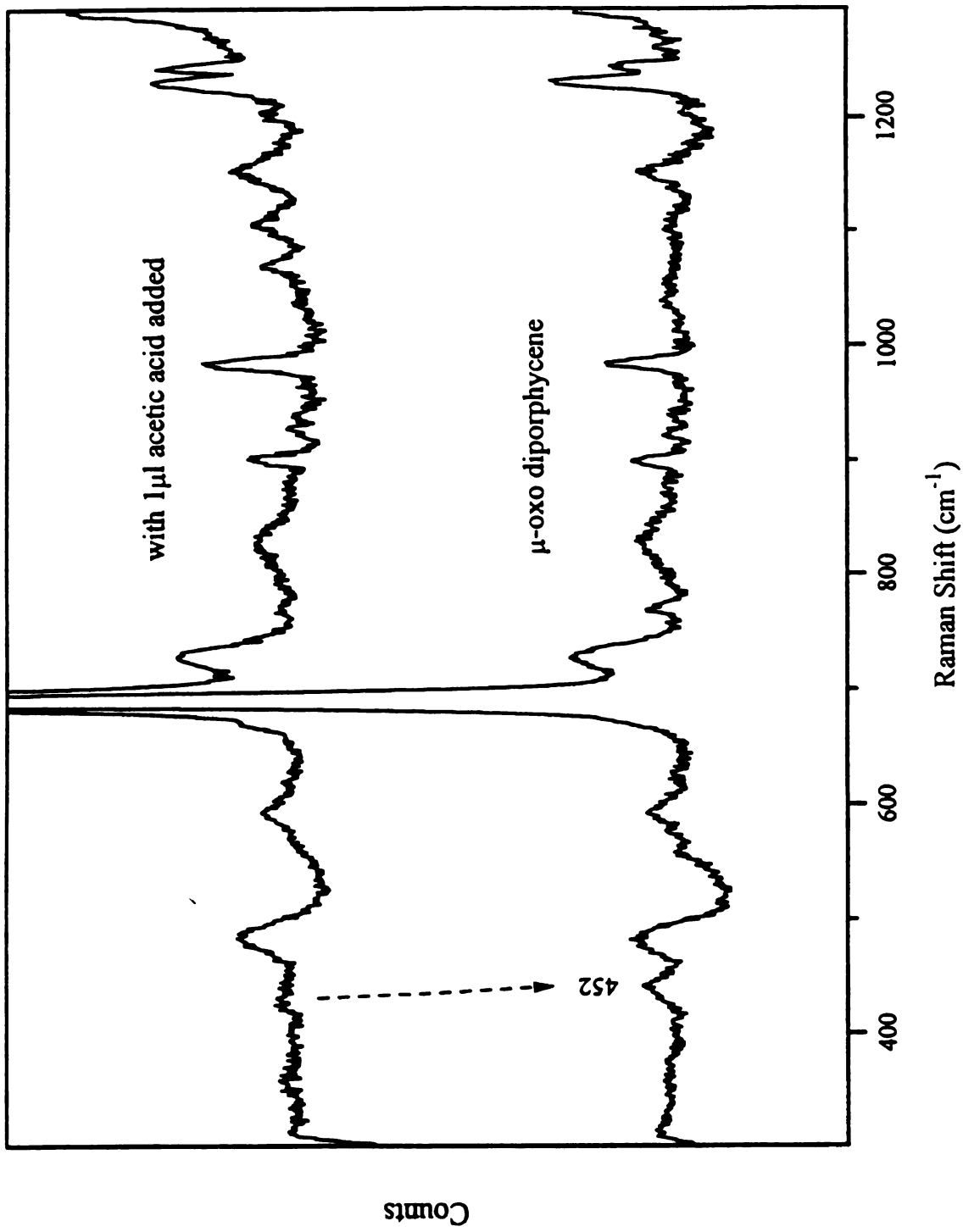
with 1µl acetic acid added
µ-oxo diporphycene
452
400
600
800
1000
1200
Raman Shift (cm-1)
Counts

Figure 3.5 The correlation of the Fe-O-Fe angle to the symmetric μ-oxo bridge vibration. The x-ray data of the Fe-O-Fe angle are from reference 10. The IR and Raman vibrational frequencies are from the literatures sited here [3.8-3.11, 3.14-3.16].

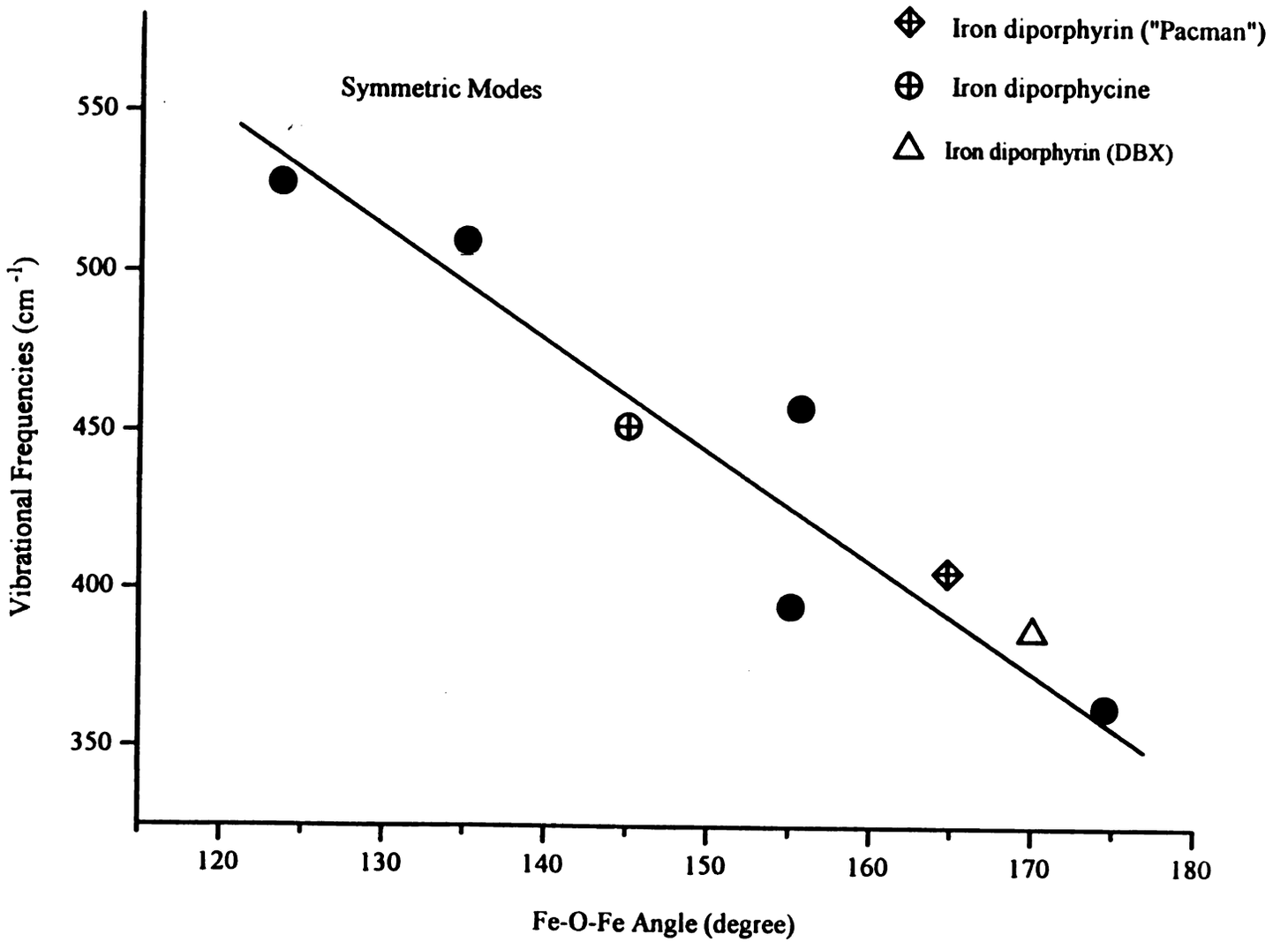
Symmetric Modes
Iron diporphyrin ("Pacman")
Iron diporphycine
Iron diporphyrin (DBX)
Vibrational Frequencies (cm -1)
550
500
450
400
350
120
130
140
150
160
170
180
Fe-O-Fe Angle (degree)

Figure 3.6 The correlation of the Fe-O-Fe angle to the asymmetric μ-oxo bridge vibration. The x-ray data and the IR and Raman vibrational frequencies are cited from the same source as Figure 3.5.

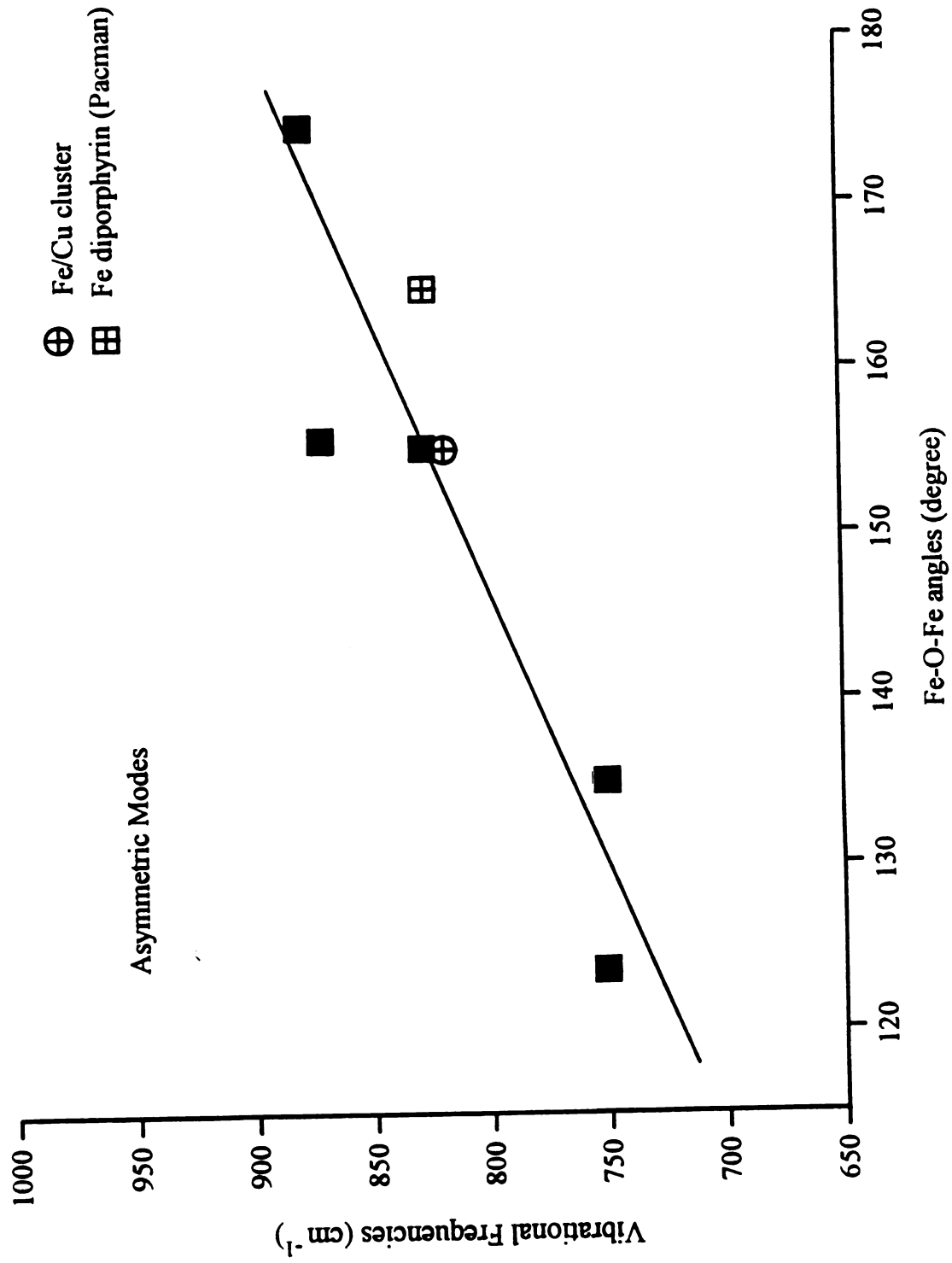
Fe/Cu cluster
Fe diporphyrin (Pacman)
Asymmetric Modes
Vibrational Frequencies (cm-1)
1000
950
900
850
800
750
700
650
120
130
140
150
160
170
180
Fe-O-Fe angles (degree)

Figure 3.7 The resonance Raman spectra of iron/copper cluster. The excitation is 413.1 nm and the power is 15 mW. The top spectrum is taken from the same sample but with 1 μm acetic acid was added.

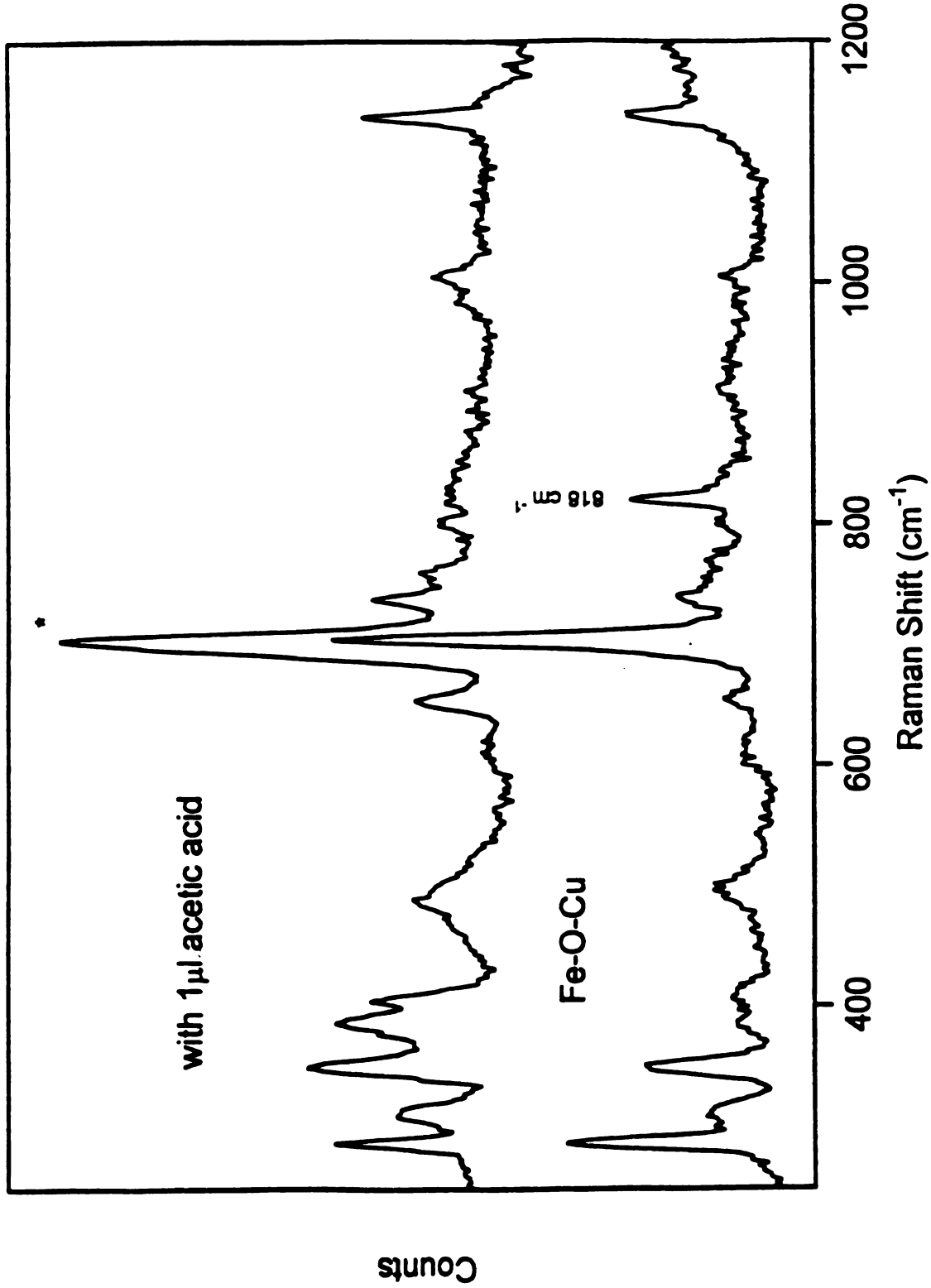
with 1µl acetic acid
Fe-O-Cu
818 cm-1
400
600
800
1000
1200
Raman Shift (cm-1)
Counts

Figure 3.8 The resonance Raman spectra of iron/iron cluster. The excitation is 413.1 nm and the power is 15 mW. The top spectrum is taken from the same sample but with 1 μm acetic acid was added.

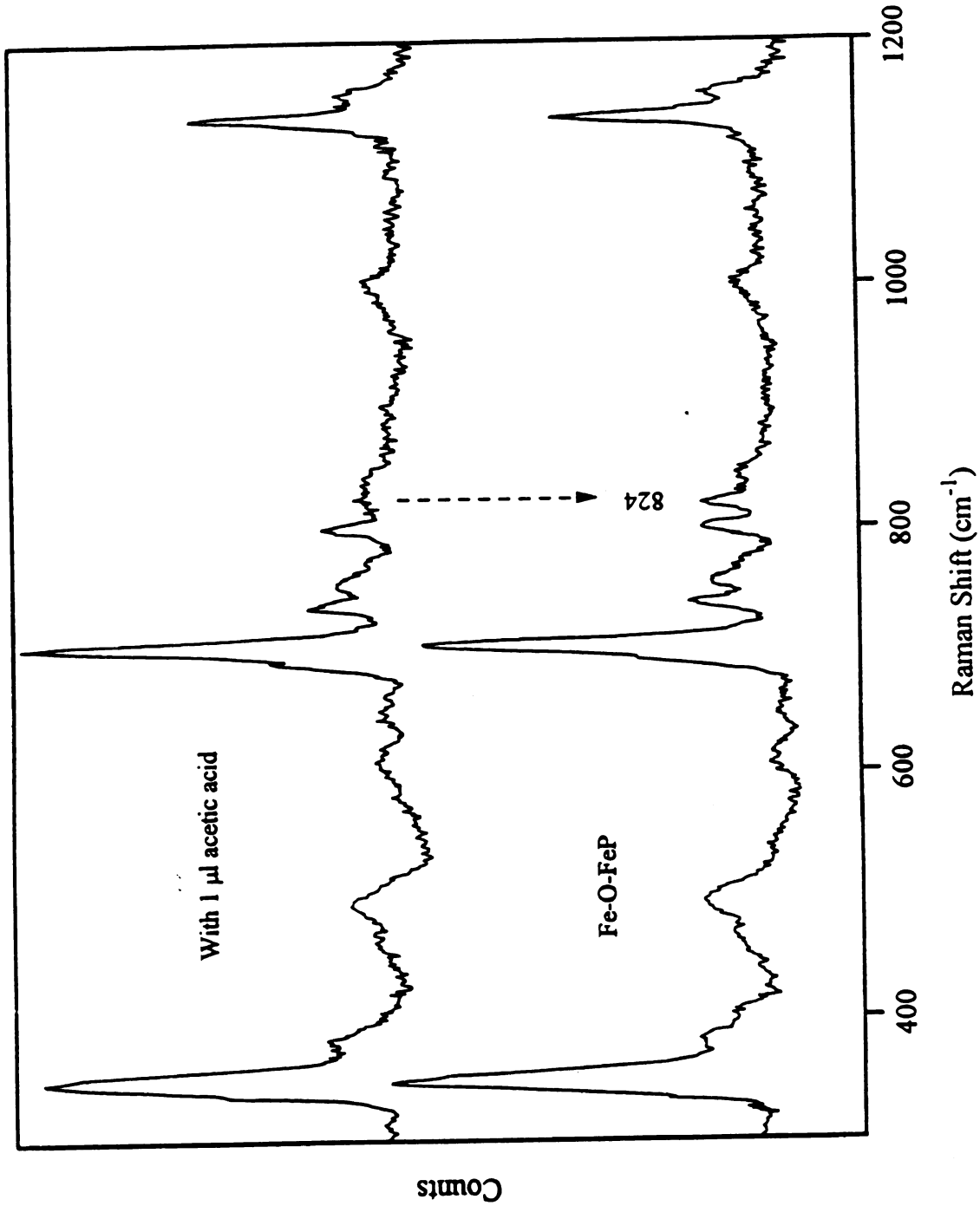
With 1 µl acetic acid
Fe-O-FeP
824
Counts
400
600
800
1000
1200
Raman Shift (cm-1)

correlation shown in Figure 3.5, in spite of the fact that both diporphyrin complexes have been strongly distorted from their slipped conformations [26] and the μ-oxo bridging angle is smaller than most μ-oxo iron porphyrins.

For the iron diporphycene μ-oxo compound, X-ray data give an Fe-O-Fe angle of 145° and the Fe-O bond length of 1.77 A°. This structure also shows the same correlation between frequency and bridging angle for the Fe-O-fe symmetric stretch [Figure 3.5]. With structures of this type, the non-bonding iron d_{yz} orbital may become involved in the Fe-O bonding interaction. The bridging oxygen, therefore, may favor an sp^2 hybridization in order to maximize the overlap of its hybrid orbitals to the iron d orbitals. The possible cooperative interactions of the d_z^2 and d_{yz} orbitals in this type of bond increases the iron to oxygen charge transfer and thus polarizes the Fe-O bond. A slightly longer Fe-O bond (1.77 A° in iron diporphycene and 1.759 A° in iron diporphyrin) and a larger angle between the two porphycene planes support this hypothesis. Thus, μ-oxo vibrational modes act as markers of the iron-oxygen bridge bond type.

Figure 3.1d shows another type of Fe-O-FeP and Cu-O-FeP complexes. In these compounds, one iron or copper center is ligated to four nitrogen atoms rather than bonded into a porphyrin ring. As predicted, this lack of symmetry enhances the asymmetric stretching vibration. Raman spectroscopy has detected asymmetric modes at 818 cm^{-1} and 824 cm^{-1} for Cu-O-FeP and Fe-O-FeP complex, respectively [Figures 3.6 and 7.7]. Similar to the diporphyrin cases, this bridge vibration is altered after protonation. If the asymmetric vibration-angle correlation in Figure 3.5 holds for this type of compound, we predict their μ-oxo angles to be approximately 155° +/- 5°. Again, positive assignment of these modes awaits isotopic labeling studies.

The main goal of the present study was to perform spectroscopic investigations of the μ-oxo bridged model compounds of cytochrome oxidase. In time-resolved resonance Raman studies of oxygen reduction in cytochrome oxidase, the vibrational

modes near the 800 cm^{-1} region were assigned to the (hydro)peroxy type intermediates [27]. However, no Fe-O stretching modes in the model peroxy compounds have been reported at such high frequencies to date. Since the μ-oxo asymmetric stretching mode was detected around the 800 cm^{-1} region, and the fact that this mode was observed in the iron porphyrin/copper cluster studied above, one should consider the possibility of μ-oxo type intermediates. These complexes are potential structural models for reaction intermediates that directly link the a_3 heme iron with the Cu_B site in cytochrome oxidase enzyme. However, if this is the case, the time course of the reaction arethsatism [28] needs to be modified since this type of compounds is suggested to occur late in the cycle of dioxygen reduction [2].

Further efforts will be focused on the vibrational characterization of other μ-oxo derivatives of the diporphyrin and/or iron porphyrin-copper clusters. With the help of the X-ray crystallographic structures and isotopically labeled samples some interesting questions raised by the kinetic studies of the dioxygen/cytochrome oxidase reaction by time-resolved resonance Raman spectroscopy can be clarified.

3.4 Acknowledgment

We thank Ms. Y. Liang and Dr. N. Bag for preparing the compounds used in this study and Dr. C. K. Chang for helpful discussion. Support is acknowledged from grants GM 25480 (to G.T.B.) and GM xxxxx (to C.K.C.) of the U.S. National Institute of Health.

References

1. For review see G. T. Babcock and M. Wikstrom, *Nature* **1992,** *356,* 301.

2. W. E. Blumberg and J. Peisach, in *Cytochrome Oxidase* T. King *eds,* **1979,** Elservier/North-Holland Biomedical Press, Amsterdam. p. 153.

3. C. A. Reed and J. T. Landrum, *FEBS Lett.* **1979,** *106,* 265.

4. A. Nanthakumar, *et al, J. Am. Chem. Soc.* **1993,** *115,* 8513.

5. K. D. Karlin, *Science* **1993,** *261,* 701.

6. K. D. Karlin, *et al, J. Am. Chem. Soc.* **1994,** *116,* 4753.

7. S. C. Lee and R. H. Holm, *J. Am. Chem. Soc.* **1993,** *115,* 5833.

8. C. Bremard, J. J. Girerd, P. Kowalewski, J. C. Merlin and S. Moreau, *Applied Spectroscopy,* **1993,** *47,* 1837.

9. P. Kowalewski, J. C. Merlin, C. Bremard and S. Moreau, *J. Mol. Struct.* **1988,** *175,* 55.

10. E. P. Plowman, T. M. Loehr, C. K. Schauer and O. P. Anderson, *Inorg. Chem.,* **1984,** *23,* 3553.

11. A. K. Shiemke, T. M. Loehr and J. Sanders-Loehr, *J. Am. Chem. Soc.* **1984,** *106,* 4951.

12. W. Li and G. Palmer, *Biochem.* **1993,** *32,* 1833.

13. E. Scheidt, S. C. Lee, R. H. Holm and G. T. Babcock, *unpublished results.*

14. J. M. Burke J. R. Kincaid and T. G. Spiro, *J. Am. Chem. Soc.* **1978,** *100,* 6077.

15. J. A. Hoffmann, Jr. and D. Bocian, *J. Phys. Chem.* **1985,** *88,* 1472.

16. C. Bremard, J. J. Girerd, P. Kowalewski, J. C. Merlin and S. Moreau, *J. Raman Spectro.* **1992,** *23,* 325.

17. C. K. Chang *et al., unpublished results.*

18. F. A. Cotton, *Chemical Applications of Grou* Theory **1990,** JohnWIley & Son.

19. W. R. Scheidt, B. Cheng, M. K. Safo, F. Cukiernik, J. C. Marchon and P. G. Debrunner, *J. Am. Chem. Soc.* **1992,** *114,* 4420.

20. A. B. Hoffman, D. M. Collins, V. W. Day, E. B. Fleischer T. S. Srivastava and J. L. Hoard, *J. Am. Chem. Soc.* **1972,** *94,* 3620.

21. S. H. Straus, M. J. Pawlik, J. Skowyra, J. R. Kennedy, O. P. Anderson, K. Spartanlian and J. L. Dye, *Inorg. Chem.* **1987,** *26,* 724.

22. K. L. Lay, J. W. Buchler, J. E. Kenny, W. R. Scheidt, *Inorg. Chim. Acta* **1986,** *123,* 91.

23. P. N. Swepston, J. A. Ibers, *Acta Crystallogr., Sect. C* **1985,** *C41,* 671.

24. T. J. Bartczak, L. Latos-Grazynski, A. Wyslouch, *Inorg. Chim. Acta* **1990,** *30,* 711.

25. J. T. Landrum, D. Grimmett, K. J. Haller W. R. Scheidt and C. A. Reed, *J. Am. Chem. Soc.* **1981***103,* 2640.

26. J. P. Fillers, K. G. Ravichandran, I. Abdalmuhdi, A. Tulinsky and C. K. Chang, *J. Am. Chem. Soc.* **1986,** *108,* 417.

27. T. Ogura, S. Takahashi, S. Hirota, K. Shinzawa-Itoh, S. Yoshikawa, E. H. Appleman and T. Kitagawa *J. Am.Chem. Soc.* **1993,** *115,* 8527.

28. C. Varotsis, Y. Zhang, E. H. Appleman and G. T. Babcock, *Proc. Natl. Acad. Sci. USA,* **1993,** *90,* 237.

CHAPTER FOUR

STRUCTURAL IMPLICATIONS ON ELECTRONIC AND VIBRATIONAL PROPERTIES OF THE PEROXYHEME INTERMEDIATE OF OXYGEN REDUCTION BY CYTOCHROME OXIDASE, A SEMI-EMPIRICAL QUANTUM CHEMISTRY STUDY

Summary

In previous studies by this lab time resolved resonance Raman spectroscopy has been used to investigate the reduction of dioxygen by the mitochondrial enzyme, cytochrome oxidase (C. Varotsis *et al.* *Proc. Natl. Acad. Sci.* **1993,** *90,* 237). A series of intermediates in the O_2 reduction cycle were detected and assigned to oxy (Fe^{2+}-O_2), peroxy [Fe^{3+}-O^--O^-(H)] and ferryl (Fe^{4+}=O). Simulation of the kinetic scheme of the postulated reaction sequence indicates that following rapid O_2 binding, a series of progressively slower steps occurs. This process allows the various transient species to build up to the concentration sufficient for their detection by time resolved techniques. In the work reported in this chapter, intermediate neglect of differential overlap (INDO) semi-empirical calculations were performed on oxy and peroxy species to evaluate the effect of electron transfer on bond cleavage and bond formation during the reduction of O_2 to water. The Fe^{3+}-O^--O^-(H) bonding interaction and excited state transition energies were calculated. A group of low lying charge transfer states were determined for the peroxy species. The impact on electronic configurations and dioxygen bonding structures are compared to experimental results. The charge transfer from iron to dioxygen is sensitive to the dioxygen orientation and its π^* orbital interactions with iron d orbitals. Our results indicate that the peroxy species is photoreactively different from the oxy species.

4.1 Introduction

Cytochrome oxidase is the terminal enzyme in the respiratory chain of most aerobic organisms. This mitochondrial enzyme catalyzes the four-electron reduction of molecular oxygen to water and couples this thermodynamically favorable reaction to the generation of an electrochemical proton gradient across the membrane. Two hemes, cytochrome a and cytochrome a_3, and two redox active copper centers, Cu_A and Cu_B, mediate the redox chemistry and coordinate the translocation of protons. Cytochrome a_3 and Cu_B combine to form a binuclear cluster that is the site of dioxygen binding and reduction to H_2O. The remaining redox metal active sites function as electron transfer mediators between cytochrome c and the binuclear center [1-4].

The characteristics of dioxygen binding to proteins has been a fundamental question that has concerned researchers studying this and other oxygen-metabolizing enzymes. Besides cytochrome oxidase, dioxygen reactions with cytochrome P-450 [5], hemoglobin [6] and myoglobin [7] have been extensively studied by both experimental and theoretical methods. Since the determination of the X-ray structure of hemoglobin and myoglobin in the sixties, many synthetic heme-dioxygen complexes have been prepared [8]. The necessary and sufficient conditions for dioxygen binding to a heme group are now understood qualitatively well, and model compounds have played a particularly important role in developing this understanding. However, the local environments in the protein, which are different from the model compounds, may substantially modify the dioxygen binding geometry and, thus its reactivity. For instance, hydrogen bonding between the terminal oxygen and the distal residue in oxy hemoglobin and oxy myoglobin has been demonstrated [6, 7].

Some reaction intermediates, peroxy species, for example, proposed in the dioxygen reactions with cytochrome oxidase and cytochrome P-450, are unstable and

thus, are unable to be prepared experimentally in model systems easily. The use of theoretical quantum chemistry to study the dioxygen binding properties in these biological systems, therefore, is a natural alternative and has been widely applied in the last decade [9]. Different dioxygen binding transient structures and conformations developed from experimental evidence can be constructed and examined by theoretical methods. Since the use of the entire protein structure in a quantum chemical study is too complicated to be practical, many theoretical studies have employed model iron-porphyrin complexes [10-21]. Many of these works have examined the possible electronic configurations of the Fe-O2 complex and its electronic ground state for which both a superoxo type electronic structure, Fe(III)-$O2^-$, and a neutral spin-paired electronic structure, Fe(II)-O2, are supported by experimental data [22, 23]. These computational results, in general, are quite sensitive to the quantum chemical methods used and the surrounding ligand environment assumed. The interaction with the environment may thus be an important factor that influences the dioxygen geometry in real systems and could be responsible for part of the differences observed between molecular model computations and experimental data. Nevertheless, these works have reflected the diverse range of chemistry encountered in these systems and have given useful information in understanding the catalytic processes involved with dioxygen complexation and reaction.

Dioyxgen reduction by cytochrome oxidase has been extensively studied by a variety of spectroscopic techniques [24-59]. In biological systems the activation and bond cleavage of dioxygen require the injection of electrons into the reactive site and subsequent electron and proton transfer steps to reduce dioxygen into water. Due to the unique ligand-binding kinetics of the binuclear center, the rate limiting step in the overall process occurs late in the proton transfer reaction. Reaction intermediates during this catalytic cycle, therefore, can build up to a detectable level for experimental measurements [34]. Because of its advantage in directly probing the protein binding-

site structures, time-resolved resonance Raman spectroscopy adapting a Gibson-Greenwood flow-flash scheme [24-25] has been applied successfully to this purpose [27]. This approach has stimulated extensive studies of the dioxygen reduction reaction by fully reduced cytochrome c oxidase [27-43]. As shown in Figure 4.1a, several intermediate species have been detected and a basic reaction scheme for the oxidation of fully reduced cytochrome oxidase by dioxygen has been proposed [34]. The kinetic simulation of concentration-time profiles for these proposed intermediates is given in Figure 4.1b.

In spite of significant progress in understanding the dioxygen reduction reaction catalyzed by the cytochrome oxidase enzyme, many questions remain. One of the more controversial issues is the assignment of the signals associated with the possible peroxy species, a key intermediate in the scheme shown on Figure 1a, in the time-resolved resonance Raman experiments. First, the short life-time of this possible intermediate makes its detection difficult. Secondly, the complicated electronic configurations of the possible end-on and side-on dioxygen binding conformations to the heme and, the coupling of the Fe-O bond to the peroxy O-O bond may give this species unique structural and, therefore, vibrational properties. Thirdly, the possible hydrogen bonding and/or Cu_B center ligation to the terminal oxygen in the end-on conformation can also contribute to the structure and function of this species. As the function of the protein cannot be separated from the fundamental chemistry of the particular metal active-site structure and its local environments, synthetic models of small molecular complexes that resemble these intermediates have been given great consideration [8, 61-63] and have helped us to understand several reaction intermediates of oxygen reduction by cytochrome oxidase [60]. However, the only porphyrin-based peroxy species has been prepared synthetically and characterized by X-ray crystallography is a Mn porphyrin peroxy complex [63]. The semi-empirical quantum mechanical methods, therefore, have been employed here to study possible

Figure 4.1 a). the proposed dioxygen reduction scheme by cytochrome oxidase, b). kinetic simulation of the concentration-time profiles for proposed intermediates, reprinted from C. Varotsis *et al. Proc. Natl. Acad. Sci.* **1993,** *90,* 237

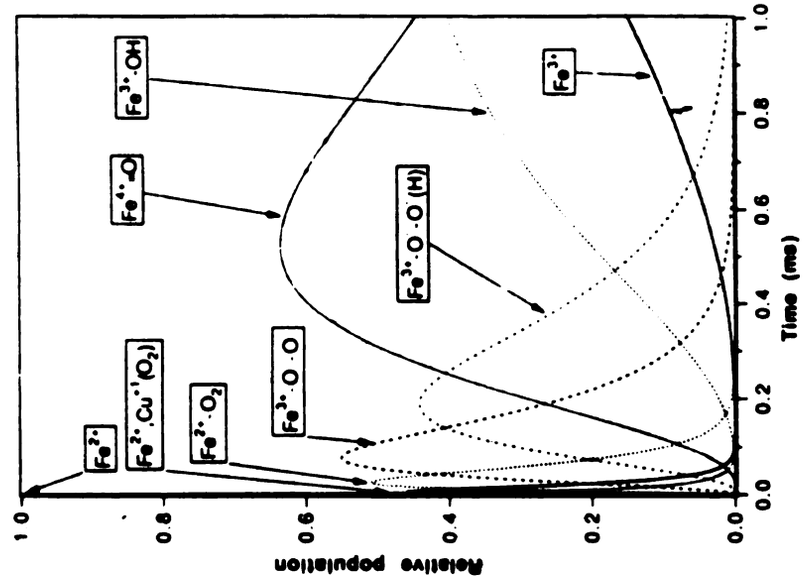
Relative population
Time (ms)
0.0
0.2
0.4
0.6
0.8
1.0
Fe^{2+}
$Fe^{2+}.Cu^{+1}(O_2)$
$Fe^{2+}.O_2$
$Fe^{3+}.O.O$
$Fe^{3+}.O.O(H)$
$Fe^{4+}.O$
$Fe^{3+}.OH$
Fe^{3+}

b

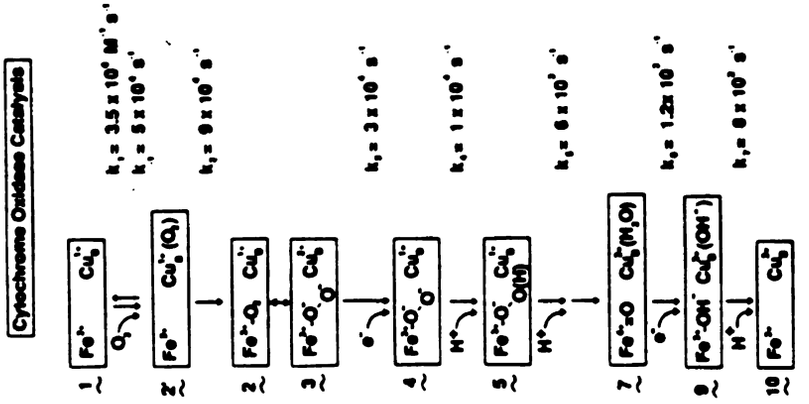
Cytochrome Oxidase Catalysis
$k_1 = 3.5 \times 10^6\ M^{-1}\ s^{-1}$
$k_{-1} = 5 \times 10^3\ s^{-1}$
$k_2 = 9 \times 10^3\ s^{-1}$
$k_3 = 3 \times 10^3\ s^{-1}$
$k_4 = 1 \times 10^3\ s^{-1}$
$k_5 = 6 \times 10^3\ s^{-1}$
$k_7 = 1.2 \times 10^3\ s^{-1}$
$k_9 = 8 \times 10^3\ s^{-1}$
O_2
e^-
H^+
e^-
H^+
1
2
2
3
4
5
7
9
10

a

Figure 4.2 The peroxy structures used in our calculations: a). standard peroxy; b). hydroperoxy-1, a proton is shifted from imidazole ring to terminal oxygen; c). hydroperoxy-2, a proton is added to the standard peroxy.

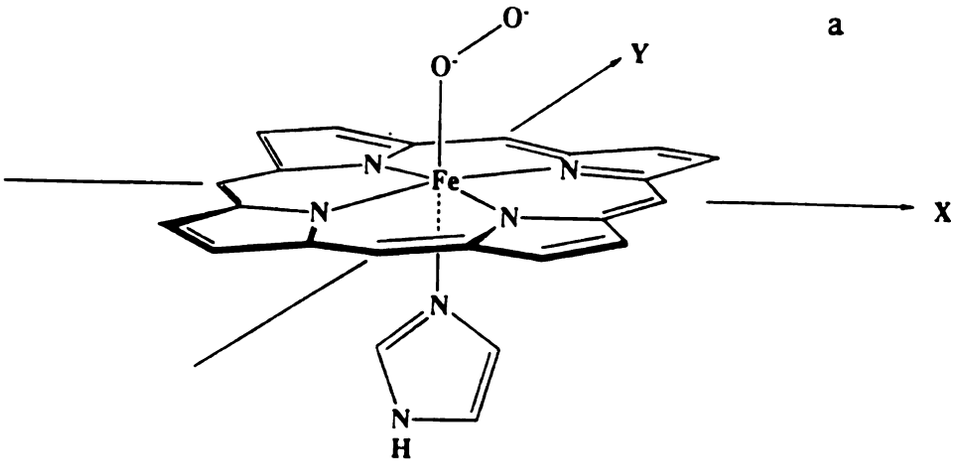
a
O
O
Y
N
Fe
N
N
N
X
N
N
H

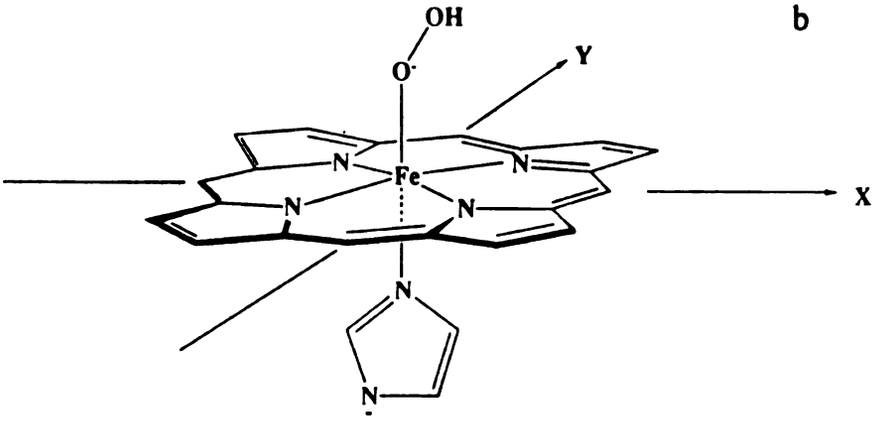
b
OH
O
Y
N
Fe
N
N
N
X
N
N

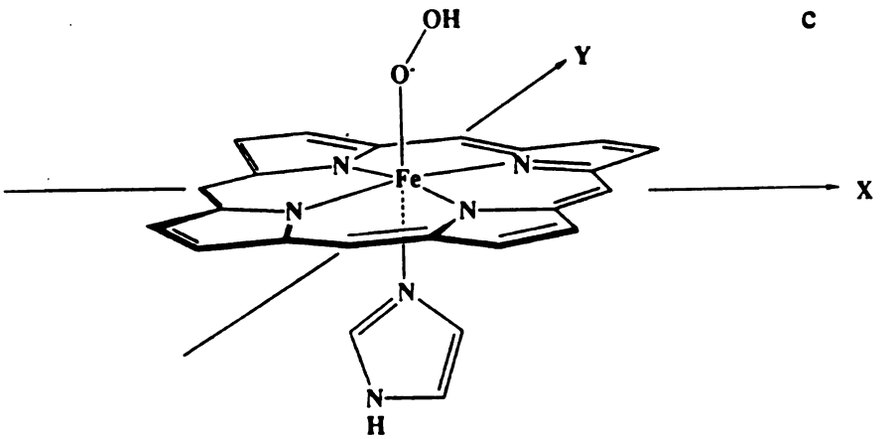
c
OH
O
Y
N
Fe
N
N
N
X
N
N
H

heme-peroxy intermediates. The structures of the standard peroxy form and its protonated forms (hydroperoxy) [see Figure 4.2] were chosen as targets to investigate their electronic and structural properties and their possible biological relevance to the cytochrome oxidase reaction sequence.

Several *ab-initio* and semi-empirical calculations have been done to study the electronic structures of porphyrin derivatives [65], and the O_2 binding to the porphine peripheries [9-21]. For model compounds involving a porphyrin macrocycle and its ligands, the use of *ab-initio* methods is prohibitive [66] due to the large number of basis functions required to represent the system accurately. Among the semi-empirical quantum chemistry methods, a computational package, ZINDO [67-70], is our choice for studies of possible dioxygen intermediates catalyzed by the cytochrome oxidase because of its proven ability to treat transition metal ions (heme) [10-12, 17] and the capability of our computer facilities.

4.2 Methods

All calculations of the model peroxy complexes were carried out in a SGI-xz-4000 machine by using a spin-restricted open-shell INDO method, which has been described in detail elsewhere [67-70]. Empirical parameterization with the Weiss-Mataga-Nishimoto formula was employed [71]. The electronic spectra were calculated by using single excitation within the INDO semi-empirical approximations (INDO/s). In general, the configuration interaction (CI) calculations are performed by exciting electrons from the occupied orbitals of a reference configuration, often the ground state configuration, into virtual orbitals. As many as possible ground state orbital and excited virtual orbitals should be used in carrying out CI calculations to improve the overall accuracy of the molecular wave function. In our work here, CIs were considered by exciting the electron from the highest 16 occupied orbitals to the lowest 8 unoccupied orbitals, as the number of CIs are limited to 210 by the software.

These configurations were generated by using Rumer diagram techniques [70]. Oscillator strengths were also calculated for each excited state relative to the ground state.

The geometrical parameters for the peroxy model compound were modified from X-ray data [23]. The porphyrin crystal structure was modified to a porphine-like conformation [Figure 4.2a-c]. D_{4h} symmetry labels were used for the calculated MOs and states as they are traditionally in porphyrin chemistry, although the actual complex has lower symmetry. The Fe-$N_{porphyrin}$ distance was set to 2.01 A^{o}. The iron-$N_{imidazole}$ distance was set to 2.02 A^{o} without any further modification during the calculations. The orientation of the complexes was such that the pyrrole nitrogens of the porphyrin macrocycle bisect the x and y axes and the Fe binding atom of the axial ligands lie on the z axis [Figure 2]. The imidazole ligand was basically in the y-z plane. The bent end-on dioxygen binding geometry to the porphyrin plane was used throughout the ground state and excited state transition calculations except where otherwise indicated.

4.3 Results

a). Changes in end-on oxygen position vs. electronic configurations and charge transfer.

The computed net atomic charges for a doublet peroxy species (Figure 4.2a) at various Fe-O1 distances but at a fixed O1-O2 distance are given in Table 4.1. In the remainder of this chapter, O1 will be designated the bound oxygen and O2 will be designated the terminal oxygen. The correlations of net charge distribution at the iron, bound oxygen and terminal oxygen vs. the Fe-O1 distance are plotted on Figure 4.3. An interesting result is that the net charge distribution at the oxygen moiety is similar to that in superoxo species. There is substantial amount (> 0.7) of excess negative charge at the terminal oxygen. However, the net excess negative charge is much less

on the bound oxygen. The rest of the negative charge is delocalized into the porphyrin macrocycle, particularly on the nitrogen atoms. Previous semi-empirical calculations of dioxygen binding to ferrous heme model compounds also gave a similar charge distribution pattern [20]. The iron is at an intermediate electron distribution state between the electronic configurations of the ferrous and ferric states. The Mulliken population analysis confirms these results: the d-orbital population is $(d_{x^2-y^2}) = 1.98$, $(d_{xz}) = 1.95$, $(d_{yz}) = 1.13$, $d_{z^2} = 0.66$ at r(Fe-O1) = 1.90 A° and $(d_{x^2-y^2}) = 1.97$, $(d_{xz}) = 1.96$, $(d_{yz}) = 1.03$ and $d_{z^2} = 0.67$ at r(Fe-O1) = 2.1 A°. While the net charge density at the terminal oxygen remains approximately constant, an increase in Fe-O1 distance, which minics a photodissociation process, enhances the charge transfer from iron to the bound oxygen (Figure 4.3). However, this increase is not large enough to make an Fe(III)-O^--O^- electron configuration, a conventional structure for the peroxy species that is often proposed in the literature [34]. On the other hand, an almost linear correlation of the increase of net charge density on the oxygen atoms to the increase of the Fe-O1 bond length [Figure 3] suggests that there are not other bond breaking/bond making processes accompanying the photodissociation of peroxy intermediates. This is consistent with photolability results in the time-resolved resonance Raman on the early time scale of the dioxygen reaction with fully reduced cytochrome oxidase [31].

Table 4.2 shows the ground state atomic orbital compositions of the principal molecular orbitals used in the configuration interaction calculations of a heme-peroxy complex at Fe-O1 distances of 1.9 A° and 2.1 A°. For comparison, the ground state orbital compositions of standard dioxygen-heme binding structures at identical Fe-O distance are also listed (Table 4.3). For the orbital occupancies of the oxy-heme complex, the results from our calculations are similar to those reported in the literature [10]. The major components of the HOMOs and LUMOs are basically a_{1u}, a_{2u} and eg configurations, which is consistent with the four orbital model of porphines [72]. Relative to the oxy-heme complex, the major changes in the orbitals of the peroxy-

Figure 4.3 The correlations of net charge distribution at iron, end-on oxygen and terminal oxygen vs. the Fe-O- distance. Fe-O-O angle equals to 110.8^{O}, O-O bond length equals to 1.45 A^{O}.

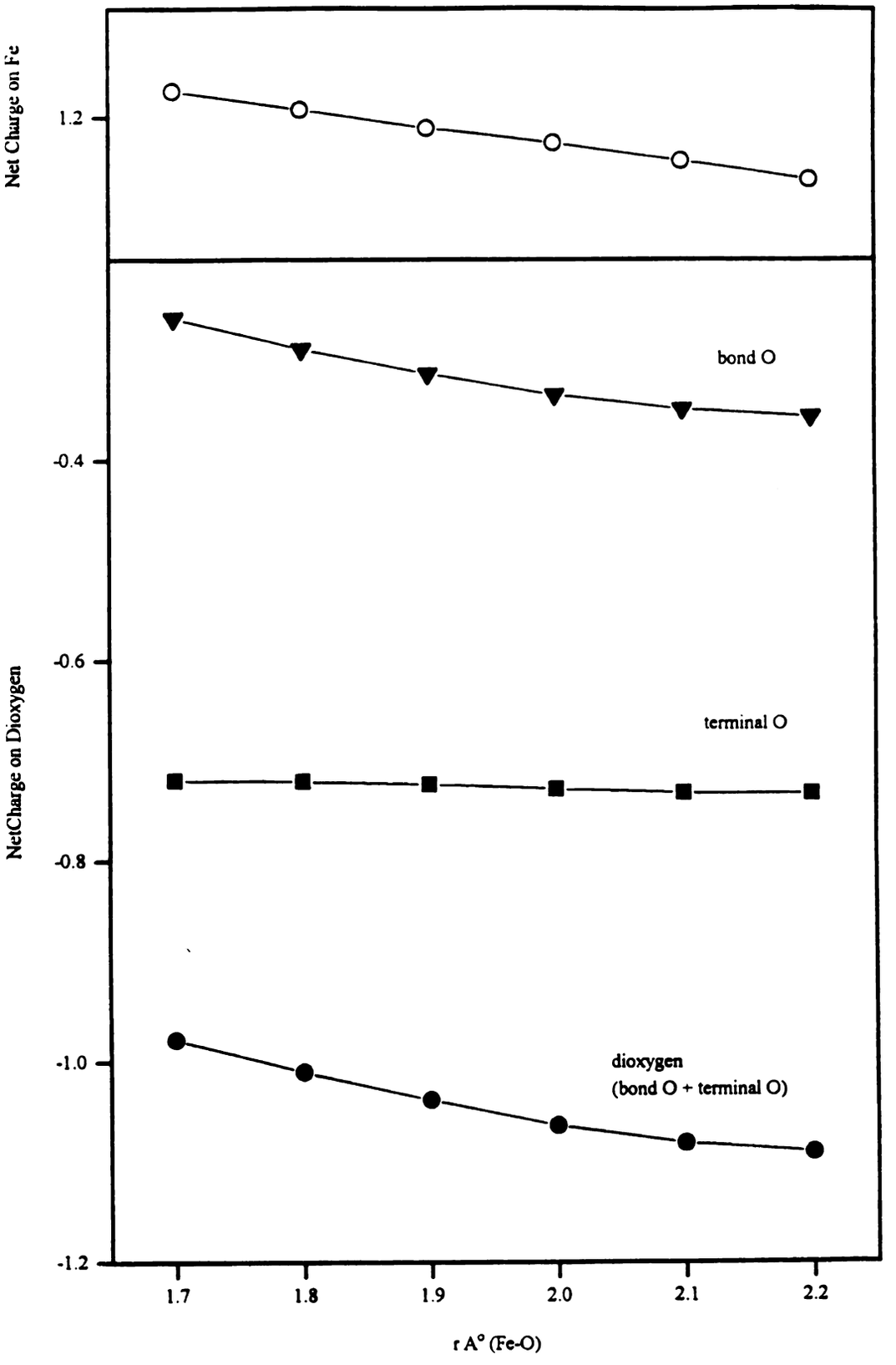
Net Charge on Fe
1.2
bond O
-0.4
-0.6
terminal O
NetCharge on Dioxygen
-0.8
-1.0
dioxygen
(bond O + terminal O)
-1.2
1.7
1.8
1.9
2.0
2.1
2.2
r A° (Fe-O)

Figure 4.4 The 3-D view of the computed electronic spectra of the standard peroxy species at different Fe-O- distances.

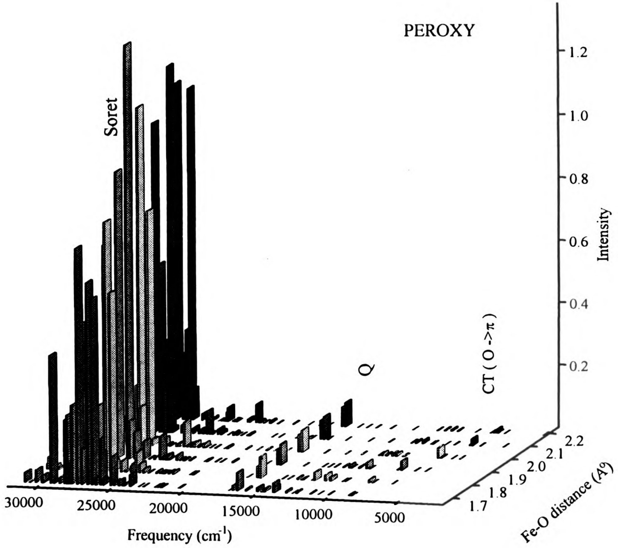
PEROXY
Soret
Q
CT (O ->π)
Intensity
0.2
0.4
0.6
0.8
1.0
1.2
Frequency (cm-1)
30000
25000
20000
15000
10000
5000
Fe-O distance (A°)
1.7
1.8
1.9
2.0
2.1
2.2

Figure 4.5 Computed electronic spectrum of the standard peroxy species: Fe-O =1.9 A^{O}, O-O = 1.45 A^{O}.

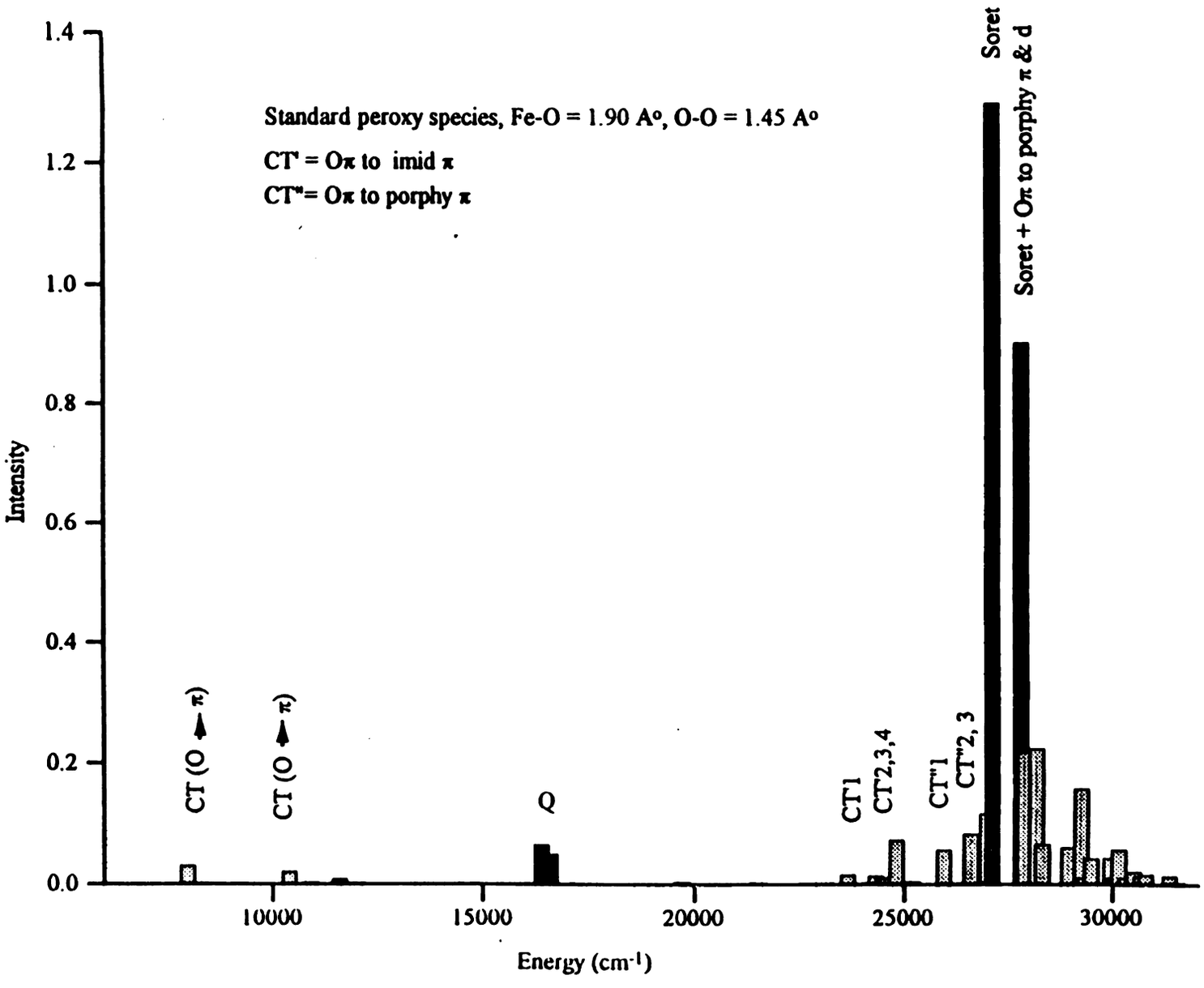
Standard peroxy species, Fe-O = 1.90 A°, O-O = 1.45 A°
CT' = Oπ to imid π
CT"= Oπ to porphy π
Intensity
1.4
1.2
1.0
0.8
0.6
0.4
0.2
0.0
CT (O → π)
CT (O → π)
Q
CT1
CT'2,3,4
CT"1
CT"2, 3
Soret
Soret + Oπ to porphy π & d
10000
15000
20000
25000
30000
Energy (cm-1)

heme complex occur in the HOMOs. The two highest occupied MOs, lying slightly higher than the porphyrin a_{1u} and a_{2u} orbitals, are d_{yz} and oxygen π in character, which demonstrates the importance of these orbitals in the peroxy-heme species. Table 4 and 5 give the excited state transitions and major components for the above peroxy structure at Fe-O distances of 1.9 A^{o} and 2.1 A^{o}. Figure 4.4 gives three-dimensional views of the electronic transitions of this peroxy species at different Fe-O1 distances. Consistent with the analysis of the charge distribution data discussed above, the optical spectrum clearly shows that a set of oxygen to porphyrin charge transfer transitions lie below the Q band absorption range. Furthermore, these CT bands are photoreactive and can lead to dissociation, as an increase of Fe-O1 bond distance moves these CT states to lower energies. This behavior is similar to the oxy-heme species: decreasing energy of the charge transfer transitions with increasing iron-dioxygen distance and no barrier to dissociation [10]. This observation is also supported by time-resolved resonance Raman experimental results of the dioxygen reaction with fully reduced cytochrome oxidase [31]. More specifically, the above experiments have demonstrated that both the oxy adduct and the three-electron-reduced species (peroxy equivalent) are photolabile at high photon flux. The requirement for high photon flex presumably arises from the low transition oscillator strengths suggested by the results of our calculations presented here (oscillator strength ~ 0.03 for the charge transfer transitions of the peroxy species). There are also several sets of charge-transfer transitions between the Q bands and Soret bands. Both O π to porphyrin π CT and porphyrin $\pi - \pi$ transitions are photodissociative. However, a group of porphyrin π to imidazole π CT transitions which carry intermediate oscillator strength and occur between the Soret and Q bands (Figure 4.4) are stable during the photodissociation of the iron-peroxy complex, because these transitions are not directly involved in the peroxide-heme bonding.

As discussed previously, the local protein environment, particularly the hydrophobic nature of the heme pocket formed by the amino-acid residues in its vicinity may have a significant influence on oxygen binding properties and structures. The existence of hydrogen bonding between the terminal oxygen and the distal residues has been suggested in the proposed peroxy intermediates in the oxidase reaction [1, 34]. The presence and the nature of the axial ligand, which is on the opposite side of the porphyrin plane with respect to the dioxygen ligand, is also expected to play a role in influencing iron-oxygen bonding, in particular because this ligand governs in part the electronic charge-transfer from the iron to the oxygen atoms. Thus, an isomeric form of the peroxy species, formed by shifting a proton from the imidazole to the terminal oxygen, hydroperoxy-1 (Figure 4.2b), and a protonated peroxy, formed by adding an additional proton to the terminal oxygen of the standard peroxy structure, hydroperoxy-2 (Figure 4.2c), are also considered here. The ground state orbital occupancies of the hydroperoxy-1 and hydroperoxy-2, are listed in Table 4.6 and 4.7. The computed charge distribution on isomer hydroperoxy-1 at different Fe-O1 distances is listed on Table 4.8. The optical transitions of the peroxy, its isomer, hydroperoxy-1 and the protonated peroxy, hydroperoxy-2, at standard nuclear configurations, Fe-O1 = 1.90 A^0 and O1-O2 = 1.45 A^0 are plotted in Figures 4.5 to 4.7. The changes in the optical spectra are due to perturbations to both ground and excited states (compare Table 4.2 to Table 4.6 and 4.7). The protonation of the terminal oxygen lowers the oxygen π orbitals in energy more than that of the porphyrin π orbitals. The low-lying oxygen π to porphyrin CT bands, which are significant in the peroxy species, are eliminated in the terminal oxygen protonated forms, hydroperoxy-1 and -2. On the other hand, bands due to the charge transfer from imidazole to the porphyrin and to the d orbitals of the iron become predominate in the hydroperoxy-1 isomer, presumably because a proton is transferred from the imidazole ring to the terminal oxygen on the opposite side to form an imedazolate ligand. Similarly, the

spectra of the protonated peroxy species, hydroperoxy-2, lacks not only the low-lying oxygen π to porphyrin CT bands but also the imidazolate to porphyrin ring-ring transitions. The addition of the proton causes a relatively large perturbation in the peroxy electronic configuration. This effect results in the production of excited state transitions with greater intensity in the Soret band region [see Figure 4.7]. The most interesting transitions in the hydroperoxy-2 species formed during the protonation step discussed above are the iron d orbitals to porphyrin charge transfers. These bands mix into the Soret transitions and neutralize the negative charge distribution of the porphyrin ring, particularly on the Npyrrole atoms (see Table 4.11).

b). Changes in oxygen-oxygen bond length vs. the electronic configurations and charge transfer.

The computed net atomic charges for a doublet state peroxy species with an end-on geometry at various O1-O2 distances but a fixed Fe-O1 distance (1.90 A^{o}) are given in Table 4.9. The correlations of net charge distribution at iron, bound oxygen (O1) and terminal oxygen (O2) vs. the O1-O2 distance are plotted in Figure 4.8. For comparison, the charge distribution in hydroperoxy-1 and hydroperoxy-2 are also listed in Tables 4.10 and 4.11. In contrast to the dissociation of the peroxy species from the heme moiety (Figure 4.3), extension and eventual cleavage of the O-O bond leads to significant electron rearrangements. This is best shown in the change of the net charge distribution vs. the increase of the O-O bond distance (Figure 4.8). Similar to the change in Fe-O1 bond distance (Figure 4.3), the analysis of the charge distribution at various O1-O2 distances indicates that this peroxy complex also prefers a Fe-O-O^{-} configuration mixed with Fe(II) and Fe(III) rather than a pure the Fe(III)-O^{-}-O^{-} form. It has been well established by resonance Raman experiments that the ν_4 vibration mode can serve as an oxidation state marker of the heme group [73]. The ν_4 band occurs at 1355 cm^{-1} for the ferrous species (Fe^{2+}) and at 1371 cm^{-1} for the ferric

species (Fe^{3+}). The time-resolved resonance Raman spectra of dioxygen reactions with the fully reduced cytochrome oxidase [31] show that the ν_4 band shifts from 1355 cm^{-1} to 1371 cm^{-1} when a photon photolyzes CO and initiates dioxygen reduction to form initial O_2-a_3 complex. However, in the time scale from 100 μs to 500 μs, the diminishing 1355 cm^{-1} band begins to recover to a level comparable with the 1371 cm^{-1} peak. This observation, whose origin is unclear in terms of the previous discussion, therefore, can be explained by the possible formation of Fe(II)/Fe(III)-O-O^- intermediate rather than the Fe(III)-O^--O^- species.

While the charge density distribution undergoes little change at the porphyrin ring and at the imidazole as the terminal oxygen moves from the bound oxygen (Table 4.10), increasing distance favors the charge transfer from the iron and porphyrin ring to the dioxygen, particularly to the terminal oxygen. The most interesting observation is that while the net charge on the end-on oxygen atom increases steadily, the changes in net charge on iron and the terminal oxygen atom are much larger. The rapid increase in negative charge at terminal oxygen at r(O-O) from 1.2 to 1.45 A° indicates strong potential reactivity of the terminal oxygen. The shallow well structure at about r(O-O) =1.45 A° for the terminal oxygen gives an indication of a metastable form of this species. This bent end-on structure, as its terminal oxygen extends away from the porphyrin moiety and accumulates significant net negative charge, is rendered more reactive with a positive charge or a proton to form a hydrogen-bonded structure as compared to the side-on oxygen conformation [9]. Since the charge distribution is different between the two oxygens, the terminal oxygen is easier to break away than the bound oxygen when a proton or the Cu_B cluster attacks the peroxy species. The plot of the charge distribution vs. the O-O bond distance Figure 4.8 reveals that the transition region from the oxy to peroxy and, to the possible cleavage of the terminal oxygen, occurs in the range of r(O-O) distance from 1.40 A° to the 1.48 A°. A detailed comparison of the electronic transitions of the peroxy (Figure 4.5) and

hydroperoxy forms (Figures 4.6 and 4.7) shows that the O π to porphyrin π charge-transfer transitions in the spectral region between the Q bands and Soret bands gain considerable intensity in the hydroperoxy forms (see also Figures 4.9-4.11, three dimensional plots of the hydroperoxy-1 and hydroperoxy-2 at different Fe-O and O-O bond distances), which suggests that the cleavage of the oxygen-oxygen bond rather than the iron-bound oxygen bond is more favorable than dissociation of the dioxygen species under these conditions. The heterogeneous dissociation mechanism of the terminal oxygen gives the proposed ferryl species (scheme 1). Recently, light-induced cleavage of the oxygen-oxygen bond was observed in the low temperature Raman studies of peroxy-heme complex [74].

c). Changes in C_{porphy}-Fe-O-O torsion angles and dioxygen rotation barrier above the porphyrin plane.

Table 12 lists the computed net atomic charges for the standard, doublet state peroxy species at various Fe-O torsion angles. The rotation of the peroxy species above the porphyrin plane does not produce any noticeable modifications of the electron density. This result indicates that there is little mixing and coupling between the oxygen π^* orbital and porphyrin a_{1u} and a_{2u} orbitals. Although the peroxy species discussed here is taken as occuring in a bent, end-on binding conformation, certain interactions between iron d_{xy} and dioxygen π^* orbitals are expected. However, this type of d_{xy} to π^* back bonding has to be weak in the bent, end-on peroxy structure; otherwise, rotating the O-O above the porphyrin plane will significantly alter the charge distribution on the oxygen atoms.

Table 4.1. Charge distribution on a standard peroxy-heme structure: Fe-O-O angle equals to 110.8^{O}, O-O bond length equals to 1.45 A^{O}.

r (Fe-O) A^{O}	Q (Fe)	Q (O1)	Q(O2)	Q (Porphyrin)	Q (Imidazole)
1.7	1.236	-0.258	-0.720	-1.332	0.074
1.8	1.210	-0.289	-0.720	-1.287	0.086
1.9	1.184	-0.314	-0.724	-1.241	0.095
2.0	1.163	-0.335	-0.729	-1.203	0.104
2.1	1.138	-0.349	-0.733	-1.164	0.108
2.2	1.112	-0.357	-0.734	-1.133	0.112
2.3	1.087	-0.362	-0.732	-1.111	0.118

Table 4.2. Ground State Orbital Description of the Standard Peroxy Complex

Orbital #	Orbital Occupancies Fe-O1 = 1.90 A^o	Fe-O1 = 2.1 A^o
90	62% d_{xy}; 24% porphy σ; 4% d_z^2	99% eg*
89	99% eg*; 1% d_x^2-y^2	66% d_{xy}; 27% porphy σ; 4% d_z^2
88	96% eg*; 2% d_z^2	90% b_{1u}; 5% d_z^2; 3% d_{xy}
87	100% b_{1u}	52% imid π; 17% O π; 11% imid σ; 22% porphy π
86	82% imid π; 17 % imid σ	81% imid π; 17 % imid σ
85	99% b_{2u}	100% b_{2u}
84	69% imid σ; 25% imid π	88% imid σ; 5% imid π; 2% d_z^2
83	82% imid π; 13% imid σ	81% imid π; 15% imid σ
82	99% eg*	98% eg* ;
81	98% eg*	96% eg*; 2% O π
80	85% d_{yz}; 13% O π	93% d_{yz}; 5% O π
79	82% O π; 9% d_z^2	69% O π; 12% d_z^2;13% O σ
78	56% O π; 39% a_{1u}; 4% d_{yz}	92% O π; 3% d_{yz}
77	47% O π; 45% a_{1u}; 4% d_{yz}	98% a_{1u}
76	98% a_{2u}	99% a_{2u}
75	52% d_{xz}; 41% porphy π	54% eg; 44% d_{xz}
74	88% eg; 8% O π	90% eg; 4% O π
73	76% d_x^2-y^2 ; 15% a_{2u}; 1% O π	38% d_x^2-y^2 ; 60% a_{2u}
72	83% eg; 14% d_x^2-y^2 ; 1% O π; 1% imid π	98% eg
71	100 b_{1u}	53% d_x^2-y^2 ; 40% porphy
70	68% imid π; 23% porphy π; 8% d_{xz}	98% b_{1u}
69	53% eg; 19% d_{xz}; 1% O π	
68	85% eg; 7% d_{xz}; 6% imid π	
67	98% eg; 1% d_{yz}	

Table 4.3. Ground State Orbital Description of the Standard Oxy Complex

Orbital #	Orbital Occupancies Fe-O1 = 1.90 A^o
90	98% eg*; 2% d_z^2
89	95% eg*
88	61% d_{xy}; 27% porphy σ; 1% d_z^2
87	100% b_{1u}
86	99% imid π*
85	93% imid π*; 2% d_z^2
84	100% b_{2u}
83	98% imid π*
82	64% eg*; 22% O π; 22% d_{yz}
81	95% eg*; 2% O π; 2% d_{yz}; 1% d_{xz}
80	48 % eg*; 37% O π; 12% d_{yz}
79	99% a_{1u}
78	98% a_{2u};
77	32% O π; 36% d_{yz}; 31% eg
76	52% eg; 40% d_{xz}; 5% O π
75	70% imid π; 28% eg
74	64% a_{2u}; 11% O π; 15% O σ; 3% d_x^2-y^2
73	72% b_{1u}; 26% imid π; 1% d_x^2-y^2
72	44% a_{2u}; 25% O π; 24% O σ; 2% d_z^2; 1% d_{xz}
71	87% d_x^2-y^2 ; 8% porphy; 7% O π; 4% O σ
70	84% eg; 8% d_{yz}; 5% O π
69	96% eg; 4% d_{yz}
68	90% eg; 4% d_{yz}; 6% d_{xz}
67	37% d_{xz}; 36% eg; 11% O σ; 15% imid π

Table 4.4. Excited State Transition for a Standard Peroxy Structure: Fe-O1 = 1.90 A; O-O = 2.45 A (Assigments Are Given to These Transitions Whose Transition Energies Are Lower Than the Soret Band).

Transition Energy (cm-1)	Transition Oscillator strength	Major Components	
6311.8	0.0000	d_{xz} -> d_{yz}; Oπ (0.80)	
7040.8	0.0000	d_x^2-y^2 -> d_{yz}; Oπ (0.87)	
7983.7	0.0296	Oπ -> eg* (0.71)	
8244.9	0.0021	Oπ (0.44); d_z^2 (0.36) -> eg*	
10390.8	0.0202	Oπ; a_{1u} -> eg*	
10904.8	0.0051	Oπ; a_{1u} -> eg*	
11455.7	0.0013	Oπ -> eg*	
11580.4	0.0085	d_{yz} -> eg*; Oπ -> eg*	
11993.5	0.0037	Oπ -> eg*	
12605.2	0.0017	Oπ -> eg*	
16378.1	0.0656	a_{1u} -> eg* (0.46); a_{2u} -> eg* (0.41)	Q
16583.3	0.0501	a_{1u} -> eg* (0.42); a_{1u} -> eg* (0.44)	Q
19704.2	0.0045	a_{1u} -> imid π*	
20909.1	0.0021	Oπ -> imid π* (0.57); d_{yz} -> imid π* (0.36)	
21521.0	0.0030	Oπ (0.51); a_{1u} (0.40) -> b_{2u}	
22728.6	0.0029	Oπ -> imid π*	
23648.4	0.0158	d_{xz} -> eg*	
24171.5	0.0024	Oπ (0.32); a_{1u} (0.29) -> b_{2u}; d_{xz} -> eg* (0.20)	
24323.8	0.0139	a_{2u} -> b_{2u} (0.18); Oπ (0.17), a_{1u} (0.08)-> d_{yz}; d_{xz} (0.10) -> eg*; ...	
24486.6	0.0110	d_{xz} -> eg*	
24580.1	0.0092	a_{2u} -> b_{2u}	
24818.7	0.0731	a_{2u} -> imid π	
25199.7	0.0059	a_{2u} -> imid π	
25570.7	0.0017	Oπ -> b_{2u}	
25948.3	0.0562	Oπ -> b_{2u} (14); d_{xz} -> eg* (0.38); ...	
26481.9	0.0037	Oπ -> b_{2u}	
26596.0	0.0829	Oπ -> imid π, σ	
26978.2	0.1168	a_{2u} (0.28) -> eg*; a_{1u} (0.28) -> eg*; ...	
27100.8	1.3006	a_{2u} (0.27) -> eg*; a_{1u} (0.19) -> eg*; ...	Soret
27797.2	0.9048		

27873.2	0.2194
28074.2	0.0042
28175.2	0.2237
28320.1	0.0661
28872.4	0.0019
28930.7	0.0611
29246.9	0.1591
29307.8	0.0099
29490.5	0.0433
29944.5	0.0439
29963.1	0.0106
30139.7	0.0571
30296.7	0.0103
30488.8	0.0206
30654.7	0.0126
30772.7	0.0159
31324.8	0.0134
31503.0	0.0044

Table 4.5. Excited State Transition for a Standard Peroxy structure: Fe-O1 = 2.1 A; O-O = 2.45 A (Assigments Are Given to These Transitions Whose Transition Energies Are Lower Than the Soret Band).

Transition Energy (cm^{-1})	Transition Oscillator strength	Major Components	
3598.8	0.0001	Oπ -> eg* (0.48); d_{yz} (0.47)	
5231.5	0.0001	d_{xz} (0.60); $d_{x^2-y^2}$ (0.29) -> d_{yz}	
5802.4	0.0221	Oπ -> eg*	
5937.1	0.0043	$d_{x^2-y^2}$ (0.51); d_{xz} (0.22);); ->d_{yz}	
7037.6	0.0006		
7673.8	0.0002		
8538.5	0.0013	Oπ -> eg* (0.87)	
8661.3	0.0003	Oπ -> eg* (0.84)	
9209.1	0.0106	Oπ -> eg* (0.72)	
9692.5	0.0058	Oπ -> eg* (0.68)	
10012.9	0.0024	a_{1u} (0.62); Oπ (0.23)-> eg*	
11584.5	0.0004		
13011.8	0.0001		
14605.7	0.0001		
15885.5	0.0009		
16133.2	0.0720	a_{1u} (0.40); a_{2u} (0.55)-> eg*	Q
16353.0	0.0596	a_{1u} (0.42); a_{2u} (0.55)-> eg*	Q
17059.2	0.0003		
17328.2	0.0000		
18104.3	0.0012	Oπ -> imid π* (0.90)	
19293.4	0.0010	Oπ -> imid π* (0.73)	
19781.1	0.0001		
21371.8	0.0053	a_{1u} -> b_{2u}* (0.72)	
21502.9	0.0035	a_{1u} -> b_{2u}* (0.95)	
21957.0	0.0009		
22248.7	0.0000		
22462.2	0.0030	Oπ -> b_{2u}*(0.87)	
22490.0	0.0065	Oπ -> b_{2u}*(0.81)	
22872.6	0.0000		
23361.8	0.0090	Oπ (0.67); d_{z^2} (0.23) -> imid σ*	
23559.6	0.0179	Oπ -> b_{2u}* (0.61)	

23949.0	0.0009	
24144.3	0.0018	d_{xz} -> eg* (0.34); Oπ -> imid σ* (0.39)
24355.2	0.0720	a_{2u} -> imid π* (0.75)
24605.4	0.0091	d_{xz} -> eg* (0.61)
24650.4	0.0046	Oπ -> imid π* (0.81)
24718.6	0.0117	a_{2u} -> imid π* (0.77)
24902.7	0.0112	a_{2u} -> b_{2u}*(0.41); d_{xz} ; eg -> eg* (0.27)
25313.5	0.0175	a_{2u} -> b_{2u}*(0.27); d_{xz} ; eg -> eg* (0.35)
25734.4	0.0038	
25775.7	0.0002	
26139.5	0.0251	d_{xz} -> eg* (0.56)
26821.2	0.0138	Oπ -> imid π* (0.86)
26993.0	1.1623	a_{1u} (0.22); a_{2u} (0.28)-> eg* Soret
27134.7	0.2952	
27414.2	0.1544	
27601.7	0.0682	
27665.4	0.5357	
28059.6	0.9829	
28679.5	0.0062	
29079.6	0.0100	
29232.2	0.0637	
29315.1	0.0015	
30055.9	0.0008	
30222.8	0.0315	
30259.3	0.0422	
31028.3	0.0287	
31167.8	0.0115	
31445.4	0.0026	

Table 4.6. Ground State Orbital Description of an Isomer of the Peroxy Complex, Hydroperoxy-1. A Proton Has Been Shifted from Imidazole Ring to the Terminal Oxygen

Orbital #	Orbital Occupancies Fe-O1 = 1.90 Å
90	98% imid π^*
89	99% a_{1u}^*
88	98% eg^*
87	99% eg^*
86	60% d_{z^2}, 17% porphy σ; 10% porphy π; 10% imid σ^*
85	55% d_{xy}; 25% porphy σ^*;17% porphy π^*
84	85% b_{2u};14% d_{xy}
83	100% b_{1u}^*
82	97% eg^*; 1% d_{xz}
81	99% eg^*
80	94% d_{yz}; 3% O π
79	99% a_{1u}
78	94% imid π
77	97% a_{2u}
76	32% imid π; 26% imid σ; 17% d_{xz}; 16% porphy π
75	55% eg; 20% d_{xz}; 14% imid π; 9% imid σ
74	58% imid π; 23% imid σ; 10% porphy π; 5% d_{xz}
73	75% eg; 17% O π; 2% imid π
72	98% b_{1u}
71	92% a_{2u}; 6% imid σ
70	80% $d_{x^2-y^2}$; 12% porphy π; 5% imid σ
69	95% eg; 2% O π
68	98% eg;
67	62% O π; 26% porphy π; 5% d_{xz}; 3% d_{yz}

Table 4.7. Ground State Orbital Description of a Protonated Peroxy Complex, Hydroperoxy-2. A Proton Has Been added to the Terminal Oxygen

Orbital #	Orbital Occupancies Fe-O1 = 1.90 A^{o}
90	98% eg*
89	99% a_{1u}*
88	50% d_{z^2}; 28% porphy π; 16% imid σ*; 2% d_{xy}
87	62% d_{xy}; 32% porphy σ
86	98% imid π*
85	89% imid σ*; 9% imid π*; 2% d_{z^2}
84	99% b_{2u}
83	98% imid π*
82	96% eg*
81	98% eg*
80	94% d_{yz}; 4% O π
79	99% a_{1u}
78	98% a_{2u}
77	72% eg; 27% d_{xz}
76	58% imid π; 40% eg
75	96% eg
74	98% a_{2u}
73	60% b_{1u}; 39% imid π
72	98% eg;
71	96% eg; 1% $d_{x^2-y^2}$;
70	80% $d_{x^2-y^2}$; 16% porphy π
69	95% eg; 2% O π
68	98% eg;
67	58% O π; 30% porphy π; 4% d_{xz}; 2% d_{yz}

Table 4.8. Charge distribution on an isomer of the peroxy-heme complex, hydroperoxy-1. A proton has been shifted to the terminal oxygen from the imidozale ring: Fe-O-O angle equals to 110.8^{O}, O-O bond length equals to 1.45 A^{O}.

r (Fe-O) A^{O}	Q (Fe)	Q (O1)	Q(O2)	Q (Porphyrin)	Q (Imidazole)
1.5	1.322	-0.271	-0.235	-1.296	-0.751
1.6	1.299	-0.318	-0.237	-1.245	-0.734
1.7	1.272	-0.356	-0.241	-1.196	-0.716
1.8	1.245	-0.387	-0.247	-1.151	-0.698
1.9	1.219	-0.412	-0.254	-1.109	-0.682
2.0	1.195	-0.432	-0.260	-1.066	-0.669
2.1	1.175	-0.448	-0.266	-1.040	-0.658
2.2	1.158	-0.463	-0.271	-1.009	-0.651
2.3	1.145	-0.477	-0.275	-0.985	-0.643
2.4	1.136	-0.491	-0.279	-0.962	-0.638

Table 4.9. Charge distribution on a standard peroxy-heme structure: Fe-O-O angle equals to 110.8^{O}, Fe-O bond length equals to 1.90 A^{O}.

r (O-O) A^{O}	Q (Fe)	Q (O1)	Q(O2)	Q (Porphyrin)	Q (Imidazole)
1.1	1.009	-0.150	-0.078	-1.942	0.111
1.2	0.991	-0.146	-0.345	-1.563	0.063
1.3	1.003	-0.191	-0.362	-1.517	0.067
1.4	1.060	-0.225	-0.513	-1.402	0.080
1.45	1.184	-0.314	-0.724	-1.234	0.088
1.5	1.197	-0.338	-0.744	-1.214	0.099
1.6	1.211	-0.375	-0.764	-1.176	0.104
1.7	1.219	-0.407	-0.766	-1.153	0.107
1.8	1.222	-0.437	-0.755	-1.141	0.111
2.0	1.220	-0.495	-0.707	-1.131	0.113

Table 4.10. Charge distribution on an isomer of the standard peroxy-heme complex, hydroperoxy-1. A proton has been shifted to the terminal oxygen from the imidozale ring: Fe-O-O angle equals to 110.8^{O}, Fe-O bond length equals to 1.90 A^{O}.

r (O-O) A^{O}	Q (Fe)	Q (O1)	Q(O2)	Q (Porphyrin)	Q (Imidazole)
1.1	1.169	-0.333	-0.150	-1.196	-0.697
1.3	1.210	-0.400	-0.223	-1.133	-0.683
1.45	1.219	-0.412	-0.254	-1.112	-0.679
1.6	1.222	-0.410	-0.279	-1.097	-0.677
1.8	1.223	-0.394	-0.319	-1.077	-0.672
2.0	1.226	-0.371	-0.374	-1.048	-0.664

Table 4.11. Charge distribution on hydroperoxy-heme complex, a proton has been added to the terminal oxygen from the imidozale ring: Fe-O-O angle equals to 110.8^{O}, Fe-O bond length equals to 1.90 A^{O}.

r (O-O) A^{O}	Q (Fe)	Q (O1)	Q(O2)	Q (Porphyrin)	Q (Imidazole)
1.1	1.160	-0.259	-0.107	-1.366	-0.653
1.3	1.237	-0.364	-0.217	-1.256	-0.641
1.45	1.250	-0.383	-0.250	-1.225	-0.640
1.6	1.255	-0.385	-0.274	-1.210	-0.636
1.8	1.257	-0.374	-0.308	-1.188	-0.636
2.0	1.258	-0.355	-0.352	-1.161	-0.632

Table 4.12. Charge distribution on the standard peroxy-heme complex, dioxygen are rotated above the porphyrin plane: O-O bond eclipses the x-axis at $\theta = 0^{O}$, Fe-O-O angle equals to 110.8^{O}, Fe-O bond length equals to 1.90 A^{O}.

θ (degree)	Q (Fe)	Q (O1)	Q(O2)
0	1.184	-0.314	-0.724
15	1.186	-0.315	-0.724
30	1.186	-0.317	-0.714
45	1.190	-0.319	-0.701
60	1.188	-0.319	-0.710
75	1.186	-0.318	-0.726
90	1.185	-0.317	-0.730

Figure 4.6 Computed electronic spectrum of the hydroperoxy-1 species: Fe-O =1.9 A^{O}, O-O = 1.45 A^{O}.

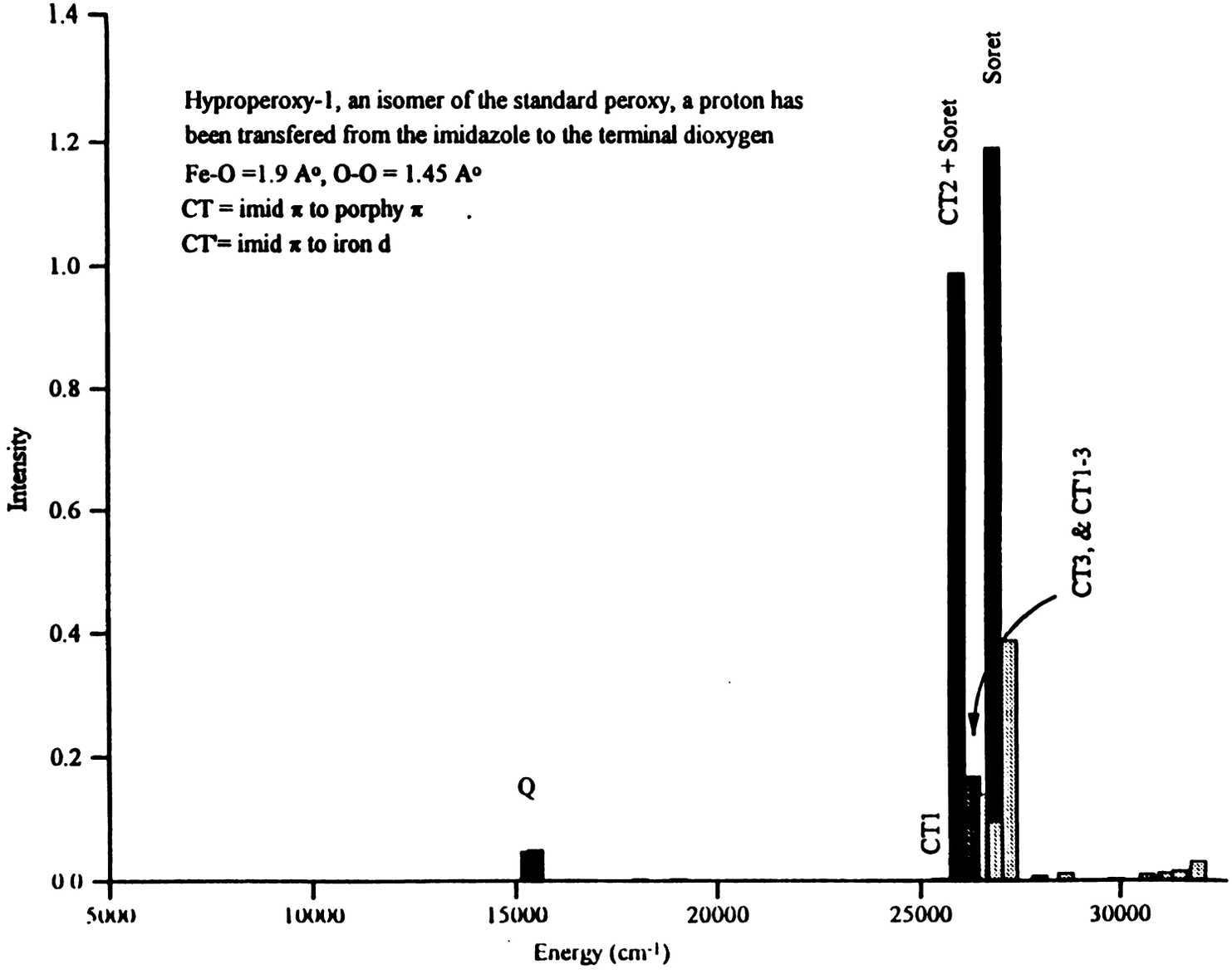
Hyproperoxy-1, an isomer of the standard peroxy, a proton has been transfered from the imidazole to the terminal dioxygen
Fe-O =1.9 A°, O-O = 1.45 A°
CT = imid π to porphy π
CT= imid π to iron d
Intensity
1.4
1.2
1.0
0.8
0.6
0.4
0.2
0 0
Q
CT1
CT2 + Soret
Soret
CT3, & CT1-3
5000
10000
15000
20000
25000
30000
Energy (cm-1)

Figure 4.7 Computed electronic spectrum of the hydroperoxy-2 species: Fe-O =1.9 A^{O}, O-O = 1.45 A^{O}.

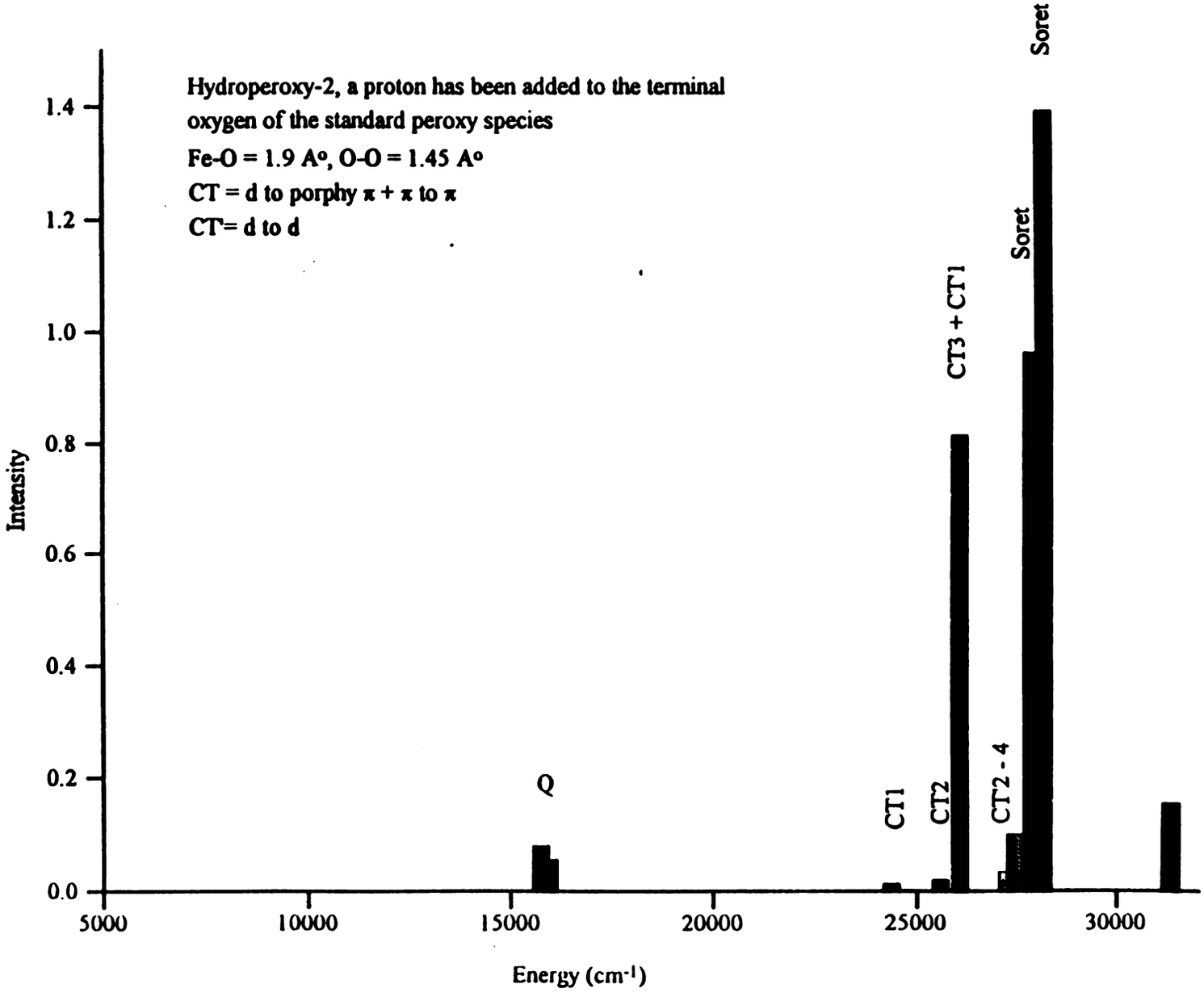
Hydroperoxy-2, a proton has been added to the terminal oxygen of the standard peroxy species
Fe-O = 1.9 A°, O-O = 1.45 A°
CT = d to porphy π + π to π
CT= d to d
Soret
CT3 + CT1
Soret
Q
CT1
CT2
CT2 - 4
Intensity
0.0
0.2
0.4
0.6
0.8
1.0
1.2
1.4
5000
10000
15000
20000
25000
30000
Energy (cm-1)

Figure 4.8 The correlations of net charge distribution at iron, end-on oxygen and terminal oxygen vs. the O-O distance. Fe-O-O angle equals to 110.8^{o}, Fe-O bond length equals to 1.90 A^{o}.

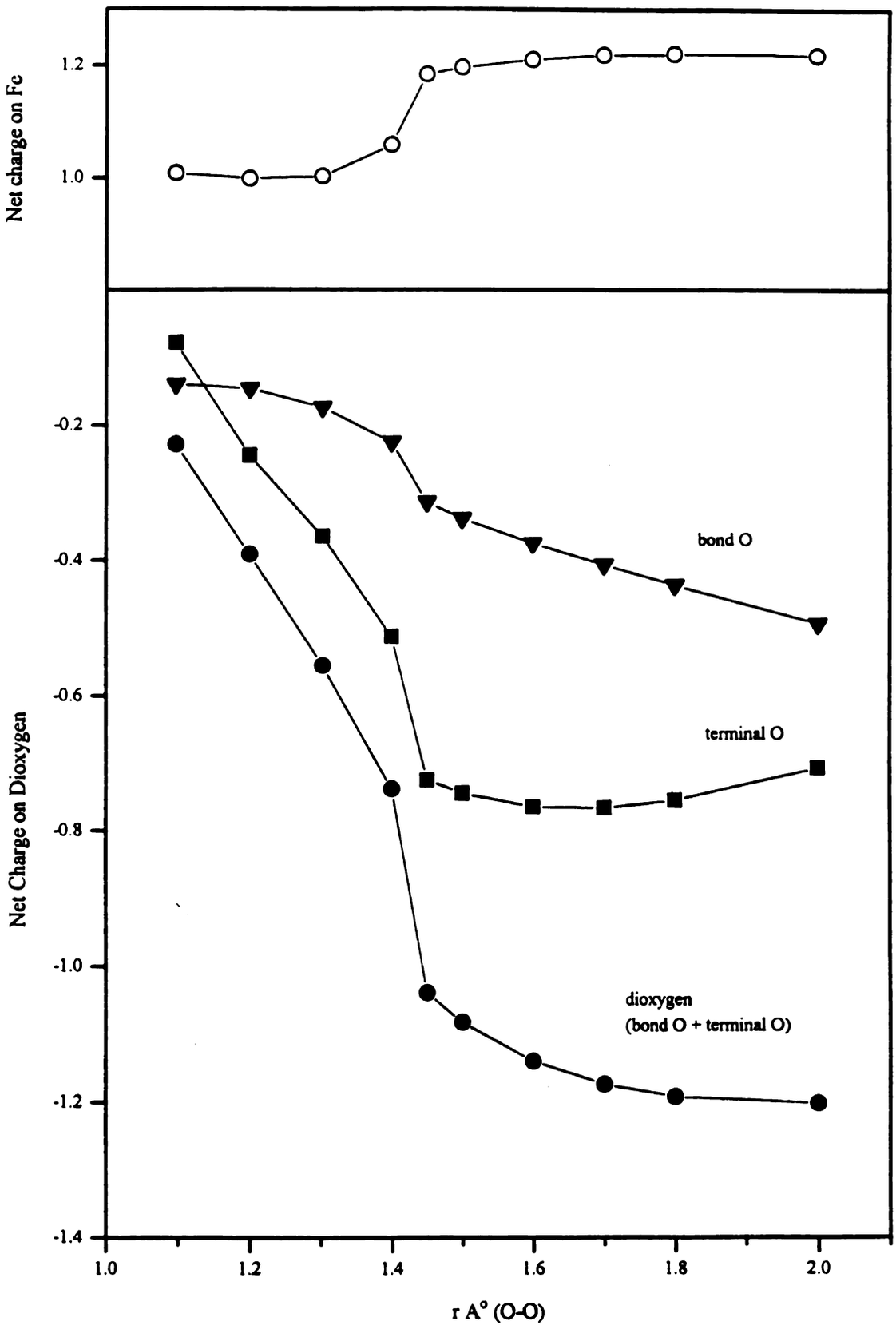
Net charge on Fe
1.2
1.0
Net Charge on Dioxygen
-0.2
-0.4
-0.6
-0.8
-1.0
-1.2
-1.4
bond O
terminal O
dioxygen
(bond O + terminal O)
1.0
1.2
1.4
1.6
1.8
2.0
r A° (O-O)

Figure 4.9 The 3-D view of the computed electronic spectra of the hydroperoxy-1 species at different O-O distances.

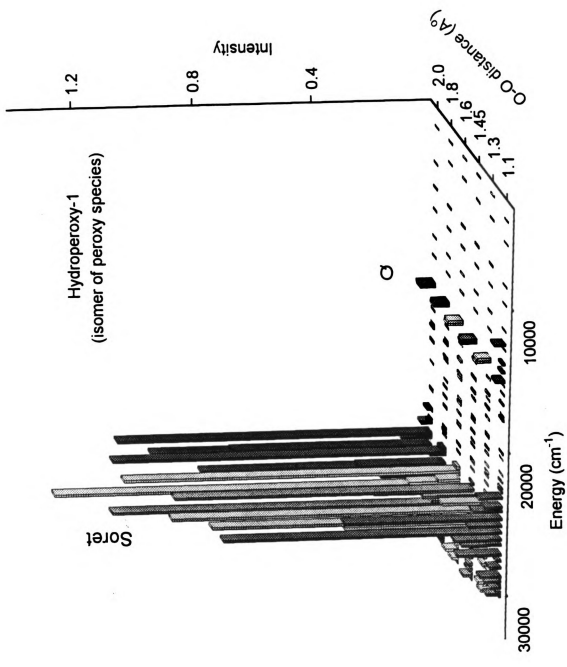
Hydroperoxy-1
(isomer of peroxy species)
Intensity
1.2
0.8
0.4
O-O distance (Å)
2.0
1.8
1.6
1.45
1.3
1.1
Soret
σ
30000
20000
10000
Energy (cm-1)

Figure 4.10 The 3-D view of the computed electronic spectra of the hydroperoxy-2 species at different O-O distances.

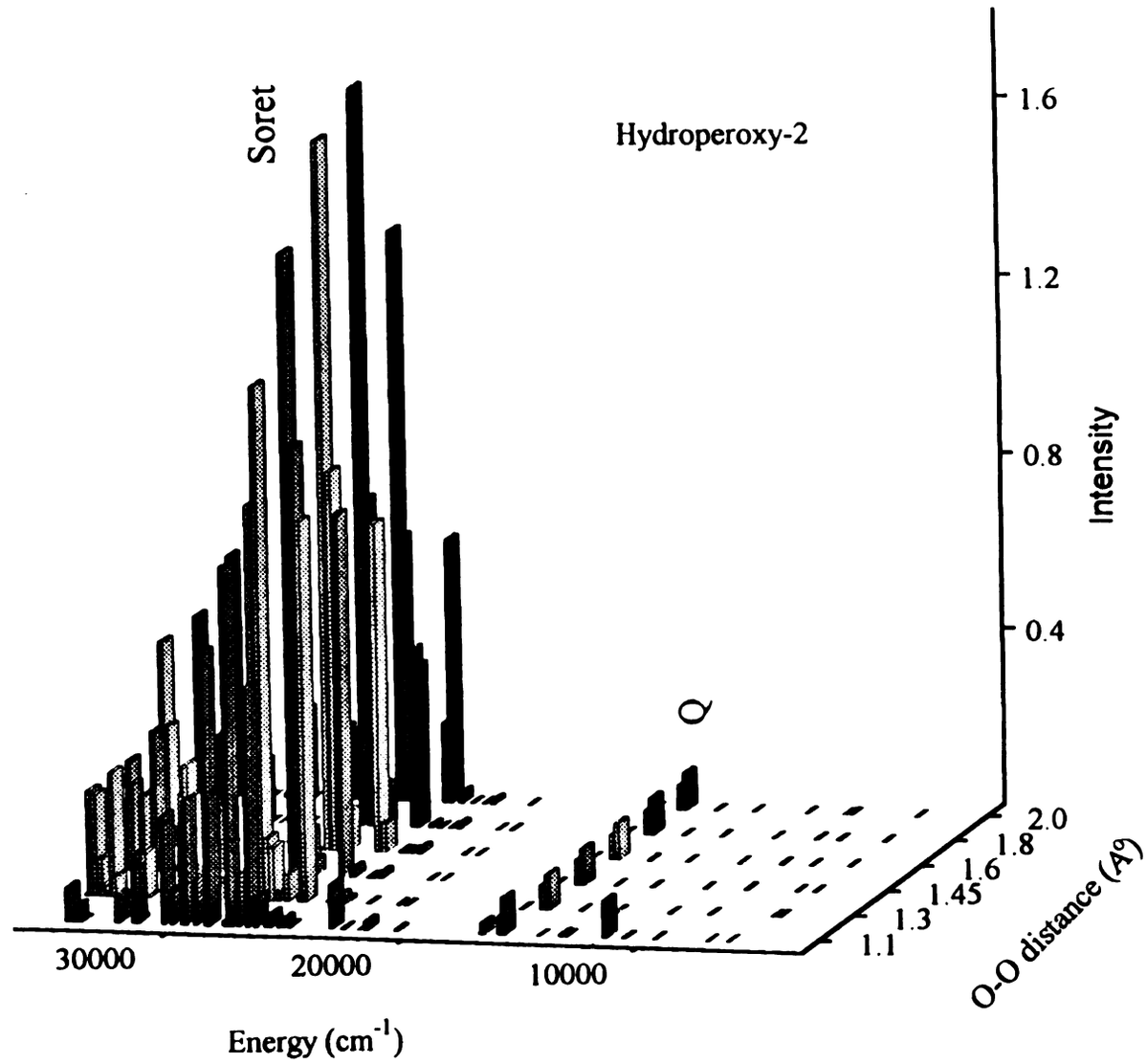
Soret
Hydroperoxy-2
Q
1.6
1.2
0.8
0.4
Intensity
2.0
1.8
1.6
1.45
1.3
1.1
O-O distance (A°)
30000
20000
10000
Energy (cm-1)

Figure 4.11 The 3-D view of the computed electronic spectra of the hydroperoxy-1 species at different Fe-O distances.

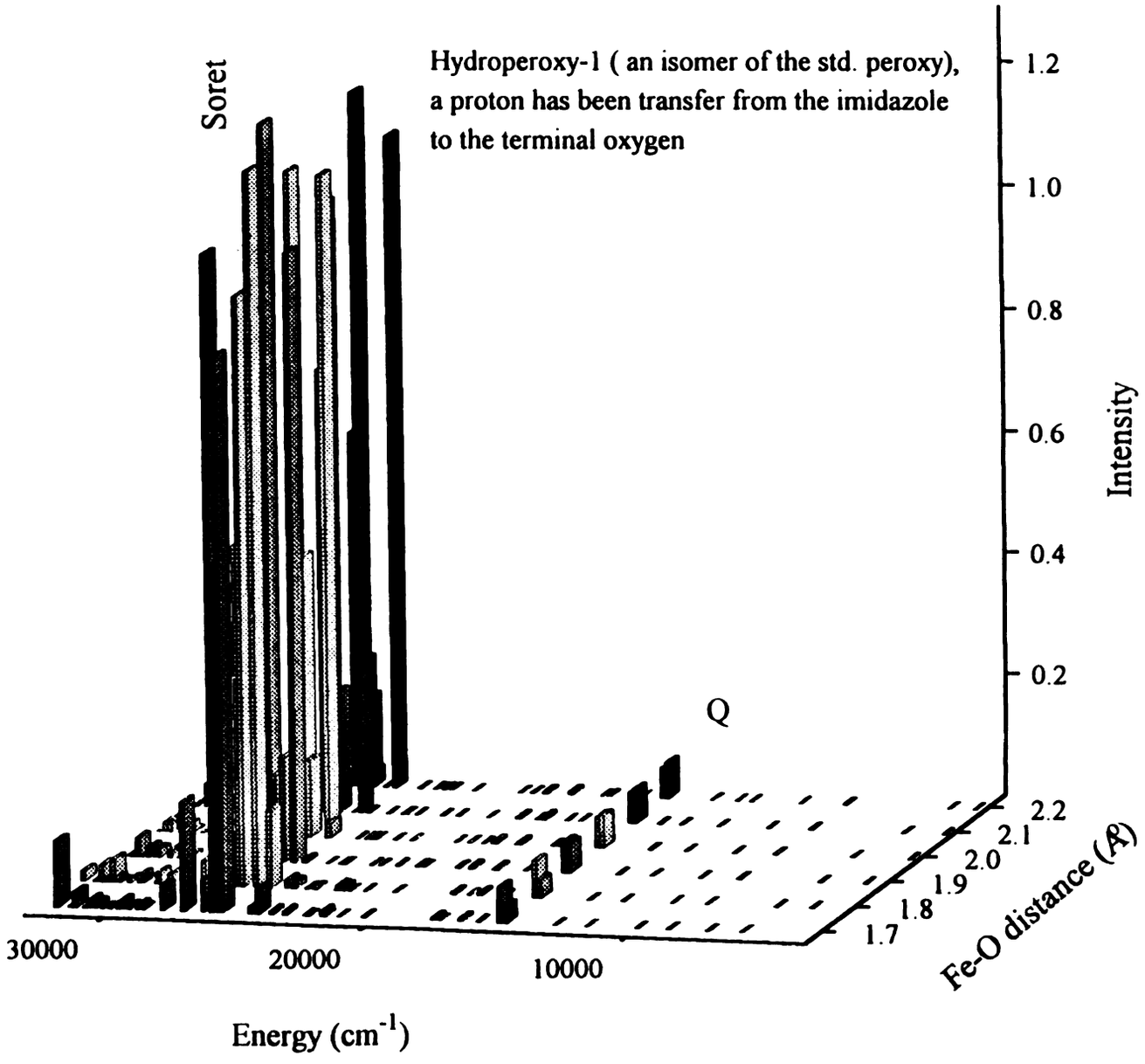
Hydroperoxy-1 (an isomer of the std. peroxy),
a proton has been transfer from the imidazole
to the terminal oxygen
Soret
Q
1.2
1.0
0.8
0.6
0.4
0.2
Intensity
2.2
2.1
2.0
1.9
1.8
1.7
Fe-O distance (Å)
30000
20000
10000
Energy (cm-1)

Figure 4.12 The variation of the empirical paraterized INDO-SCF energies as a function of the Fe-O torsion angle.

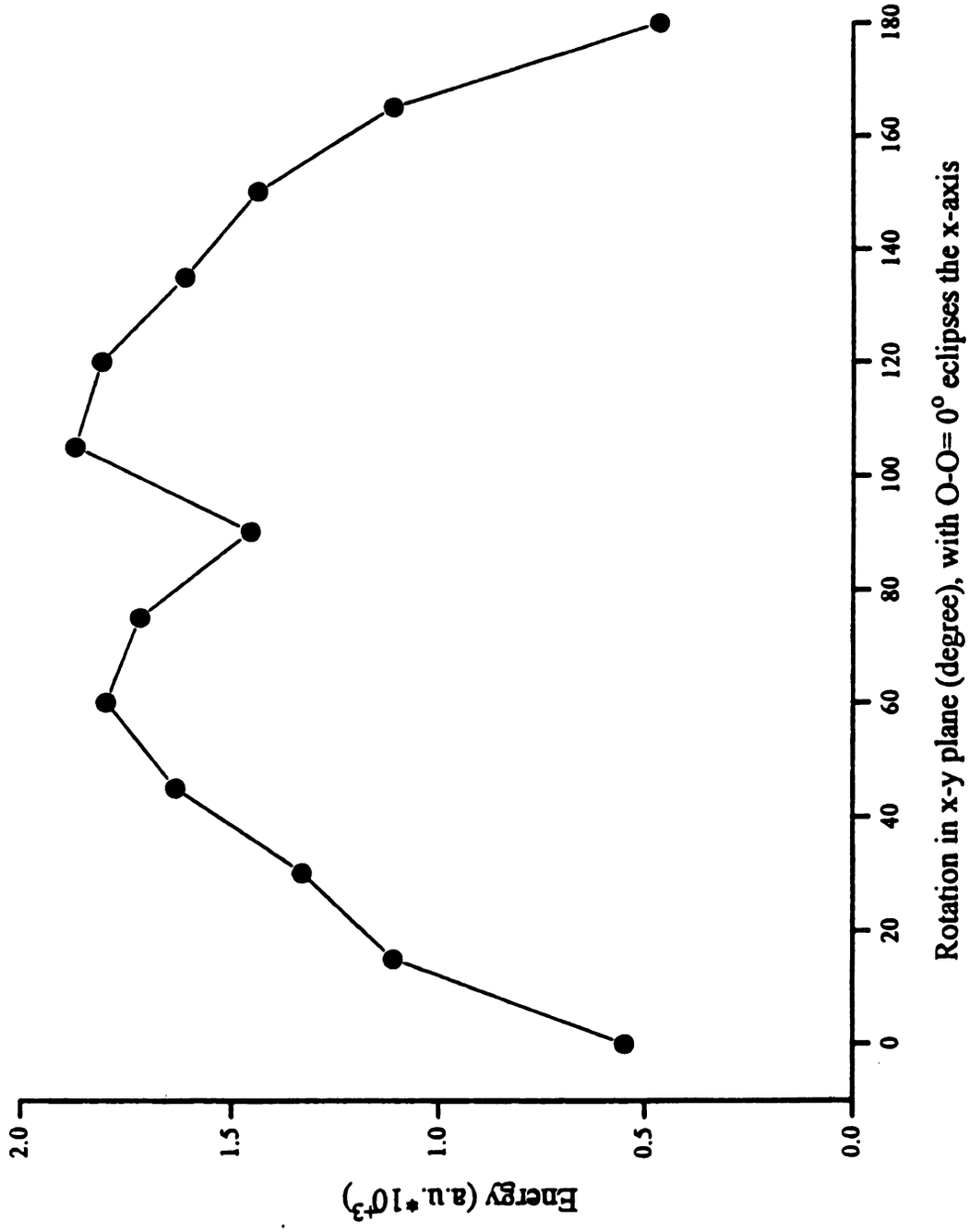
Energy (a.u.*10^-3)
2.0
1.5
1.0
0.5
0.0
0
20
40
60
80
100
120
140
160
180
Rotation in x-y plane (degree), with O-O= 0° eclipses the x-axis

The variation of the empirically parameterized INDO-SCF energies as a function of the Fe-O torsion angle is shown in Figure 4.12. Similar to the dioxygen binding to the heme complex [11], energy minima of the peroxy species occur at 0 °, 90 ° and 180 °, corresponding to the peroxy species eclipsing and staggering the x-axis. The local minimum at 90 ° is, however, higher in energy than those at 0 ° and 180 °, probably due to rectangular type Jahn-Teller distortion on the porphyrin macrocycle [72]. Similar behavior was also observed for the side-on peroxy adduct of a manganoporphyrin [63]. On the other hand, the peroxy species is rotationally less hindered about the porphyrin plane than the oxy-heme complex, as the rotational barrier (~ 2 kcal/mol) of the peroxy is smaller than that of the dioxygen adduct (~ 7 kcal/mol) [11]. This, in turn, can be explained by the longer Fe-O and O-O bonds in the peroxy forms.

4.4 Discussion

The analysis of the electronic transitions of these possible peroxy intermediates shows that both Soret and Q bands are very stable in energy. They are not affected to a great extent by the peroxy-heme geometry, nor by the difference in binding species, i.e., the standard peroxy, its isomeric hydroperoxy-1, and proton-added hydroperoxy-2. However, the oxygen to porphyrin ring charge-transfer transitions caused by the added electron density located on oxygens in the peroxy conformation in the standard peroxy species are eliminated from the hydroperoxy-1 and the hydroperoxy-2. The hydroperoxy-1, which has the same negative charge as the peroxy form, lacks oxygen to porphyrin charge transfer transitions because the negative charge is neutralized by the proton shifted from the imidazole ring. This species has imidazole to porphyrin and imidazole to iron charge transfer states, as expected for a negative imidazole ligand. However, most of these transitions that carry oscillator strength lie higher than the Soret bands, see Figure [6]. The high-lying CT channels are less peroxy-

photodissociable because of their higher energy levels and because of the lack of mixing of the imidazolate orbitals with those involved in the heme-peroxy binding mechanism. These excited states, however, may influence electron delocalization to the porphyrin periphery and the iron center because they strongly mix into the Soret transitions. They may also take part in oxygen reduction by fully reduced cytochrome oxidase by facilitating the formation of non-photolabile products at later stages in the reaction.

In the standard peroxy species, the lower photodissociating channel, which consists of a manifold of charge-transfer states, is accessible either by direct excitation or decay from the higher energy $\pi-\pi^*$ singlet states that give rise to the Q and Soret bands. As pointed out early, dissociation of the peroxy from the heme plane would not contribute to the non-photolabile products in oxygen reaction with the cytochrome oxidase. Since the formation of end-on peroxy-heme is a natural extension of end-on dioxygen-heme species, the transition from the oxy to the standard peroxy can be considered as a relaxation process after the injection of an electron to the heme a_3 reactive site. This conformation further discriminates the two oxygen atoms by their charge distribution, and hence, their redox ability. This is probably the key to the enzyme catalyzed oxygen reduction [1, 34]. Considering the overlap of iron d_{yz} orbital with the oxygen p_y orbital in the bent end-on peroxy structure, this uneven configuration makes the bound oxygen orbitals overlap more strongly the iron d orbitals than those on the terminal oxygen. As the terminal oxygen accumulates more net negative charge than the bound oxygen, it is more susceptible to attack by a proton to form the hydroperoxy intermediate. The presence and the nature of the distal Cu_B, which is on the same side of the porphyrin plane as the bound dioxygen, is also expected to play a role in the geometry of the dioxygen-heme binding. On the other hand, the transient species with the standard peroxy conformation is very reactive and, therefore, short-lived. A proton transfer or the ligation of Cu_B cluster to the terminal

oxygen is necessary in order to trap this end-on binding structure. Otherwise, we speculated that this intermediate will transform to a side-on conformation to equalize the electronic configuration on two oxygen atoms. As iron porphyrin itself could not distinguish two oxygen atoms, the protein local environment may be at the origin of modifications of the electronic configurations of the oxygen atoms and therefore, the dioxygen-heme binding geometry. For example, a model of mutant and wild-type carbon monoxy cytochrome oxidase has suggested that three histidine residues, His284, -333, and -334 are ligated to the Cu_B center [29]. One of these residues may serve as the proton donor or form a hydrogen bonding to the peroxy type dioxygen-heme complex under certain conditions, especially low pH.

As it can be seen from Table 4.4 and 4.5, both the Soret and Q transitions are mainly x-y polarized. Although Fe-O stretch is z-polarized in character, resonance Raman was, however, able to detect this vibrational mode by exciting at Soret region. The bent dioxygen-heme binding geometry may explain this experimental result. The coupling of the oxygen $p\pi$ orbitals to the iron d_{xz} and d_{yz} orbitals mixes the porphyrin x-y polarized π–π^* transitions into the z-polarized transition of the Fe-O- bond, the interaction of the $O\pi$ (p_y) orbitals with the π orbitals on the porphyrin periphery may also contribute to this phenomenon. The existence of $O\pi$ to porphyrin π transitions in the oxy-heme dioxygen adduct supports this hypothesis [10-11]. In the peroxy case, the weak coupling of the O-O π to the Fe-O π is expected because the dioxygen anti-bonding orbitals are occupied by an additional electron. Its Fe-O-O angle (110.8°) is larger than that of the oxy adduct, which renders the O π to porphyrin π transitions weaker [see Figure 10]. On the other hand, even weaker coupling of the O-O π to the Fe-O π is expected in the protonated terminal oxygen forms, the hydroperoxy-1 and the hydroperoxy-2, because of the lack of the strong $O\pi$ to porphyrin π transitions in these species. This may explain the observation that the detection of the Fe-O

stretching mode by vibrational methods is more difficult in the peroxy species than that in oxy species.

Traditionally, the peroxy species is constructed as two negative charges localized on the oxygen atoms. This is probably true in many inorganic peroxy complexes because the ligands coordinated to the metal centers are incapable of delocalizing excessive electrons. However, our calculations indicate that the porphyrin resonance ring structure, especially its pyrrole nitrogen atoms, is a strong contender with the bound oxygen atom for delocalizing the electron density in the peroxy species. Our results show that there is no need to have a true peroxy species, Fe(III)-O^--O^-, as an intermediate in the dioxygen reduction cycles. Since the dissociation of the peroxy species is fatal to the physiological function of the enzyme, this reaction would not be, therefore, a favorable process in Nature. The extra electrons introduced during the dioxygen-enzyme reactions can be delocalized on the porphyrin macrocycle to form a superoxo-like species. This superoxo-like conformation has a stronger Fe-O bond and is, therefore, less dissociable than is the standard peroxy form. A proton transfer reaction will convert this species into an even more stable protonated form, hydroperoxy-1. As the iron is in a mixed valence configuration, the Fe-O stretching mode is somewhat different from the standard peroxy species. The Fe-O- bond in the superoxo-like peroxy is more polarized and slightly longer than the Fe(II)-O- bond in the oxy species, but less polarized than the conventional Fe(III)-O^-- bond. Both the oxy-heme species and the superoxo-like peroxy species are expected to have iron d to oxygen π^* backbounding. Since the superoxo-like peroxy species have smaller perturbation from the oxy species than that expected for the standard peroxy conformation, the vibrational mode of this species is expected to be close to the oxy species, around 570 cm^{-1}. Although there is no resonance Raman experiment to confirm this prediction, a likely explanation is that, according to the kinetic scheme (Figure 1b), the possible overlap of the oxy and the

peroxy species at the same time domain and their similarity in vibrational properties are expected to complicate the observation of the peroxy species in this region. Another possibility is that the existence and the fast converting of oxy, peroxy, hydroperoxy-1 and -2 intermediates couple their charge-transfer bands so that the transient absorption spectra near the Soret region are also mixtures of the above species. Resonance Raman spectroscopy, therefore, can not effectively distinguish them in this excitation region.

4.5 Conclusion

In this work, INDO calculations have been performed to study the peroxy-heme complex and its protonated terminal oxygen forms, i.e., hydroperoxy-1 and hydroperoxy-2 [Figure 3]. The electron density distribution and the excited electronic state properties as functions of several geometrical conformations and parameters, have been analyzed in terms of the iron d, porphyrin π and oxygen π^* orbital interactions. The analysis of the electron density distribution reveals that in the end-on dioxygen geometry negative charge is mainly distributed on the terminal oxygen and porphyrin macrocycle and iron is basically in an intermediate valence configuration. The effect of the molecular surrounding was considered. In particular, the charge-transfer transitions that account for the extra features to the red of the Q bands were found for the bent end-on peroxy species. These CT transitions have calculated oscillator strengths higher than those of the standard oxy-heme complexes [10]. Since these CT bands lie about or lower than that of Q bands, excitation in the red region should give appreciable photodissocation signal of the peroxy species. Time-resolved resonance Raman results on oxygen reduction catalyzed by cytochrome oxidase also indicated that this species is photodissociable [11]. In order to stabilize this intermediate, a proton is required for addition to the terminal oxygen. As expected, these low-lying CT bands are extinguished in the protonated peroxy forms. The end-

on dioxygen structure favors the accumulation of negative charge at the terminal oxygen. Thus, a mechanism that involves heterogeneous cleavage of the oxygen-oxygen bond is preferred, rather than the simple dissociation of the peroxy from the heme moiety. The CT transitions with calculated oscillator strengths intermediate between those calculated for the Q and Soret bands are found for all three model intermediates. The character of the charge transfer is however, some what different in each complex. In the peroxy form, oxygen π is mixed into the porphyrin a_{1u} orbital and CT transitions are predominately from the oxygen π^* to the porphyrin π. In the hydroperoxy-1 isomer, both iron d orbitals and imidazole ring orbitals are involved in the CT to the porphyrin π orbitals. However, the majority of the CTs that carry oscillator strength are the imidazole to porphyrin transitions, which are equal or higher than the porphyrin Soret bands. There are few transitions between Q and Soret bands that are significant in intensity. In the hydroperoxy-2 intermediate, in addition to the porphyrin π–π transitions, CTs are from iron d orbitals to the porphyrin macrocycle but with an extensive coupling of the CT from oxygen to the porphyrin π. Thus, the excitation between the Q bands and Soret bands is most likely to be useful in monitoring the protonated peroxy forms.

In conclusion, in spite of using INDO level calculations, the present results give new information about the electronic and geometrical conformation of possible peroxy intermediates in heme enzymes. Further experiments have been suggested in order to test these computational predictions. If they could be experimentally confirmed in the oxygen reaction with cytochrome oxidase, these calculations would be powerful ways to probe the nature of oxygen binding site in the protein environments.

4.6 Acknowledgment

We thank Prof. M. Zerner for kindly providing us his ZINDO programs and Dr. Bendale for helpful discussion on implements of above computational package. Support is acknowledged from grant GM 25480 (to G.T.B.) of the U.S. National Institute of Health.

References

1. G. T. Babcock and M. Wikstrom, *Nature* **1992**, *356*, 301.

2. B. G. Malmstrom, *Acc. Chem. Res.* **1993**, *26*, 332.

3. S. I. Chan and P. M. Li, *Biochem.* **1990**, *29*, 1.

4. A minireview series devoted to cytochrome oxidase: *J. Bioenerg. Biomember.* **1993**, *25*, 69-188.

5. For review see *Cytochrome P-450, Structure, Mechanism, and Biochemistry* P. R. Ortiz de Montellano *eds.*, Plenum Press, New York and London, **1986.**

6. B. Shaanan, *Nature*, **1982**, *296*, 683.

7. S.E.V. Phillips and B. P. Schoenborn, *Nature*, **1981**, *292*, 81.

8. For review see M. Momenteau and C. A. Reed, *Chem. Rev.* **1994**, *94*, 659.

9. For review see I. Bytheway and M. B. Hall, *Chem. Rev.* **1994**, *94*, 639.

10. A. Waleh and Gilda Loew, *J. Am. Chem. Soc.* **1982**, *104*, 2352.

11. Z. S. Herman and G. H. Loew, *J. Am. Chem. Soc.* **1980**, *102*, 1815.

12. P. Du, F. U. Axe, G. H. Loew, S. Canuto and M. C. Zerner, *J. Am. Chem. Soc.* **1991**, *113*, 8614.

13. A. Dedieu, M.M. Rohmer and A. Veillard, *Adv. Quantum Chem.* **1982**, *16*, 43.

14. S. Yamamoto and H. Kashiwagi, *Chem. Phys. Lett.* **1989**, *161*, 85.

15. J. E. Newton and M. B. Hall, *Inorg. Chem.* **1984**, *23*, 4627.

16. D. A. Case, B. H. Huynh and M. Karplus, *J. Am. Chem. Soc.* **1979**, *101*, 4433.

17. G. H. Loew, In *Iron Porphyrins: Part One*, A.B. P. Lever and H. B. Gray *eds.*, Addison-Wesley, **1983**, 1-87.

18. M. B. Hall, In *Oxygen Complexes and Oxygen Activation by Transition Metals*, A. E. Martell and D. T. Sawyer *eds.*, PLenum, New York, 1988, pp 3-16.

19. M. H. Gubelmann and A. F. Williams, *Struct. Bonding*, **1983**, *55*, 1.

20. J. Bertran, M. F. Ruiz-Lopez and D. Rinaldi, *J. Mol. Struct.* **1991**, *232*, 337.

21. W. A. Goddard III and B. D. Olafson, *Proc. Natl. Acad. Sci USA*, **1977**, *74*, 1315.

22. I. P. Gerothanassis and M. Momenteau, *J. Am. Chem. Soc.*, **1987**, *109*, 6944.

23. J. P. Collman, J. I. Brauman, T. R. Hallbert and K. S. Suslick, *Proc. Natl. Acad. Sci. USA*, **1976**, *74*, 3333.

24. Q. Gibson and C. Greenwood, *Biochem. J.* **1963**, *86*, 541.

25. C. Greenwood and Q. Gibson, *J. Biol. Chem.* **1967**, *242*, 1781.

26. R. S. Blackmore, C. Greenwood and Q. Gibson, *J. Biol. Chem.* **1991**, *266*, 19245.

27. G. T. Babcock, J. M. Jean, L. N. Johnston, G. Palmer and W. H. Woodruff, *J. Am. Chem. Soc.* **1984**, *106*, 8305.

28. G. T. Babcock, in *Biological Applications of Raman Spectroscopy* ed. T. G. Spiro, Wiley, **1988**.

29. G. T. Babcock, C. Varotsis and Y. Zhang, *Biochim. Biophy. Acta*, **1992**, *1101*, 192.

30. J. P. Hosler, et al *J. Am. Chem. Soc.* **1994**, *116*, 5515.

31. C. Varotsis and G. T. Babcock, *Biochem.* **1990**, *29*, 7357.

32. C. Varotsis, W. H. Woodruff and G. T. Babcock, *J. Am. Chem. Soc.* **1989**, *111*, 6439.

33. C. Varotsis, W. H. Woodruff and G. T. Babcock, *J. Am. Chem. Soc.* **1990**, *112*, 1297.

34. C. Varotsis, Y. Zhang, E. H. Appleman and G. T. Babcock, *Proc. Natl. Acad. Sci. USA*, **1993**, *90*, 237.

35. J. P. Hosler, et al *J. Bioener. Biomem.* **1993**, *25*, 121.

36. A. P. Hansen, R. D. Britt, M. P. Klein, C. J. Bender and G. T. Babcock, *Biochem.* **1993**, *32*, 13718.

37. G. T. Bacock, *Encyclopedia of Inorganic Chemistry*, R. H. Scott *ed.* Wiley, New York, inpress.

38. G. T. Babcock, C. Varotsis, and Y. Zhang, *Biochim. Biophys. Acta* **1993**, *1101*, 192.

39. G. T. Bacock and C. Varotsis, *SPIE* vol. 1890, *Biomolecular Spectroscopy*, **1993.**

40. T. Ogura, S. Takahashi, S. Hirota, K. Shinzawa-Itoh, S. Yoshikawa, and T. Kitagawa, *J. Am. Chem. Soc* **1990**, *112*, 5630.

41. T. Ogura, S. Takahashi, S. Hirota, K. Shinzawa-Itoh, S. Yoshikawa, E. H. Appleman and T. Kitagawa, *J. Am.Chem. Soc.* **1993**, *115*, 8527.

42. S. Han, Y.-C. Ching and D. L. Rousseau, *Proc. Natl. Acad. Sci. USA* **1990**, *87*, 89.

43. S. Han, Y.-C. Ching and D. L. Rousseau, *Nature* **1990**, *348*, 89.

44. M. I. Verhovsky, J. E. Morgan and M. Wikstrom, *Biochem.* **1994**, *33*, 3079.

45. M. Oliveberg and B. G. Malmstrom, *Biochem.* **1992**, *31*, 3560.

46. B. C. Hill, *J. Biol. Chem.* **1991**, *266*, 2219.

47. B. C. Hill, *J. Bioenerg. Biomembr.* **1993**, *25*, 115.

48. O. Einarsdottir, *et al Biochem.* **1993**, *32*, 12013.

49. O. Einarsdottir, P. M. Killough, J. A. Fee and W. H. Woodruff, *J. Biol. Chem.* **1989**, *264*, 2405.

51. W. H. Woodruff, *et al, Proc. Natl Acad. Sci USA* **1991**, *88*, 2588.

52. P. O. Stoutland, R. B. Dyer and W. H. Woodruff, *Science* **1992**, *257*, 1913.

53. R. B. Dyer, K. A. Peterson, P. O. Stoutland and W. H. Woodruff, *Biochem.* **1994**, *33*, 500.

54. W. H. Woodruff, R. B. Dyer and O. Einarsdottir, in *Biological Spectroscopy* Part B, **1993**, R. J. H. Clark and R. E. Hester *eds.*, *John Wiley and Sons*, Chichester, England, pp. 189-233.

55. W. H. Woodruff, *J. Bioenerg. Biomember.* **1993**, *25*, 177.

56. W. Li and G. Palmer, *Biochem.* **1993**, *32*, 1833.

57. D. F. Blair, S. N. Witt and S. I. Chan, *J. Am. Chem. Soc.* **1985**, *107*, 7389.

58. B. Chance, C. Saronio and J. S. Jr. Leigh, *J. Biol. Chem.* **1975**, *250*, 9226.

59. M. Lauraeus, L. Power, B. Chance and M. Wikstrom, *J. Biophys. Biochem.* **1993**, *51*, 274.

60. K. D. Karlin, *Science* **1993**, *261*, 701.

61. K. D. Karlin, *et al*, *J. Am. Chem. Soc.* **1994**, *116*, 4753.

62. S. C. Lee and R. H. Holm, *J. Am. Chem. Soc.* **1993**, *115*, 5833.

63. R. B. VanAtta, C. E. Strouse, L. K. Hanson and J. S. Valentine, *J. Am. Chem. Soc.* **1987**, *109*, 1425.

64. L. K. Hanson, in *Chlorophylls* p. 993, ed. H. Scheer, CRC Press, **1991**.

65. J. A. Pople and D. L. Beveridge, *Approximate Molecular Orbital Theory*, McGraw-Hill, New York , **1970.**

66. J. E. Ridley and M. C. Zerner, *Theoret. Chim. Acta* **1973**, *32*, 111.

67. A. D. Bacon and M.C. Zerner, *Theoret. Chim. Acta* **1979**, *53*, 21.

68. M. C. Zerner, G. Loew and R. F. Kirchner, *J. Am. Chem. Soc.* **1980**, *102*, 589.

69. J. D. Head, M. C. Zerner and B. Weiner, *Chem. Phys. Lett.* **1986**, *131*, 359.

70. M. C. Zerner, J. Mckelvey and W. D. Edwards, *Theoret. Chim. Acta* **1987**, *72*, 347.

71. N. Mataga and K. Nishimoto, *Z. Phys. Chem. (Frankfurt and Main)* **1957**, *13*, 140.

72. M. Gouterman, *In The Porphyrins, Vol. 3, p 1, D. Dolphin eds*, Acad. Press, **1978.**

73. *The Biological Application of Raman Spectroscopy, T. Spiro eds*, John Wily & Son, **1989.**

74. L. M. Proniewicz, A. Bruha, K. Nakamoto, E. Kyuno and J. Kincaid, *J. Am. Chem. Soc.* **1989**, *111*, 7050.

CHAPTER 5

QUANTUM CHEMISTRY OF THE MOMENTUM DISTRIBUTIONS FOR A PARTICLE IN A BOX*

Summary

A particle in a one-dimensional box is a widely used classical model system for the introductory of the quantum mechanism [1-8] and quantum chemistry [9-13]. In most cases, however, only the position distributions of the particle is discussed. In this work, we focus on the momentum distributions for systems in energy eigenstates of the particle-in-a-box Hamiltonian. We obtain simple, explicit expressions for the probability distributions of observing an arbitrary momentum p for a system in state Ψn, and demonstrate the nonclassical features of the momentum distribution. For the lowest energy eigenstate, with n=1, the momentum distribution peak at p=0, rather than at the values $\pm h/2a$ predicted from En. With an increase in quantum number from n=1 to n=2, the distribution bifurcates, and the maxima for the *nth* level approach $\pm p_n$ as n increases, thus illustrating the transition from quantal to classical behavior.

* Results published on *Journal of Chemical Education*, **1995**, *72*, 149 (Co-authors withY. Liang and Y. X. Dardenne).

5.1 Introduction

We consider a particle of mass in a one-dimensional box of length a described by time-independent Schrodinger equation [1-9]:

$$d^2 \Psi(x) /dx^2 + 8p^2mE/h^2 \Psi(x) = 0 \qquad (0<x<a) \qquad (1)$$

Here F(x) is the wave function, h is Planck's constant, and E is the energy. The wave function satisfies the boundary conditions $\Psi(0) = \Psi(a)= 0$.

The normalized energy eigenfunctions are given by [1-9]

$$\psi_n(x) = \sqrt{\frac{2}{a}} \sin(\frac{n\pi x}{a}) \qquad (2)$$

where n=1, 2, 3, ..., and the quantized energy levels obtained naturally from above boundary conditions

$$\Psi(0) = \Psi(a)= 0$$

are

$$E = \frac{h^2 n^2}{8ma^2} \qquad \text{for n=1,2,3,...} \qquad (3)$$

From a classical standpoint, the particle is expected to move back and forth in the box at constant speed, with momentum values $p_n = \pm\sqrt{2mE_n}$. In contrast, quantum mechanically, the energy eigenstates $\Psi(x)$ is not an eigenstate of the momentum operator because

$$p\sqrt{\frac{2}{a}}\sin\left(\frac{npx}{a}\right) = -i\left(\frac{h}{2\pi}\right)\frac{d}{dx}\left(\sqrt{\frac{2}{a}}\sin\left(\frac{n\pi x}{a}\right)\right)$$
$$= -i\left(\frac{h}{2\pi}\right)\left(\frac{n\pi}{a}\right)\sqrt{\frac{2}{a}}\cos\left(\frac{n\pi x}{a}\right) \neq p_0\sqrt{\frac{2}{a}}\sin\left(\frac{n\pi x}{a}\right) \quad (4)$$

This means that the outcome of a momentum measurement for the particle cannot be predicted with certainty.

Because

$$\psi_n(x)\sqrt{\frac{2}{a}}\sin\left(\frac{n\pi x}{a}\right) = -\frac{i}{\sqrt{2a}}[\exp(in\pi x/a) - \exp(-in\pi x/a)] \quad (5)$$

and the time-dependent wave-function $\psi_n(x,t)$ satisfies

$$\psi_n(x,t) = \exp(-iE_n t/h)\,\psi_n(x) \quad (6)$$

it follows that the wave function inside the box is a superposition of traveling wave moving in opposite directions [4]. Each of the two components of $\psi_n(x)$ on the right-hand side of eq (5) is an eigenfunction of the momentum operator. The eigenvalues are $\pm p_n = \pm hn/2a$.

5.2 Obtaining a Momentum Wave Function

Does the quantum uncertainty correspond simply to a classical uncertainty about the direction of motion of the particle? We can answer this question by determining the probability distribution for the particle in state $\psi_n(p)$ in the momentum space. Just as the probability density to find the particle located within the infinitesimal range dx about x is

$$\rho_n(x) = |\psi_n(x)|^2 \tag{7}$$

the probability density to find the momentum within the infinitesimal range dp about p is

$$\rho_n(p) = |\Phi_n(p)|^2 \tag{8}$$

where $\Phi_n(p)$ is the momentum wave function for the state $\psi_n(p)$. The momentum wave function $\Phi_n(p)$ is found by Fourier transformation of $\psi_n(x)$ [1,2, 10]

$$\Phi_n(p) = \frac{1}{\sqrt{h}} \int_0^a (\sqrt{\frac{2}{a}}) \sin(\frac{n\pi x}{a}) \exp(-2\pi i p x / h) dx \tag{9}$$

Therefore, for the particle in a box, in the state $\psi_n(x)$,

$$\Phi_n(p) = \frac{1}{h} \int_0^a (\sqrt{\frac{2}{a}}) \sin(\frac{n\pi x}{a}) \exp(-2i\pi p x / h) dx$$

$$= \frac{-i}{\sqrt{2ahh}} \int_0^a (\exp(in\pi x / a) - \exp(-in\pi x / a)) \exp(-2i\pi p x / h) dx$$

$$= (\sqrt{\frac{h}{2\pi^2 a}})(\frac{p_n}{p_n^2 - p^2})(1 - (-1)^n \exp(-2i\pi p x / h) \qquad \text{(n even)}$$

$$= \frac{2i(\sqrt{\frac{h}{2\pi^2 a}})(p_n) \sin(\frac{pa\pi}{h}) \exp(-i\pi p x / h)}{p_n^2 - p^2}$$

$$= \frac{2(\sqrt{\frac{h}{2\pi^2 a}})(p_n) \cos(\frac{pa\pi}{h}) \exp(-i\pi p x / h)}{p_n^2 - p^2} \qquad \text{(n odd)} \tag{10}$$

where

$$p_n = \frac{nh}{2a} \qquad n=1,2,3,\ldots \qquad (11)$$

Equation 10 gives an explicit, simple expression for the momentum wave function, from which it is easily seen that the wave functions are amplitude-modulated and n-dependent.

5.3 Determining the Probability Distribution

The most important observation from eq 9 is that $\Phi_n(p)$ is nonzero for p values other than $\pm p_n$! The quantum uncertainty is an uncertainty in the value of the momentum, as well as its sign. This is very different from the classical behavior. It is also different from expectations based on the observation that $\psi_n(x)$ in the eq 5 is a superposition of two momentum eigenfunctions [4,6]. The difference reflects a "quantum confinement" effect. Equation 5 holds only within the box. To satisfy the boundary conditions, $\psi_n(x)=0$, elsewhere. If $\psi_n(x)$ is specified by

$$\psi_n(x) = \begin{cases} \exp(\pm in\pi x/a) & \text{for } 0 \le x \le a \\ 0 & \text{for } x<0 \quad or \quad x>a \end{cases} \qquad (11)$$

then $\psi_n(x)$ is not an eigenfunction of the momentum operator. Only if $\psi_n(x) = \exp(\pm in\pi x/a)$ holds without spatial restriction is a momentum eigenfunction obtained.

The corresponding probability densities to observe the momentum in the infinitesimal range dp about p are

$$\rho_{2k}(p)=\frac{(\frac{2h}{a\pi^2})(p_{2k}^2)\sin^2(\frac{p\pi a}{h})}{(p_{2k}^2-p^2)^2} \qquad (n \text{ even}, n=2k)$$

or

$$\rho_{2k-1}(p)=\frac{(\frac{2h}{a\pi^2})(p_{2k-1}^2)\cos^2(\frac{p\pi a}{h})}{(p_{2k-1}^2-p^2)^2} \qquad (\text{n odd, n= 2k-1}) \qquad (12)$$

where k=1, 2, 3, ...

the figure shows the momentum probability densities for the particle in the first several energy eigenstates. The figure and eq 12 show clearly that there is a nonzero probability density to obtain many values other than $\pm nh/2a$ from a given momentum measurement.

A discussion of the momentum probability distribution can be found in the text *Quantum Mechanics* by Cohen-Tannoudji, Diu and Laloe [1]; they provide a physical interpretation in terms of "diffraction functions". However, they do not simplify to the explicit forms of our eq 10 and 12, and we have not found these in any other texts.

The momentum distribution of a particle for different n values are plotted on Figure 1. From eq 12, one can find the maxima and minima of the momentum distribution. From $d\rho(p)/dp=0$, the conditions for the maxima are

$$\cot(\frac{pa\pi}{h})=\frac{-2(\frac{ph}{a\pi})}{p_{2k}^2-p^2} \qquad (\text{n even}, p\neq\pm p_{2k})$$

or

$$\tan(\frac{pa\pi}{h})=\frac{2(\frac{ph}{a\pi})}{p_{2k-1}^2-p^2} \qquad (\text{n odd}, p\neq\pm p_{2k-1}) \qquad (13)$$

These equations can be solved numerically. The minima of the momentum distributions occur when $\rho(p) = 0$, that is, when

$$\sin(\frac{pa\pi}{h}) = 0 \qquad \text{(n even, } p \neq \pm p_{2k}\text{)}$$

or

$$\cos(\frac{pa\pi}{h}) = 0 \qquad \text{(n odd, } p \neq \pm p_{2k-1}\text{)} \tag{14}$$

The separation between typical minima in the momentum distribution is obviously n-independent and equal to h/a.

5.4 Remarks

1. The momentum distribution of a particle in a box gives a definite probability for observing values of p other than those corresponding to the eigen energies of the particle. Interestingly, in analogy with the nodes in the position distribution of the particle (points in space where the particle has zero probability density), the momentum distributions also have zeroes at special values of the momentum. In even n states ($n=2k$), the particle cannot have the momentum values of $p=lh/a$, where $l \neq k$, whereas in odd n states ($n=2k-1$), momentum values of $p=(2l-1)h/2a$ (with $l \neq k$) cannot be observed. We can regard the momentum wave function as a standing wave set up in the momentum space, but it is amplitude-modulated.

2. The momentum of the particle in an eigenstate averages to zero due to the symmetry of momentum distribution; $\rho(p)$ is an even function of p. Thus,

$$\langle p \rangle_n = \int_{-\infty}^{\infty} p\rho_n(p)dp = \int_{-\infty}^{\infty} \psi_n(x)(\frac{-ih}{2\pi d}dx)\psi_n(x)dx = 0 \tag{15}$$

Figure 5.1 Momentum distribution of a particle in a box at various values of n.

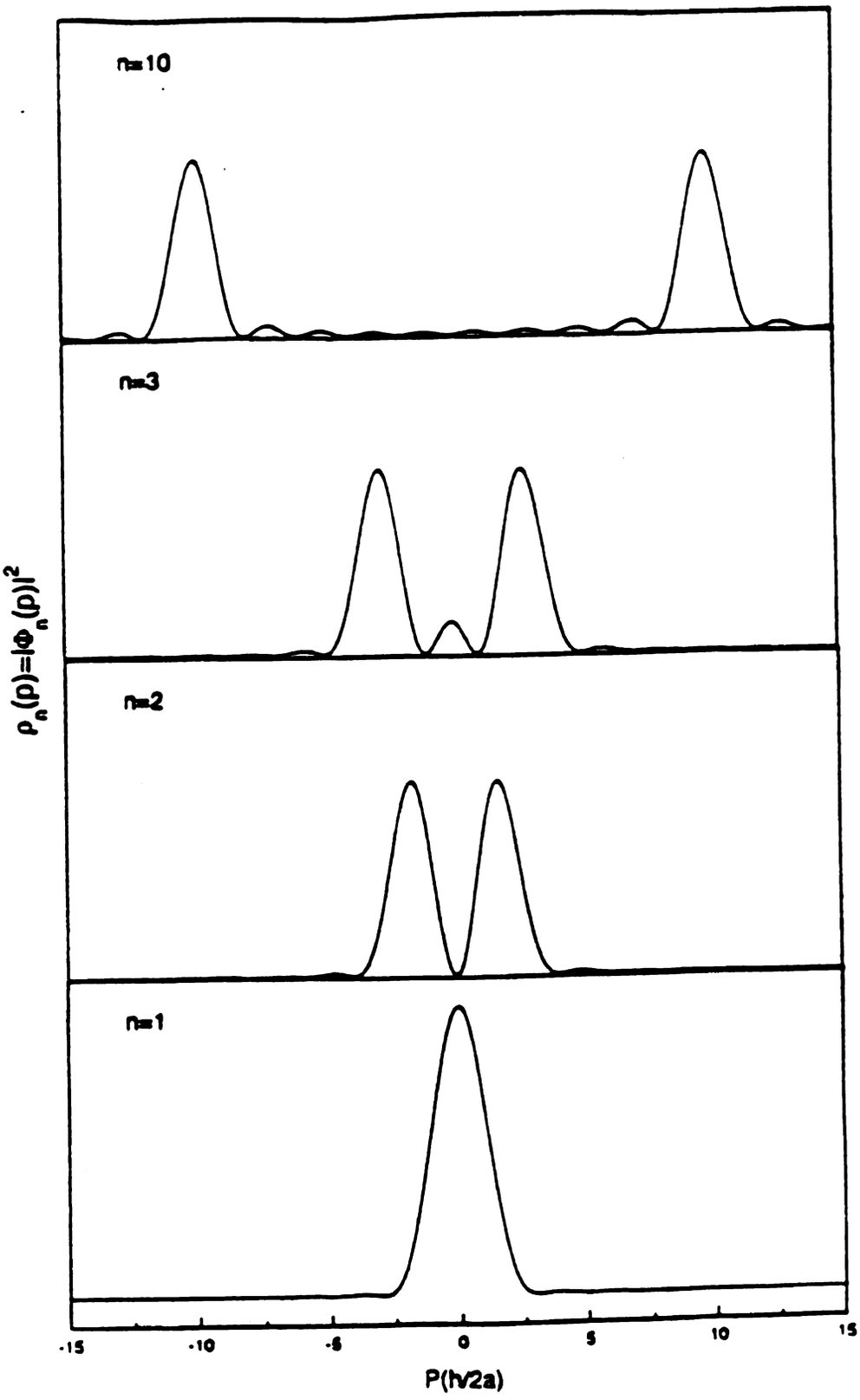
n=10
n=3
n=2
n=1
$\rho_n(p)=|\Phi_n(p)|^2$
-15
-10
-5
0
5
10
15
P(h/2a)

Table 1. The most probable momentum p_m in different states.

n	$P_m(\pm h/2a)$
1	0.000
2	1.675
3	2.790
4	3.845
5	4.950
...	
10	9.985

the probability densities at zero momentum are

$$\rho_{2k}(0) = 0$$

or

$$\rho_{2k-1}(0) = \frac{8a}{(2k-1)^2 h\pi^2} \tag{16}$$

In even n states, one cannot observe the particle with zero momentum (the probability is zero), whereas in odd n states, one does observe zero momentum of the particle with a certain probability. Surprisingly, in the state $\psi_1(x)$, with n=1, the most probable momentum is zero, rather than $\pm p_1 = h/2a$. When n becomes larger (for odd n), the probability of finding the particle with zero momentum decreases.

3. The uncertainty product $\delta p \delta x$ is bounded below, according to the Heisenberg uncertainty principle. Its value is n-dependent for particle-in-a-box energy eigenstates, as shown next. the average value of the position for the particle is

$$\langle x \rangle_n = \int_{-\infty}^{\infty} \psi_n(x) x \psi_n(x) dx = (\frac{2}{a}) \int_0^a x \sin^2(\frac{n\pi x}{a}) dx = a/2 \tag{17}$$

as expected. The average value of x^2 is

$$\langle x^2 \rangle_n = \int_{-\infty}^{\infty} \psi_n(x) x^2 \psi_n(x) dx = (\frac{2}{a}) \int_0^a x \sin^2(\frac{n\pi x}{a}) dx = (\frac{a}{2} n\pi)^2 (\frac{4n^2\pi^2}{3} - 2) \tag{18}$$

thus the root-mean-square deviation of the position for the particle is

$$\delta x = \sqrt{\langle x^2 \rangle_n - \langle x \rangle_n^2} = (\frac{a}{2n\pi})\sqrt{(\frac{n^2\pi^2}{3} - 2)} \tag{19}$$

The mean value of p^2 is given by

$$< p_n^2 >= \int_{-\infty}^{\infty} p^2 \rho_n(p) dp = \int_{-\infty}^{\infty} \psi_n(x)(\frac{-ih}{2\pi}\frac{d}{dx})^2 \psi_n(x) dx = (\frac{nh}{2a})^2 \tag{20}$$

and the root-mean-square deviation of the momentum is

$$\delta p = \sqrt{\langle p^2 \rangle_n - \langle p \rangle_n^2} = \frac{nh}{2a} \tag{21}$$

Combining eqs 18 and 20, one obtains

$$\delta p \delta x = (\frac{nh}{2a})(\frac{a}{2n\pi})\sqrt{(\frac{n^2\pi^2}{3} - 2)} \geq \frac{h}{4\pi} \tag{22}$$

This exceeds the requirements of the uncertainty principle. The uncertainty product grows as n increases! At first glance, this might appear to conflict with expectations that the behavior grows increasingly classical as n increases. However, an interesting result emerges from a calculation of the uncertainty product $\delta p \delta x$ for a purely classical particle subject to the following assumptions.

(1). The particle has equal probability to be observed anywhere in the box;

(2). The momentum of the particle is either $nh/2a$ or $-nh/2a$, with equal probability;

(3). The energy is constant at the value $n^2h^2/(8ma^2)$.

For the classical particle, the position and momentum average satisfy

$$\langle x \rangle_n = a/2,\ \langle x^2 \rangle_n = a^2/3,\ \ \langle p \rangle_n = 0,\ \text{and}\ \langle p^2 \rangle_n = n^2h^2/(4a^2).$$

This yields $\delta p \delta x = nh / 4\sqrt{3}$, which is precisely the large n limiting behavior of eq 21. The classical uncertainty product is independent of the size of the box.

4. The Probability density at $p = \pm p_n$ is a constant (n-independent).

$$\lim_{p \to p_n} \rho(p) = \frac{a}{2h} \tag{23}$$

5.5 Most Probable Momentum

the most probable momentum is not $\pm p_n$ when the particle is in state $\psi_n(x)$. Instead, by numerically solving eq 13 at different n values we find the following values for the most probable momentum p_m in different states.

The figure shows that the momentum distribution for the particle bifurcates from a single peak (in the n=1 state) to two separate peaks near $p = \pm p_n$(for all states n≥2). Only when n becomes large enough the probability density $\rho(p)$ reach its maximum at $p_m \cong \pm p_n$. then the quantum and classical descriptions are unified, in accord with the Bohr correspondence principle.

5.6 Acknowledgments

This work grew out of a problem in CEM 991, selected Topics in Quantum Chemistry, taught by Prof. K. L. C. Hunt. I would like to thank my good friends, Y. Q. Liang and Y. X. Dardenne for joining work on this project. We all thank Prof. K. L. C. Hunt for interesting discussions and reading the manuscripts. I would also like to thank a research assistantship supported through NIH Grant 25480 to Prof. G. T. Babcock during this period.

References

1. C. Cohen-Tannoudji, B. Diu and F. Laloe *Quantum Mechanics*, John Wiley and Sons, **1977.**

2. E. Merzbacher, *Quantum Mechanics*, John Wiley and Sons, **1970.**

3. L. I. Schiff, *Quantum Mechanics*, 3rd ed., McGraw-Hill, **1968.**

4. D. A. McQuarrie, *Quantum Chemistry*, University Science Books, **1983.**

5. P. W. Atkins, *Molecular Quantum Mechanics*, Oxford University, **1970.**

6. M. W. Hanna, *Quantum Chemistry, 3rd ed.*, University Science Books, **1981.**

7. J. P. Lowe, Quantum Chemistry, Student Edition, Academic Press, **1978.**

8. I. N. Levine, *Quantum Chemistry, 3rd ed.*, Allen and Bacon, **1983.**

9. For example, see a). K. Volkamer and M. W. Lerom *J. Chem. Edu.* **1992,** *69,* 100. b). B. D. El-Issa, *J. Chem. Edu.* **1986,** *63,* 761; c). G. R. Miller, *J. Chem. Edu.* **1979,** *56,* 709.

10. G. Arfken, *Mathematical Methods for Physicists, 3rd ed.*, Academic Press, **1985.**